5-2018

ANALYSIS OF TRANSITIONAL SHOCKWAVE BOUNDARY LAYER INTERACTIONS USING ADVANCED RANS-BASED MODELING

Bradley Wayne Tester
University of Tennessee, btester@vols.utk.edu

To the Graduate Council:

I am submitting herewith a thesis written by Bradley Wayne Tester entitled "ANALYSIS OF TRANSITIONAL SHOCKWAVE BOUNDARY LAYER INTERACTIONS USING ADVANCED RANS-BASED MODELING." I have examined the final electronic copy of this thesis for form and content and recommend that it be accepted in partial fulfillment of the requirements for the degree of Master of Science, with a major in Aerospace Engineering.

James G. Coder, Major Professor

We have read this thesis and recommend its acceptance:

Kivanc Ekici, Ryan S. Glasby, John D. Schmisseur

Accepted for the Council:
Dixie L. Thompson

Vice Provost and Dean of the Graduate School

(Original signatures are on file with official student records.)

ANALYSIS OF TRANSITIONAL SHOCKWAVE BOUNDARY LAYER INTERACTIONS USING ADVANCED RANS-BASED MODELING

A Thesis Presented for the

Master of Science

Degree

The University of Tennessee, Knoxville

Bradley Wayne Tester

May 2018

ACKNOWLEDGEMENTS

First and foremost, I would like to thank my spouse, Emily, for her support throughout this adventure. Her continual support pushed me to complete this program.

I would like to express my gratitude towards Dr. James Coder, my advisor, for his guidance in my professional development.

I would also like to thank Dr. John Schmisseur, Dr. Kivanc Ekici, and Dr. Ryan Glasby, for serving on my thesis committee.

Finally, I would like to thank all my friends and family who supported me every step of the way, helping to make my master's degree possible.

This material is based upon research supported by the U. S. Office of Naval Research under award number N00014-15-1-2269.

ABSTRACT

In this work, a series of Reynolds averaged Navier-Stokes (RANS)-based computational fluid dynamics (CFD) simulations are presented to investigate the upstream region of a laminar-turbulent transitional shockwave boundary layer interaction. RANS and delayed detached eddy simulation (DDES) methods are employed using the Spalart-Allmaras (SA) turbulence model in conjunction with a quadratic constitutive relation (QCR), with and without the amplification factor transport transition model. Neither fully turbulent (SA-QCR) nor transitional (SA-QCR-AFT) RANS simulations met machine-zero-level because the simulations displayed unsteadiness inherit to the solution. Initial DDES simulations displayed the oscillatory behavior present in experimental data but, upon further inspection, found disturbances propagating from an upstream overset boundary. DDES simulations using a modified grid system did not exhibit any oscillatory behavior but provided further detail within the separation region. All the CFD simulations showed good agreement with experimental data, but SA-QCR cases did not predict an upstream-influence shock. The RANS simulations under-predicted the UI shock location while the DDES simulations over-predicted the separation shock and triple-point height locations in comparison to experimental data. A single large vortex in the upstream region is captured by the RANS simulations while two vortices are present in the DDES simulations. Analysis of the flowfield consists of velocity profiles, surface pressure measurements, and surface skin frictions to locate regions of separation.

TABLE OF CONTENTS

LIST OF TABLES

LIST OF FIGURES

NOMENCLATURE

Uppercase

$\vec{E}, \vec{F}, \vec{G}$	-	vectors of inviscid and viscous fluxes
M	-	Mach number
N_{crit}	-	critical amplification factor
O_{ik}	-	normalized rotation tensor
P	-	pressure
Re	-	Reynolds number
S_{ij}	-	mean strain-rate tensor
T	-	temperature
U_i	-	mean velocity
$\forall$	-	transformation matrix
X_1	-	distance from refinement mesh leading edge to plate leading edge
X_2	-	distance from refinement mesh trailing edge to plate leading edge

Lowercase

d	-	distance to closest surface
d_c	-	cylinder diameter
e	-	energy per unit mass
h	-	cylinder height
h_{tp}	-	triple point height
$\tilde{n}$	-	amplification factor
q_i	-	heat flux
$\vec{q}$	-	vector of conserved flow variables
t	-	time
u, v, w	-	Cartesian velocity components

$\overline{u_i u_j}$	-	Reynolds stress tensor
y^+	-	non-dimensional wall distance

Greek

α	-	angle of attack
Δ	-	maximum spacing of a grid cell
$\lambda_{s,1}$	-	separation shock standoff distance
$\lambda_{s,2}$	-	reattachment shock standoff distance
μ	-	molecular viscosity
μ_t	-	turbulent eddy viscosity
ν	-	kinematic viscosity
ξ, η, ζ	-	generalized coordinates
ρ	-	density
τ_{ij}	-	turbulent stresses
ω	-	vorticity
Ω	-	vorticity magnitude

Subscripts

∞	-	freestream condition
0	-	stagnation condition
i	-	inviscid
v	-	viscous

CHAPTER 1

INTRODUCTION

Shockwave boundary layer interactions (SBLI) are of growing interest in the high-speed flow research community. As advances in technology continue, the development of aerospace vehicles emphasizes the precision and accuracy of flow parameter predictions. In development of high-speed aerospace vehicles, SBLIs are a significant source of uncertainty. SBLIs pose a threat of early flow separation, acoustic loading and thermal loading, causing a potential for structural fatigue, engine unstart, and thermal heating.

Due to the presenting challenges, a wealth of research since the 1950's has been conducted on SBLIs [1-7]. Each study can be identified by the state of the incoming boundary layer and the shock generator geometry. The state of the incoming boundary layer can be laminar, turbulent, or transitional, while the shock generator geometry can be two-dimensional, axisymmetric, or three-dimensional. Shockwave laminar boundary layer interactions (SLBLI) are accurately predicted computationally and experimentally [6]. Shockwave turbulent boundary layer interactions (STBLI) are inherently unsteady, posing technical challenges. A majority of the experimental and computational efforts for SBLIs has been for STBLIs, producing a wealth of knowledge and understanding behind the phenomena observed. Transitional shockwave boundary layer interactions (XSBLI) have seen a comparative lack of experimental studies. XSBLIs add additional complexities and uncertainties to the analysis and prediction of flow about an aerospace vehicle due to a transitional boundary layer. Although many efforts have been made, accurately predicting the instabilities in a high-speed transitioning boundary layer is still incomplete [8-11]. XSBLIs having a potential to occur on all high-speed vehicles and have been shown to be the source of maximum heat flux [12] furthering the need to accurately predict and account for the effects they attribute.

In recent years, the improvement of computational fluid dynamics (CFD) capabilities has shown better agreement with experimental efforts in all flow regimes. Traditionally in CFD

simulations, scale-resolving methods such as large-eddy simulation (LES) and direct numerical simulation (DNS) were required to accurately predict SBLIs. As a result, simulations that solve for Reynolds-averaged Navier-Stokes (RANS) equations are traditionally regarded as being inadequate for the prediction of SBLIs. However, there have been recent advances in RANS-based modeling with a focus on transition modeling. Transition modeling has significantly increased the predictive capabilities of RANS-based modeling in subsonic flows and has recently been altered to accommodate high-speed flows [13-16]. Simulations that solve the RANS equations are appealing due to their relatively low computational expenses in comparison to higher fidelity methods such as LES and DNS. Several computational studies have been performed on SLBLIs and STBLIs, but like experimental efforts, few computational studies have been conducted for XSBLIs.

1.1 Goals and Research Approach

The primary goal of the current study is to provide further understanding for a standing cylinder on a flat plate XSBLI. The study works to determine the limits and explore the capabilities of RANS-based modeling in predicting XSBLI phenomena, which complements the experimental efforts of Combs et al. [17] and Lash et al. [18-20] to study XSBLI phenomena generated by a standing cylinder on a flat plate. The experimental reference case [18-20] is simulated with the usage of a NASA developed and distributed CFD solver called OVERFLOW [21] using RANS and Delayed Detached Eddy Simulation (DDES) methods. All cases are simulated with the Spalart-Allmaras (SA) turbulence model in conjunction with the quadratic constitutive relation (QCR). Each case was also simulated with and without the amplification factor transport (AFT) transition model. Simulations implementing the SA turbulence model are identified as turbulent interactions while the simulations applying SA-AFT model are identified as transitional interactions.

In summary, the objectives of this thesis are as follows:

- Determine to what extent RANS-based modeling can predict XSBLI flow phenomena as compared to experimental data

- Demonstrate the effectiveness of transition modeling for complex high-speed flows
- Analyze possible origins of the inherent unsteady behavior in XSBLIs

CHAPTER 2

LITERATURE REVIEW

Aforementioned in Chapter 1, various studies performed for SBLIs can be identified by the geometry of the shock generator and the state of the boundary layer. An overview of recent work is presented for XSBLI characterized by the geometry of a shock generator. The geometry of a shock generator can be categorized as either two-dimensional, axisymmetric, or three-dimensional configurations. Two-dimensional configurations consist of impinging shocks and compression ramps. Axisymmetric configurations are comprised of cylinder flares or double cylinders. Three-dimensional configurations consist of standing cylinders, blunt fins, and swept ramps. Common configurations for SBLI studies [4] are illustrated in Figure 2.1. First, recent efforts in two-dimensional configurations are discussed followed by axisymmetric and three-dimensional geometries.

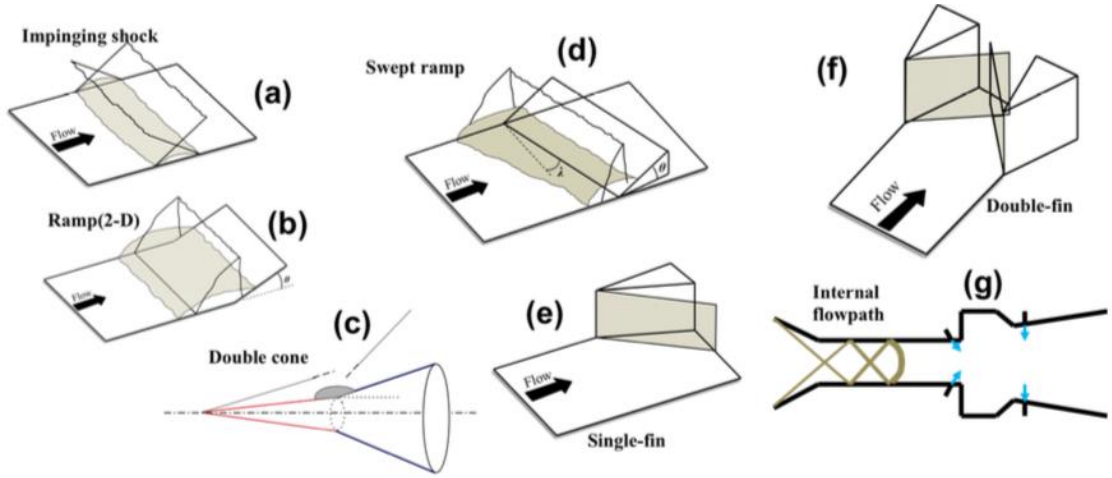

Figure 2.1 Configurations for common SBLI studies (From Ref. [4]).

2.1 Two-Dimensional Configurations

Two-dimensional configurations offer a simplified interaction case for XSBLIs. Typically, these configurations are more straightforward to conduct and analyze. Two-dimensional configurations are considered to be independent from the shock generator geometry, allowing for a freedom of design for test configurations [22]. Although far from the realistic three-dimensional XSBLI, two-dimensional configurations provide a basis for experimental and computational studies.

2.1.1 Impinging Shock

Impinging shocks can be present in supersonic inlets or be the product of a shock generated by any object near a surface [1]. A schematic of the flowfield for an impinging shock incident is illustrated in Figure 2.2. An impinging shock causes the boundary layer to separate, triggering the development of a separation shock from a series of compression waves. Above the separation region, expansion waves turn the flow back towards the surface, which are then followed by a series of compression waves that guide the flow parallel to the surface. The second series of compression waves combine to form a reattachment shock.

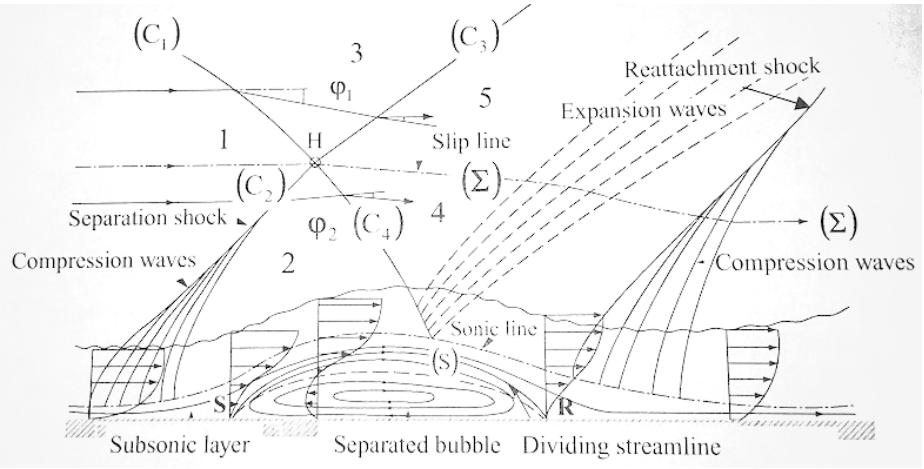

Figure 2.2 Schematic of impinging shock flowfield structure (From Ref. [1]). Flow is from left to right.

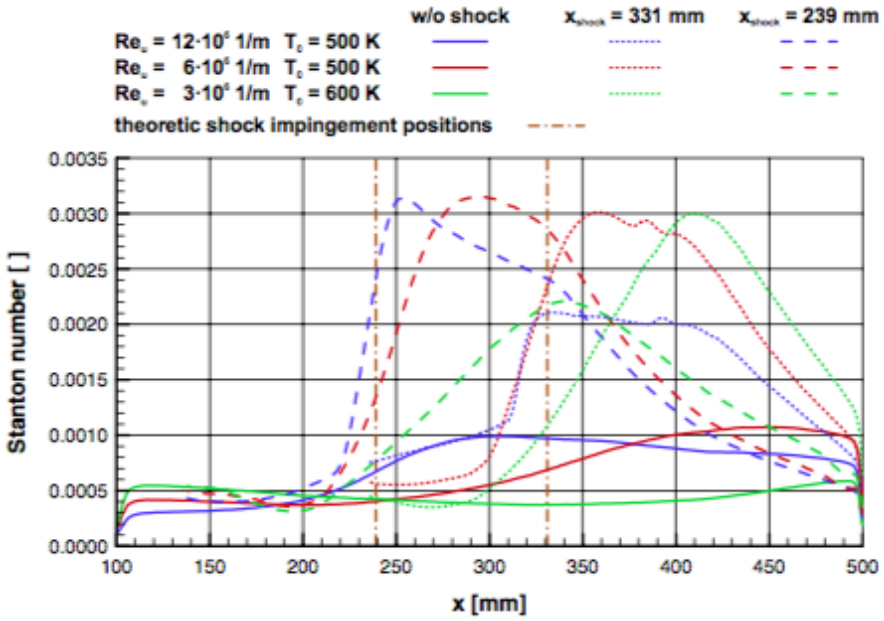

Figure 2.3 Measured Stanton number (From Ref. [25]).

Many experimental efforts involving impinging shock configurations attempt to gain a further understanding of heat flux properties (Stanton number) for re-entry vehicles [22-25]. The Stanton number is used to express the relationship between the wall shear force and the total heat transfer at the wall and is defined as

$$St = \frac{h}{\rho u c_p} \tag{2.1}$$

where h is the convection heat transfer coefficient and c_p is the specific heat of the fluid. Figure 2.3 displays the measured Stanton numbers in Mach 6 flow from Willems et al. [25]. As observed, the XSBLI Stanton number, denoted by the red dotted line, exhibits an initial increase before reaching a maximum value. Additionally, several computational efforts [23, 26] have shown good agreement with experimental heat flux behavior as well as provide further detail on

other flow parameters. Figure 2.4 displays DNS computed skin friction coefficients at various locations. The computed skin friction coefficient drops below a laminar interaction value before exhibiting a strong gradient and peaking above a turbulent interaction. Figure 2.3 plots the LES computed wall pressures. Note that the initial growth in computed surface pressures observed in Figure 2.5 exhibits a similar structure observed in the measured Stanton numbers of Figure 2.3 by the initial rise before the strong gradient. As previously stated, impinging shock configurations are two-dimensional simplifications of real-world three-dimensional boundary layers, but they provide a basis for which high fidelity simulation methods, such as DNS and LES, become possible.

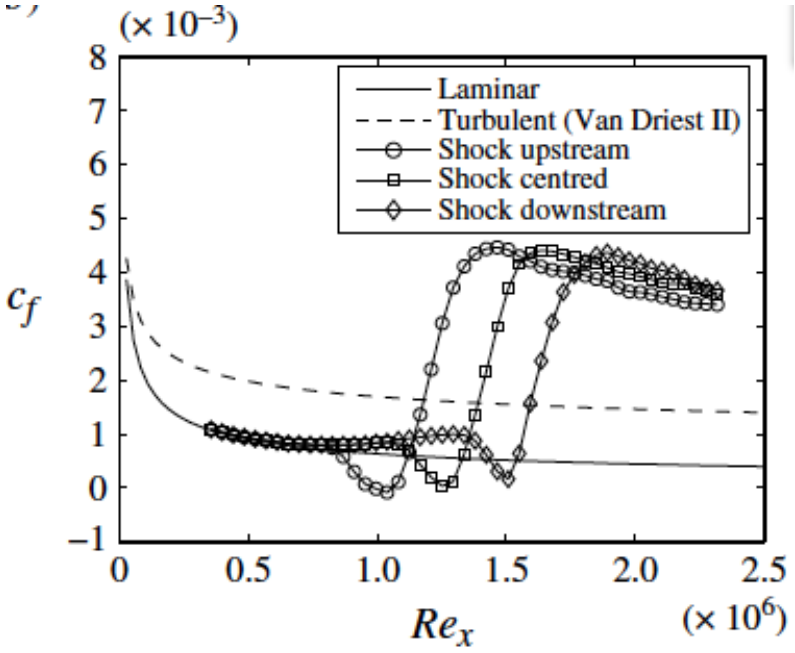

Figure 2.4 DNS computed skin friction coefficient (From Ref. [23]).

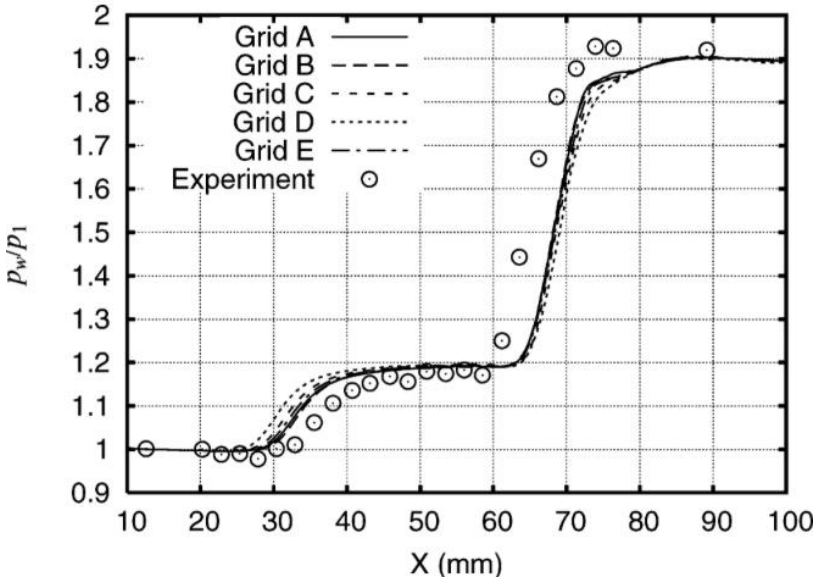

Figure 2.5 LES computed wall pressure (From Ref. [26]).

2.2 Axisymmetric Configurations

Axisymmetric configurations provide a reduced dimensionality mean flow while mitigating contamination from wind tunnel wall effects. These configurations do not guarantee axisymmetric flow but have a greater chance of eliminating other sources of flow contamination such as spanwise effects [27]. Axisymmetric configurations provide more realistic geometries than two-dimensional configurations and are actually present on some aerospace vehicles. However, axisymmetric configurations do not always develop the three-dimensional boundary layers displayed in real-world aerospace vehicles.

2.2.1 Cylinder Flair

Cylinder flairs resemble the typical geometries found on rockets and reentry vehicles. A schematic of the flowfield for a cylinder flair is illustrated in Figure 2.6. The blunt body causes a bow shock to form upstream of the model. The region of interest occurs downstream of the bow shock where a separation shock is formed by an axisymmetric compression ramp (flair). Another

shock forms at the reattachment point due to the change in slope of the geometry [28]. This reattachment point produces the largest peak heat transfer in the flowfield. The state of the incoming boundary layer affects the structure of the separation region [28].

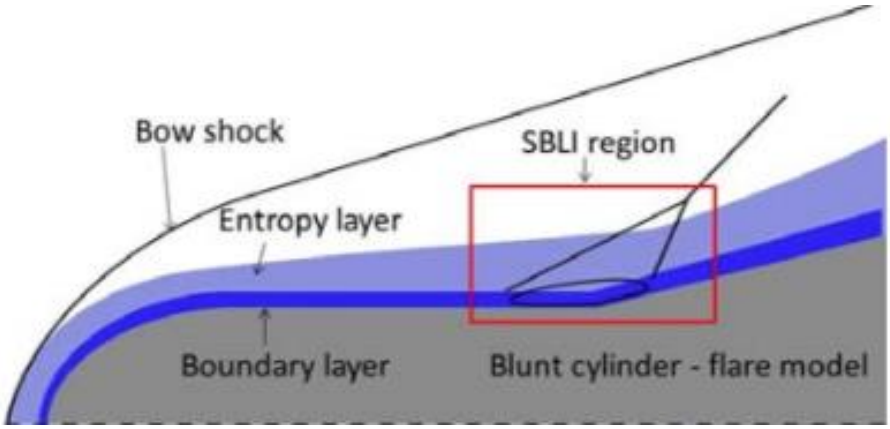

Figure 2.6 Schematic of cylinder flair flowfield (From Ref. [28]). Flow is from left to right.

With heat transfer being of primary concern when designing re-entry vehicles, many cylinder flair configurations focus to understand the heat transfer behavior within a transitional boundary layer. A series of experiments conducted by Vandomme et al. [29], Bur et al. [30], and Benay et al. [27] of the ONERA program found that natural transition of the boundary layer resulted in a higher wall heat flux than a tripped boundary layer, thus recommending forcing transition to obtain a turbulent interaction. Additionally, the natural transition wall pressures, displayed in Figure 2.7, resembled a combination of the measurements seen by Estruch-Samper et al. [31] in separate laminar and turbulent interactions of Figure 2.8. The tripped boundary layer showed better agreement with turbulent interactions.

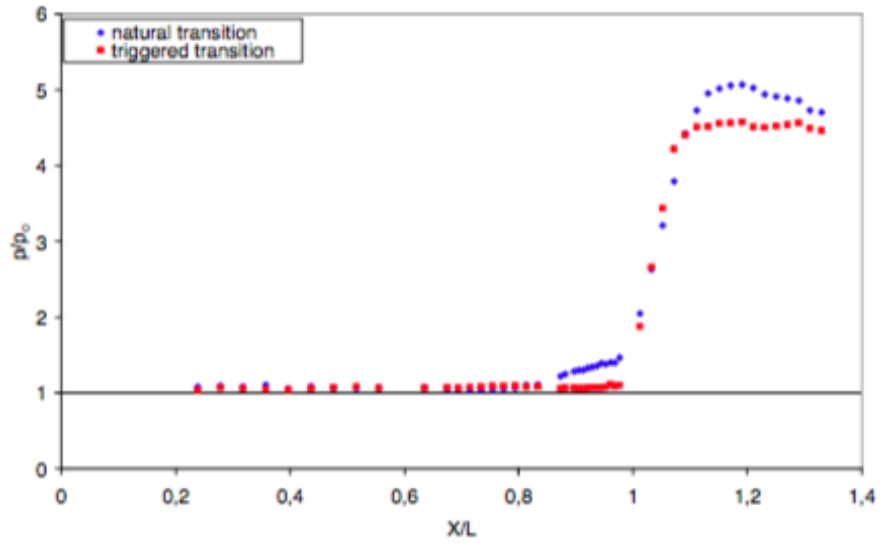

Figure 2.7 Wall pressure measurements (From Ref. [29]).

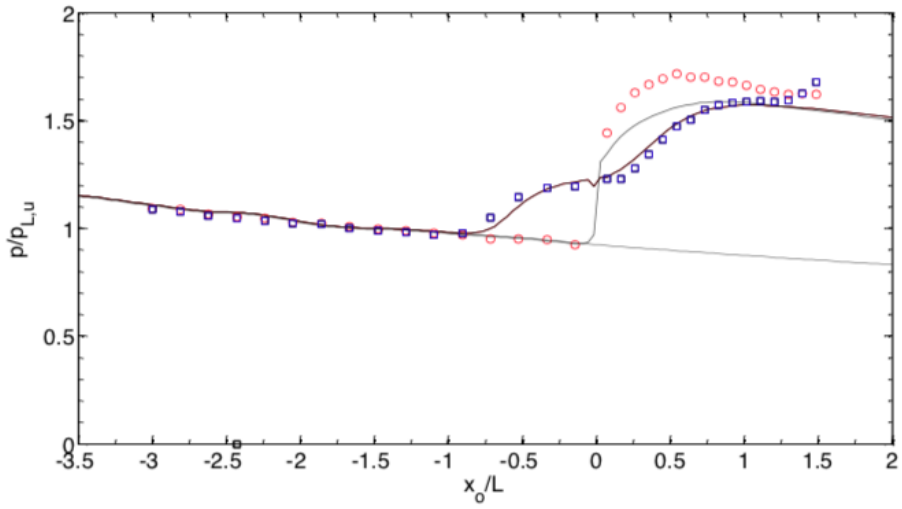

Figure 2.8 Wall pressure measurements for a laminar (blue) and turbulent (red) interaction (From Ref. [31]).

2.3 Three-Dimensional Configurations

2.3.1 Standing Cylinder

Standing cylinders can represent any blunt object on aerospace vehicles protruding from the surface. A schematic of the flowfield for a standing cylinder configuration is illustrated in Figure 2.9. The plate leading-edge forms an inviscid two-dimensional oblique shock. Blunt body flow forms a region of separation, denoted as the separation bubble, upstream of the standing cylinder, forming a separation shock. Flow reattachment further downstream forms a shock, identified as a reattachment (trailing) shock, which combines with the separation shock to form a bow shock upstream of the cylinder. As the boundary layer goes through laminar-turbulent transition, an upstream influence (UI) shock radiates from the separation (forward) shock that have only been observed for a transitional boundary layer [18].

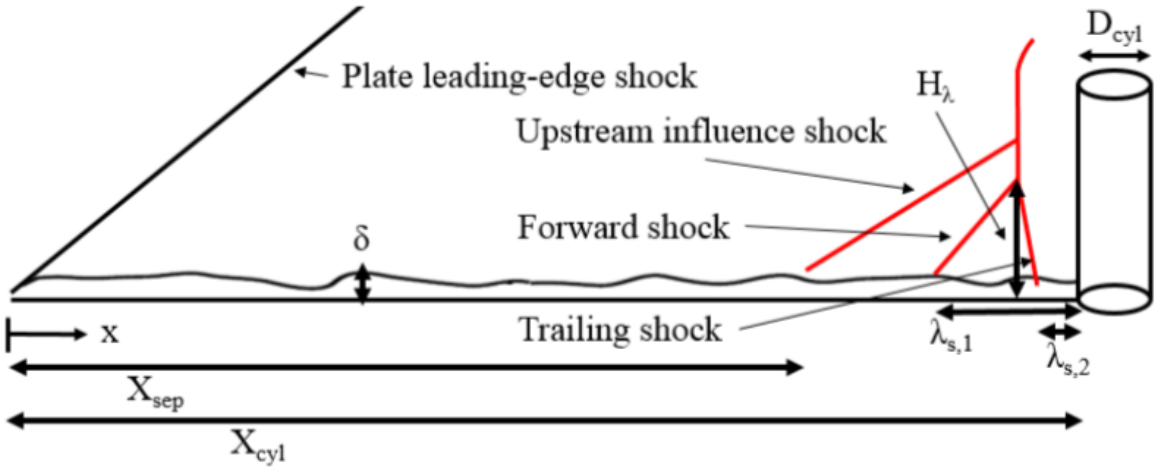

Figure 2.9 Schematic of standing cylinder flowfield (From Ref. [18]). Flow is from left to right.

Due to the three-dimensionality of the cylinder-induced XSBLI, the typical regions of interest have been the centerline plane upstream of the cylinder with additional flow diagnostic techniques incorporated on the upstream spanwise surface. The experimental efforts of Lash et al. [18] and Murphree et al. [32] highlighting the regions of interest are displayed in Figure 2.10

and Figure 2.11. In a transitional boundary layer, the SBLI phenomena resembles a laminar interaction towards the centerline plane and a turbulent interaction in the outward spanwise direction. Additionally, the computational studies of Lindorfer et al. [33] observed that XSBLIs initially resemble laminar interactions before exhibiting turbulent interactions along the centerline streamwise plane.

Several flow diagnostics, such has Schlieren imaging and pressure sensitive paint (PSP), have been employed to analyze XSBLI phenomena. The separation shock of a cylinder-induced XSBLI exhibits unsteady behaviors as demonstrated in Figure 2.12 through Schlieren imaging. As seen through all experimental efforts in XSBLI, a pressure-rise can be an indication of a shock as shown by Dolling and Bogdonoff [34] in Figure 2.13. Since pressure-rise is shown regardless of the test configuration, computational and experimental behaviors of any configuration can be compared.

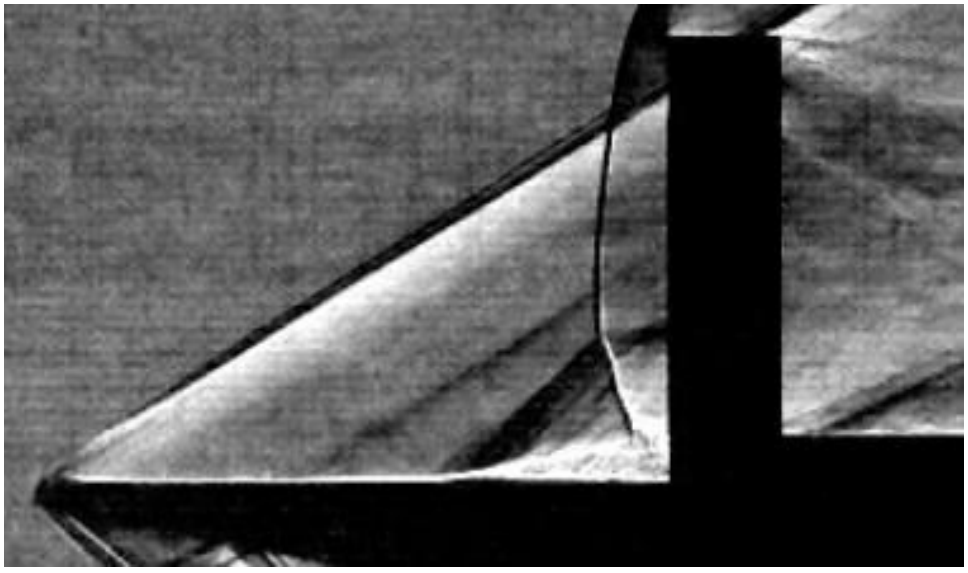

Figure 2.10 XSBLI instantaneous Schlieren image (From Ref. [18]). Flow is from left to right.

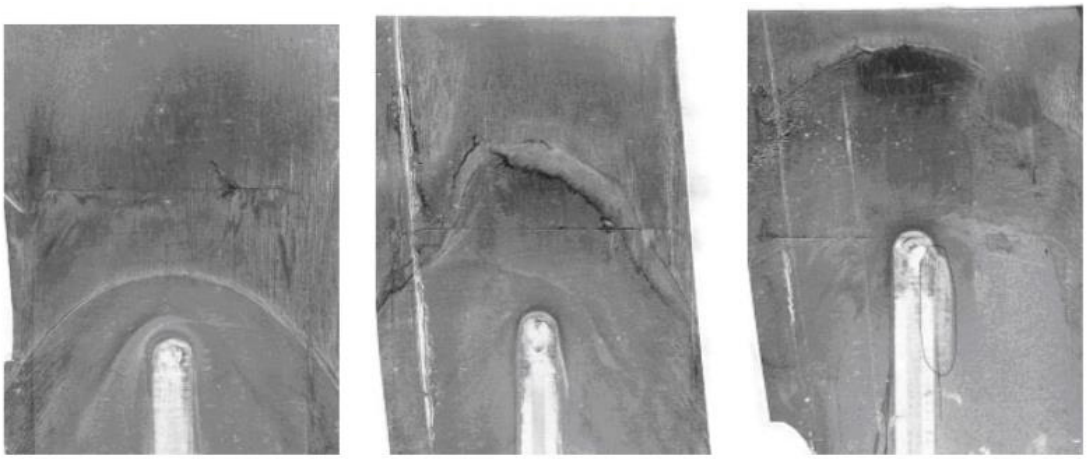

(a) (b) (c)

Figure 2.11 Kerosene-lampblack surface streakline visualization (a) turbulent (b) transitional (c) laminar boundary layer interactions (From Ref. [32]). Flow is from top to bottom.

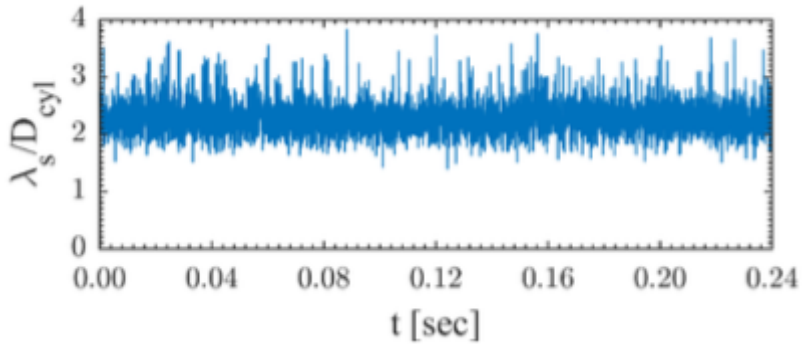

Figure 2.12 Time-accurate measurement of separation shock location upstream of cylinder-induced XSBLI (From Ref. [18]).

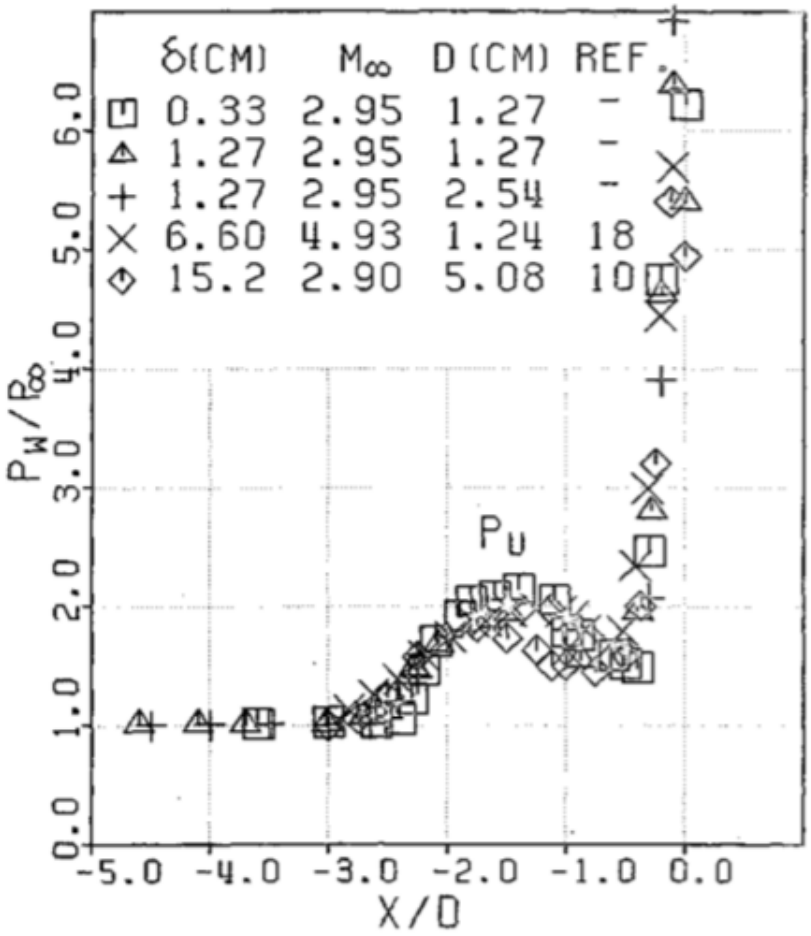

Figure 2.13 Centerline surface pressure measurements (From Ref. [34]).

2.4 Experimental Reference

The experimental reference used for simulating XSBLIs is a standing cylinder mounted on a flat plate tested in the Mach 2, low-enthalpy, blowdown wind tunnel at the University of Tennessee Space Institute described in References [17-20]. The wind tunnel features a test section with a constant cross section of 203 mm x 203 mm (8" x 8"). The following inlet conditions are provided:

- $M_\infty = 2.01$
- $Re = 762{,}000$ per inch
- $T_0 = 513$ R
- $P_0 = 30.5$ psi

2.4.1 Model Geometry

The experiments conducted use a 0.125"-diameter (d_c), 0.500"-tall (h) cylinder model mounted to a flat plate in the wind tunnel. The strut-mounted flat plate measures 203 mm x 182 mm (7.99" x 7.17") and is inclined at a negative angle of attack of -6.3-degree to reduce the potential for leading edge separation. The plate features a sharp leading-edge angle of 10-degrees. A CAD representation of the standing cylinder mounted to the flat plate is illustrated by Figure 2.14.

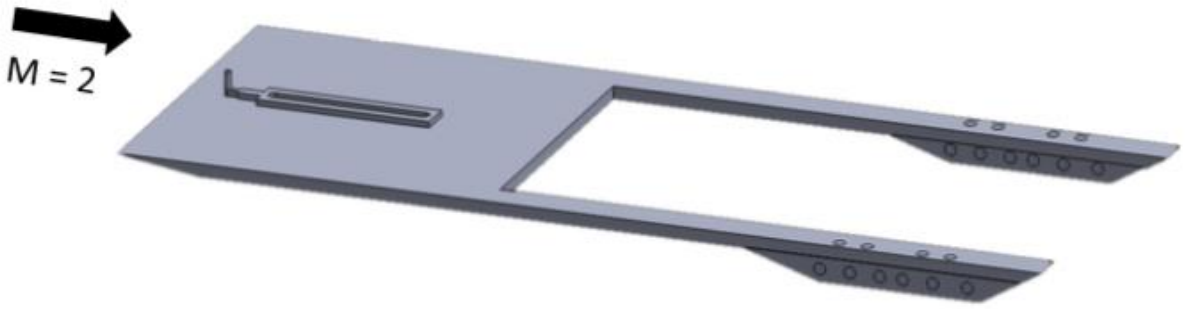

Figure 2.14 CAD representation of the flat plate and cylinder geometry (From Ref. [18]).

2.4.2 Experimental Measurement Techniques

Various flow visualization diagnostics were executed and provided a wealth of information about the shock structure observed in the experiments. XSBLI cases were conducted with the cylinder located 6-8 diameters downstream of the plate leading edge. High-speed Schlieren imaging [18-20], oil flow visualization [18, 19], pressure sensitive paint (PSP) [19], and particle image velocimetry (PIV) [17] techniques provided an analysis of the flowfield.

Schlieren imaging provides a qualitative flow visualization and was integrated to obtain time-resolved shock location measurements. The flow phenomena of XSBLIs typically visible in a Schlieren image analysis are provided in Figure 2.15. Temporal variations of the separation (forward) shock, reattachment (trailing) shock, and upstream influence were analyzed. Surface oil flow visualizations offer additional qualitative results by displaying the mean characteristics of the flow providing a direct comparison to the separation distances observed by Schlieren imaging. PIV identifies the prominent separation regions upstream of the standing cylinder.

The computational simulations of this work were primarily compared to the Schlieren imaging of Lash et al. [18-20]. Thus, the parameters of interest are the location of the separation ($\lambda_{s,1}$) and reattachment shocks ($\lambda_{s,2}$), the triple point height (h_{tp}), and the upstream influence (UI) shock location.

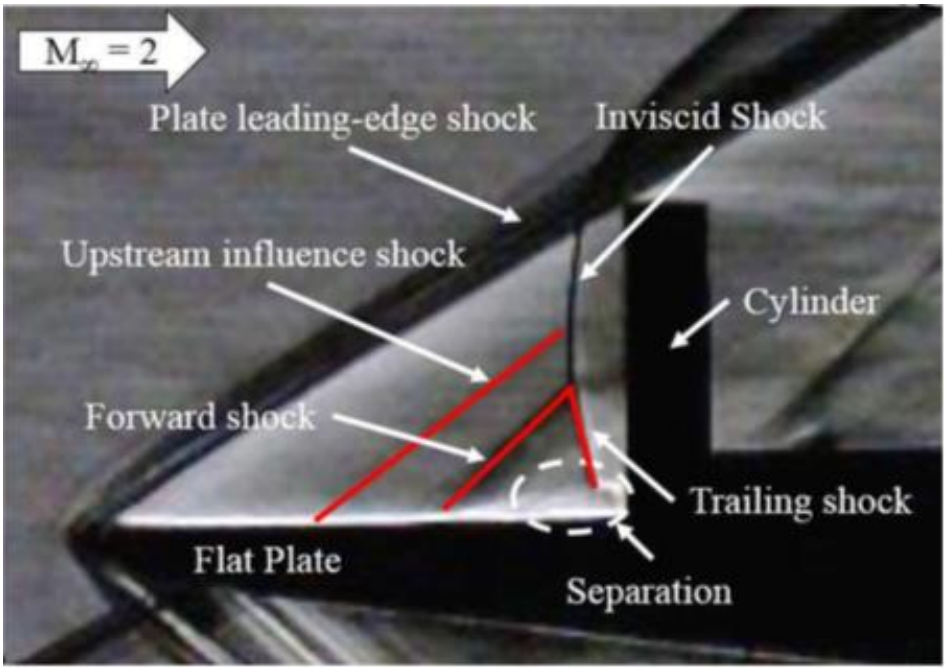

Figure 2.15 Instantaneous Schlieren image of XSBLI phenomena features of interest (From Ref. [18]). Flow is from left to right.

CHAPTER 3

METHODOLOGY

3.1 Governing Equations

OVERFLOW 2.2 [21] solves for the Navier-Stokes equations in generalized coordinates which Pulliam and Steger [35] write as

$$\partial_\tau \vec{q} + \partial_\xi \left(\vec{E}_i - \vec{E}_v \right) + \partial_\eta \left(\vec{F}_i - \vec{F}_v \right) + \partial_\zeta \left(\vec{G}_i - \vec{G}_v \right) = 0 \tag{3.1}$$

The vector of conserved variables can be written as

$$\vec{q} = J^{-1} \begin{bmatrix} \rho \\ \rho u \\ \rho v \\ \rho w \\ e \end{bmatrix} \tag{3.2}$$

where ρ is the density, u, v, and w, are velocities in the x, y, and z directions, and e is the total energy. J^{-1} is a transformation matrix converting the conserved variables from Cartesian to generalized coordinates. Inviscid flux vectors are defined in Cartesian coordinates as follows

$$\vec{E}_i = J^{-1} \begin{bmatrix} \rho U \\ \rho u U + \xi_x p \\ \rho v U + \xi_y p \\ \rho w U + \xi_z p \\ (e+p) U - \xi_t p \end{bmatrix}, \; \vec{F}_i = J^{-1} \begin{bmatrix} \rho V \\ \rho u V + \eta_x p \\ \rho v V + \eta_y p \\ \rho w V + \eta_z p \\ (e+p) V - \eta_t p \end{bmatrix}, \; \vec{G}_i = J^{-1} \begin{bmatrix} \rho W \\ \rho u W + \zeta_x p \\ \rho v W + \zeta_y p \\ \rho w W + \zeta_z p \\ (e+p) W - \zeta_t p \end{bmatrix} \tag{3.3}$$

where *p* is the pressure and *U*, *V*, and *W* are contravariant velocities are

$$\begin{aligned} U &= \xi_t + \xi_x u + \xi_y v + \xi_z w \\ V &= \eta_t + \eta_x u + \eta_y v + \eta_z w \\ V &= \zeta_t + \zeta_x u + \zeta_y v + \zeta_z w \end{aligned} \tag{3.4}$$

The viscous flux vectors are written as

$$\begin{aligned} \vec{E_v} &= J^{-1} \begin{bmatrix} 0 \\ \xi_x \tau_{xx} + \xi_y \tau_{xy} + \xi_z \tau_{xz} \\ \xi_x \tau_{yx} + \xi_y \tau_{yy} + \xi_z \tau_{yz} \\ \xi_x \tau_{zx} + \xi_y \tau_{zy} + \xi_z \tau_{zz} \\ \xi_x \beta_x + \xi_y \beta_y + \xi_z \beta_z \end{bmatrix} \\ \vec{F_v} &= J^{-1} \begin{bmatrix} 0 \\ \eta_x \tau_{xx} + \eta_y \tau_{xy} + \eta_z \tau_{xz} \\ \eta_x \tau_{yx} + \eta_y \tau_{yy} + \eta_z \tau_{yz} \\ \eta_x \tau_{zx} + \eta_y \tau_{zy} + \eta_z \tau_{zz} \\ \eta_x \beta_x + \eta_y \beta_y + \eta_z \beta_z \end{bmatrix} \\ \vec{G_v} &= J^{-1} \begin{bmatrix} 0 \\ \zeta_x \tau_{xx} + \zeta_y \tau_{xy} + \zeta_z \tau_{xz} \\ \zeta_x \tau_{yx} + \zeta_y \tau_{yy} + \zeta_z \tau_{yz} \\ \zeta_x \tau_{zx} + \zeta_y \tau_{zy} + \zeta_z \tau_{zz} \\ \zeta_x \beta_x + \zeta_y \beta_y + \zeta_z \beta_z \end{bmatrix} \end{aligned} \tag{3.5}$$

and

$$\begin{aligned} \tau_{xx} &= \lambda \left(u_x + v_y + w_z \right) + 2\mu u_x \\ \tau_{xy} &= \tau_{yx} = \mu \left(u_y + v_x \right) \\ \tau_{xz} &= \tau_{zx} = \mu \left(u_z + w_x \right) \\ \tau_{yy} &= \lambda \left(u_x + v_y + w_z \right) + 2\mu v_y \\ \tau_{yz} &= \tau_{zy} = \mu \left(v_z + w_y \right) \\ \tau_{zz} &= \lambda \left(u_x + v_y + w_z \right) + 2\mu w_z \\ \beta_x &= \gamma \kappa Pr^{-1} \partial_x e_1 + u\tau_{xx} + v\tau_{xy} + w\tau_{xz} \\ \beta_y &= \gamma \kappa Pr^{-1} \partial_y e_1 + u\tau_{yx} + v\tau_{yy} + w\tau_{yz} \\ \beta_z &= \gamma \kappa Pr^{-1} \partial_z e_1 + u\tau_{zx} + v\tau_{zy} + w\tau_{zz} \\ e_1 &= e\rho^{-1} - 0.5 \left(u^2 + v^2 + w^2 \right) \end{aligned} \tag{3.6}$$

where τ_{ij} are the turbulent shear stresses, λ is the ratio of specific heats, κ is the coefficient of thermal conductivity, and *Pr* is the Prandtl number. The coordinate transformations in arbitrary curvilinear space are given by

$$\begin{array}{ll} \xi_x = J\left(y_\eta z_\zeta - y_\zeta z_\eta\right) & \eta_x = J\left(z_\xi y_\zeta - y_\xi z_\zeta\right) \\ \xi_y = J\left(z_\eta x_\zeta - x_\eta z_\zeta\right) & \eta_y = J\left(x_\xi z_\zeta - x_\zeta z_\xi\right) \\ \xi_z = J\left(x_\eta y_\zeta - y_\eta x_\zeta\right) & \eta_z = J\left(y_\xi x_\zeta - x_\xi y_\zeta\right) \\ \zeta_x = J\left(y_\xi z_\eta - z_\xi y_\eta\right) & \xi_t = -x_t\xi_x - y_t\xi_y - z_t\xi_z \\ \zeta_y = J\left(x_\eta z_\xi - x_\xi z_\eta\right) & \eta_t = -x_t\eta_x - y_t\eta_y - z_t\eta_z \\ \zeta_z = J\left(x_\xi y_\eta - y_\xi x_\eta\right) & \zeta_t = -x_t\zeta_x - y_t\zeta_y - z_t\zeta_z \end{array} \tag{3.7}$$

and

$$J^{-1} = x_\xi y_\eta z_\zeta + x_\zeta y_\xi z_\eta + x_\eta y_\zeta z_\xi - x_\xi y_\zeta z_\eta - x_\eta y_\xi z_\zeta - x_\zeta y_\eta z_\xi \tag{3.8}$$

3.2 Grid Generation

The generation of the grid system was performed using Chimara Grid Tools v2.1 [36]. The flat plate is defined as being 0.25” thick with a 10-degree knife-edge which matches the experimental reference. Coarse and fine grid systems are used for simulations with the latter being a modified version of the initial grid system, correcting for initial observed disturbances. Each piece of geometry has its own grid system connected through overset connectivity illustrated in Figure 3.1: tunnel, flat plate, refinement region, cylinder, and cylinder patch. The cylinder patch eliminates a singularity point on top of the cylinder.

The initial grid system totals 14.9 million grid points amongst the five meshes. The cylinder features 201 axisymmetric points along the circumference with 95 axial points and 45 wall-normal points. The cylinder patch on top of the cylinder is a 65x65x51 overset grid patch matching the spacing constraints of the cylinder. A refinement mesh was placed around the cylinder to capture XSBLI phenomena. The 0.5”-wide refinement mesh features 0.005”x0.005” spacing in the streamwise and spanwise directions. The wall spacing for all viscous walls is

1.8×10^{-5} inches corresponding to a $y^+ \approx 2/3$. In the refinement region, the wall spacing grows geometrically until reaching 0.005", above which the spacing is isotropic. The flat plate and tunnel feature a spanwise spacing of 0.01" at the centerline and geometrically grow to 0.1" at the outward edge. The flat plate and tunnel meshes are each 2" wide, yielding a narrower test section than the experiment (8"). Although narrower than the experiment, the grid was designed so that the reflected shocks are downstream while providing computational savings. The centerline plane and surface mesh of the initial grid system are displayed in Figure 3.2.

The modified grid system totals 28.0 million grid points with the primary modification implemented on the refinement mesh. The refinement mesh was essentially moved further upstream with the trailing-edge positioned closer to the cylinder and leading-edge nearly flush with the flat plate leading-edge to fully capture the shock structure. The trailing-edge positioning was determined from the sonic line downstream of the cylinder obtained by the initial grid system's simulation displayed in Figure 3.3. Additionally, the refinement mesh was expanded to 1.6" in the spanwise direction to capture more of the separation shock. The isotropic region was widened to 1" in the spanwise direction with the spacing geometrically growing out to 1.6" wide. Lastly, the refinement mesh was tended in the wall-normal direction to match the wall-normal height of the flat plate mesh. Additional grid points in the wall-normal direction were placed near the wall to provide a smoother transition from the wall spacing to the specified 0.005" spacing of the refinement mesh. The next modification was implemented on the cylinder patch to match the height of the cylinder mesh in the wall-normal direction. Figure 3.4 displays the centerline plane and surface mesh of the modified grid system. Table 3.1 compares the refinement block's dimensions and spacing of both grid systems. X_1 represents the distance between the plate and refinement leading-edges while X_2 represents the distance from the plate leading-edge to the refinement trailing-edge.

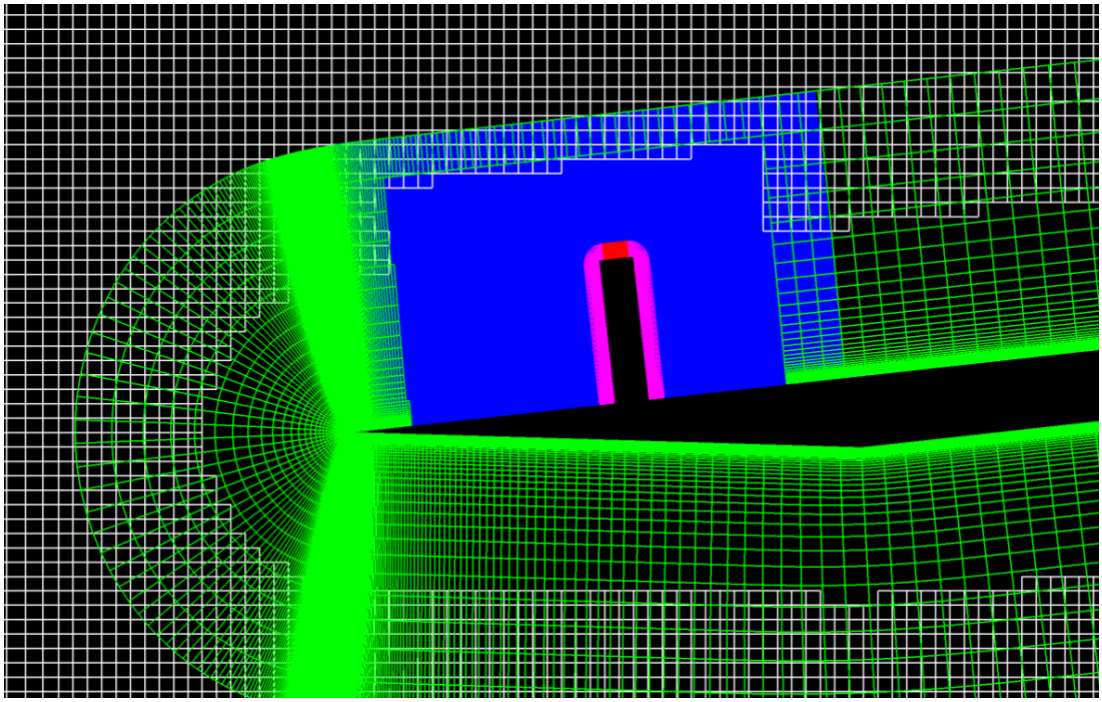

Figure 3.1 Meshes in grid system: tunnel (white), flat plate (green), refinement region (blue), cylinder (pink), and cylinder patch (red).

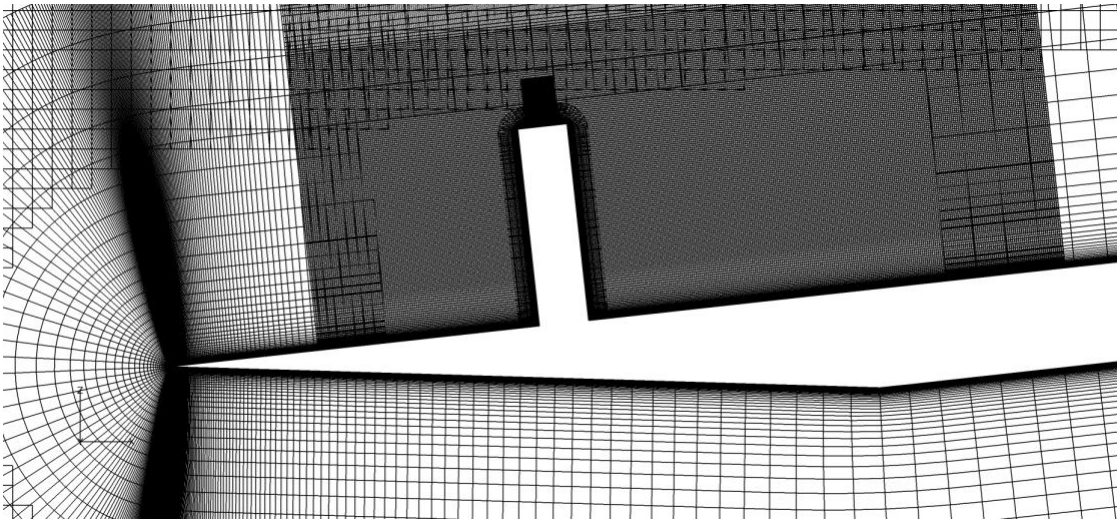

(a)

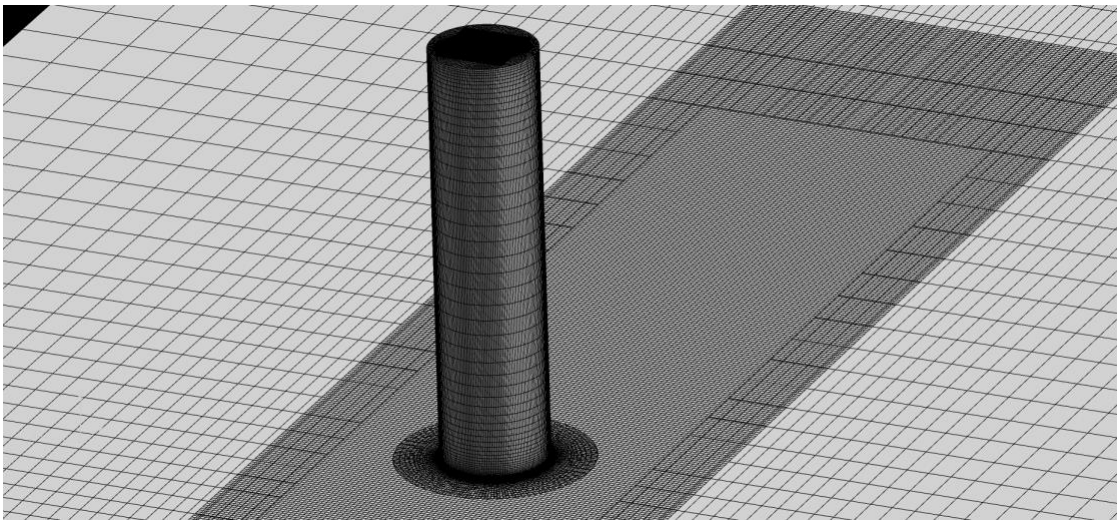

(b)

Figure 3.2 Initial grid system (a) mid-span plane of the grid system after hole cutting, (b) cylinder surface and refinement region.

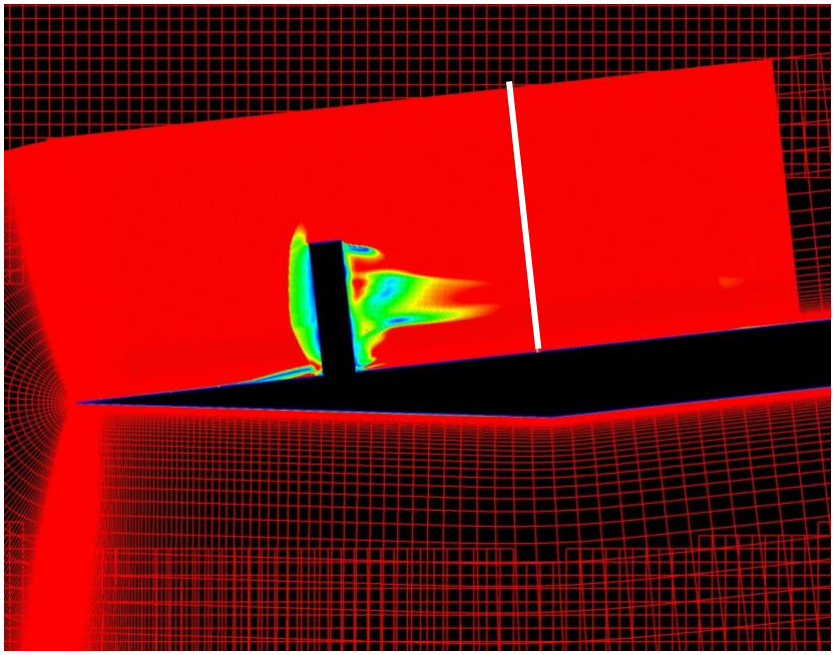

Figure 3.3 Subsonic Mach contours and specified sonic line for grid refinement. Flow is from left to right.

Table 3.1 Comparison of the refinement blocks.

	Initial Grid System	**Modified Grid System**
Dimensions	401 x 101 x 187	343 x 241 x 251
Width (in)	0.5	1.6
X_1 *(in)*	0.50	0.04
X_2 *(in)*	2.50	1.75

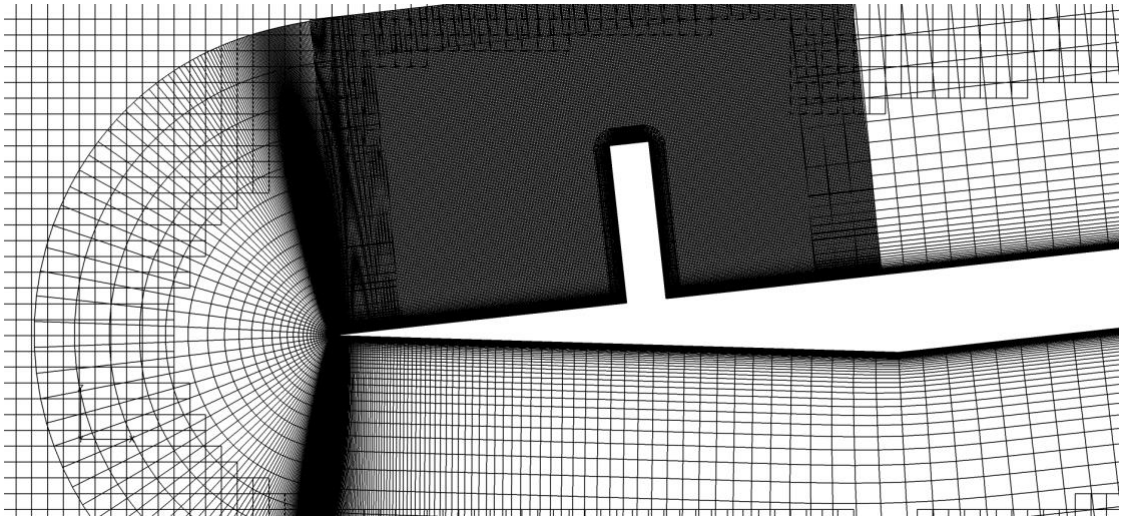

(a)

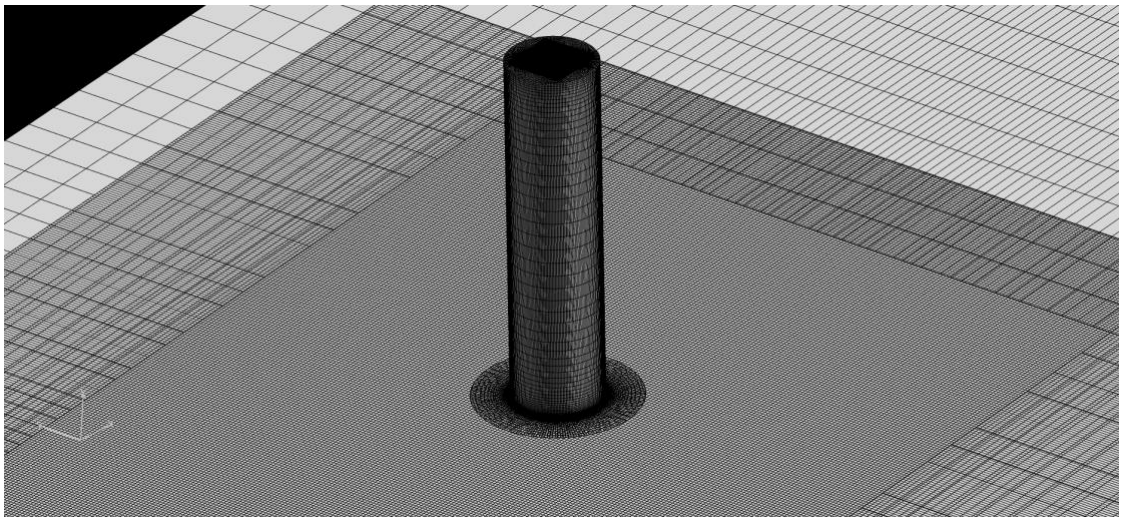

(b)

Figure 3.4 Modified grid system (a) mid-span plane of the grid system after hole cutting, (b) cylinder surface and refinement region.

3.2.1 Overset Connectivity

Overset connectivity was developed using OVERFLOW's internal routine called domain connectivity function (DCF) with XRAY hole cutters [37] that were defined using GENX, a domain connectivity pre-processor within Chimera Grid Tools. XDELTA definitions, which are the offset of the hole from the surface defined through XRAY hole cutters, were chosen to ensure sufficient overlap with zero orphan points. Three holes were created as is evident in Figure 3.6a. Holes were cut from the tunnel, flat plate, and refinement mesh to allow connectivity amongst all five meshes. The primary alteration in the modified grid system expanded the hole containing the refinement mesh to capture more of shock system on a single mesh and minimize the influence of overset boundaries. As seen by differences in Figure 3.4a and Figure 3.5a, the hole was additionally expanded in the wall-normal direction. The hole generated in the each of the initial grid system's mesh (tunnel, flat plate, and refinement mesh) had an XDELTA value of 0.5", 0.02", and 0.001" respectively. The modified grid system held the same XDELTA values with the exception of 0.01" for the flat plate mesh. The angle of attack of the model geometry and position of the cylinder were defined using the transformation features available in OVERFLOW.

3.2.2 Boundary Conditions

The flat plate and cylinder surfaces are specified as viscous (no-slip), adiabatic walls. As previously mentioned, all viscous walls feature a wall spacing of 1.8×10^{-5} inches. All the test-section walls of the tunnel are specified as inviscid (slip) walls. The tunnel inlet conditions are specified with a Mach number of 2.01, Reynolds number of 762,000 per inch, and a static temperature of 283.7 R. For numerical purposes, startup iterations were performed with a subsonic tunnel inlet Mach number of 0.8 before applying the supersonic condition. The outlet conditions of the tunnel are based on Riemann invariants of the inlet flow.

3.3 Numerical Formulation

OVERFLOW features a wide variety of implicit solvers and inviscid flux algorithms and incorporates several popular turbulence/transition models. For the work presented, simulations

used a fifth-order accurate WENO upwind spatial discretization scheme [38] with the HLLE++ fluxes of Tramel, Nichols, and Buning [39]. An entropy-smoothing parameter ($\delta = 5$) was applied, mitigating slip lines created when the shocks are oblique to the grid [39]. No additional artificial dissipation was required to stabilize the solution. An implicit SSOR algorithm [40] was employed for both RANS and DDES simulations. The implicit SSOR algorithm [40] was chosen for its robustness in high-speed flows. The simulations consisted of a subsonic run at a Mach of 0.8 for 1000 steps to initialize the flow, a supersonic run at a Mach of 2.01 for 10000 steps to obtain a steady RANS solution, and a DDES run for 2000 steps to obtain an unsteady solution. A non-dimensional time-step of 0.005 (based on free-stream velocity) was chosen for DDES simulations to provide a convective Courant-Friedrichs-Lewy (CFL) number of approximately 1 within the region of interest resulting in two convective flow-throughs.

Second-order time accuracy was achieved with the backward differentiation formula (BDF2) scheme. For the initial grid system, dual-time stepping was utilized to converge the L_{inf}-norm of the right-hand side (RHS) by three orders of magnitude per time step. With the same convergence criterion as dual-time stepping, Newton sub-iterations were executed for the modified grid system due dual-time stepping's tendency to dampen the turbulent wake structures observed in the DDES simulations. DDES-SA-QCR required approximately 30 Newton sub-iterations to converge while DDES-SA-QCR-AFT called for the specified maximum 50 sub-iterations.

3.3.1 Weighted Essentially Nonoscillatory (WENO) Spatial Discretization

A fifth-order approximation using WENO spatial discretization consists of three third-order approximations as illustrated in Figure 3.5 [38]. The WENO discretization presented follows that of Henrick et al. [41] and Merriman [42] which the fifth-order conservative variables are

$$\hat{q}^L_{i+\frac{1}{2}} = w_0^L \hat{q}^{L0}_{i+\frac{1}{2}} + w_1^L \hat{q}^{L1}_{i+\frac{1}{2}} + w_2^L \hat{q}^{L2}_{i+\frac{1}{2}} \tag{3.9}$$

$$\hat{q}^R_{i+\frac{1}{2}} = w_0^R \hat{q}^{R0}_{i+\frac{1}{2}} + w_1^R \hat{q}^{R1}_{i+\frac{1}{2}} + w_2^R \hat{q}^{R2}_{i+\frac{1}{2}} \tag{3.10}$$

where the third-order approximations are computed from the conservative variables at the nodes as

$$\begin{aligned}\hat{q}^{L0}_{i+\frac{1}{2}} &= \tfrac{1}{3}q_{i-2} - \tfrac{7}{6}q_{i-1} + \tfrac{11}{6}q_i \\ \hat{q}^{L1}_{i+\frac{1}{2}} &= -\tfrac{1}{6}q_{i-1} + \tfrac{5}{6}q_i + \tfrac{1}{3}q_{i+1} \\ \hat{q}^{L2}_{i+\frac{1}{2}} &= \tfrac{1}{3}q_i + \tfrac{5}{6}q_{i+1} - \tfrac{1}{6}q_{i+2}\end{aligned} \tag{3.11}$$

$$\begin{aligned}\hat{q}^{R0}_{i+\frac{1}{2}} &= \tfrac{1}{3}q_{i+3} - \tfrac{7}{6}q_{i+2} + \tfrac{11}{6}q_{i+1} \\ \hat{q}^{R1}_{i+\frac{1}{2}} &= -\tfrac{1}{6}q_{i+2} + \tfrac{5}{6}q_{i+1} + \tfrac{1}{3}q_i \\ \hat{q}^{R2}_{i+\frac{1}{2}} &= \tfrac{1}{3}q_{i+1} + \tfrac{5}{6}q_i - \tfrac{1}{6}q_{i-1}\end{aligned} \tag{3.12}$$

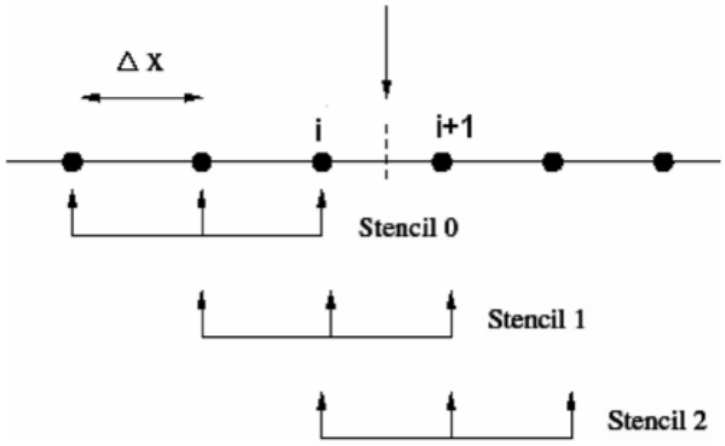

Figure 3.5 Stencil for fifth-order WENO methodology (From Ref. [29])

The weights (*w*) are given by

$$\tilde{w}_k = \frac{\gamma_k}{(\varepsilon + \beta_k)^2} \tag{3.13}$$

where γ_k are the optimal weight values: $\gamma_1 = 0.1$, $\gamma_2 = 0.6$, and $\gamma_3 = 0.3$. Smoothness indicators (β_k) increase the numerical dissipation when large variations in the flow are present and are given by [43]

$$\begin{aligned}\beta_0^L &= \tfrac{13}{12}\left(q_{i-2} - 2q_{i-1} + q_i\right)^2 + \tfrac{1}{4}\left(q_{i-2} - 4q_{i-1} + 3q_i\right)^2 \\ \beta_1^L &= \tfrac{13}{12}\left(q_{i-1} - 2q_i + q_{i+1}\right)^2 + \tfrac{1}{4}\left(q_{i-1} - q_{i+1}\right)^2 \\ \beta_2^L &= \tfrac{13}{12}\left(q_i - 2q_{i+1} + q_{i+2}\right)^2 + \tfrac{1}{4}\left(3q_i - 4q_{i+1} + q_{i+2}\right)^2\end{aligned} \tag{3.14}$$

$$\begin{aligned}\beta_0^R &= \tfrac{13}{12}\left(q_{i+3} - 2q_{i+2} + q_{i+1}\right)^2 + \tfrac{1}{4}\left(q_{i+3} - 4q_{i+2} + 3q_{i+1}\right)^2 \\ \beta_1^R &= \tfrac{13}{12}\left(q_{i+2} - 2q_{i+1} + q_i\right)^2 + \tfrac{1}{4}\left(q_{i+2} - q_i\right)^2 \\ \beta_2^R &= \tfrac{13}{12}\left(q_{i+1} - 2q_i + q_{i-1}\right)^2 + \tfrac{1}{4}\left(3q_{i+1} - 4q_i + q_{i-1}\right)^2\end{aligned} \tag{3.15}$$

3.3.2 Backward Differentiation Formula (BDF)

A backward differentiation formula (BDF) is used to solve the general initial value problem

$$y' = f\left(t, y\right), \qquad y\left(t_0\right) = y_0 \tag{3.16}$$

To attain a second-order BDF (BDF2) approximation of the derivative term, Taylor series approximations of points *i, i-1,* and *i-2* are computed as follows

$$\begin{gathered}A\left[f_i = f_i\right] \\ B\left[f_{i-1} = f_i - f_i' h + f_i'' \tfrac{h^2}{2!} + \cdots\right] \\ C\left[f_{i-2} = f_i - f_i'\left(2h\right) + f_i'' \tfrac{(2h)^2}{2!} + \cdots\right]\end{gathered} \tag{3.17}$$

where *i* is the point of interest and *h* is the step size. The linear system of equations is represented by

$$\begin{bmatrix}1 & 1 & 1 \\ 0 & -1 & -2 \\ 0 & 1/2 & 2\end{bmatrix}\begin{bmatrix}A \\ B \\ C\end{bmatrix} = \begin{bmatrix}0 \\ 1 \\ 0\end{bmatrix} \tag{3.18}$$

where A = 3/2, B = -4/2, and C = 1/2. Thus, the approximation of the general initial value problem using a BDF2 approximation is

$$y_i - \frac{4}{3}y_{i-1} + \frac{1}{3}y_{i-2} = \frac{2}{3}hf\left(t_i, y_i\right) \tag{3.19}$$

3.3.3 Turbulence/Transition Modeling

The turbulence model used in the simulations is the one-equation Spalart-Allmaras (SA) eddy-viscosity model [44] in conjunction with the quadratic constitutive relation (QCR2000) [45] for the initial grid system and the updated version (QCR2013) [46] for the modified grid system as the work transitioned from OVERFLOW 2.2l to OVERFLOW 2.2n. QCR has been shown to improve juncture and corner flow [45]. A curvature/rotation correction term was included to better account for curvature and rotational effects. In addition, the amplification factor transport (AFT) model of Coder [47] was used to capture laminar-turbulent transitional effects. The turbulence model had a time-step equal to the flow solver time-step and a freestream turbulence level of $2.8\text{x}10^{-7}$. A freestream turbulent kinetic energy of $3.91\text{x}10^{-6}$, resulting in N_{crit} = 5 (critical amplification factor), was chosen to influence transition to occur upstream of the standing cylinder. The process of determining N_{crit} = 5 will be elaborated upon in the Chapter 4.

3.3.3.1 Spalart-Allmaras Turbulence Model (SA-RC-QCR)

The solution of the one-equation turbulence model achieves closure of the Reynolds stress tensor. The Reynolds stresses are defined as

$$-\overline{u_i u_j} = 2\mu_t S_{ij} \tag{3.20}$$

where the mean strain-rate tensor (S_{ij}) is

$$S_{ij} \equiv \frac{1}{2}\left(\frac{\partial U_i}{\partial x_j} + \frac{\partial U_j}{\partial x_i}\right) \tag{3.21}$$

and U_i is the mean velocity. The turbulent eddy viscosity (μ_t) is given by

$$\mu_t = \tilde{\nu} f_{\nu 1}, \quad f_{\nu 1} = \frac{\chi^3}{\chi^3 + c_{\nu 1}^3}, \quad \chi = \frac{\tilde{\nu}}{\nu} \tag{3.22}$$

where ν is the kinematic viscosity, and $\tilde{\nu}$ is solved using

$$\frac{\mathrm{D}\tilde{\nu}}{\mathrm{D}t} = c_{b1}\tilde{S}(1-f_{t2})\tilde{\nu} - \left(c_{w1} f_w - \frac{c_{b1}}{\kappa^2} f_{t2}\right)\left(\frac{\tilde{\nu}}{d}\right)^2 + \frac{1}{\sigma}\left\{\frac{\partial}{\partial x_j}\left[(\nu+\tilde{\nu})\frac{\partial \tilde{\nu}}{\partial x_j}\right] + c_{b2}\frac{\partial \tilde{\nu}}{\partial x_j}\frac{\partial \tilde{\nu}}{\partial x_j}\right\} \tag{3.23}$$

$$\tilde{S} \equiv S + \frac{\tilde{\nu}}{\kappa^2 d^2} f_{\nu 2}, \quad f_{\nu 2} = 1 - \frac{\chi}{1 + \chi f_{\nu 1}} \tag{3.24}$$

d is the distance to the closest surface. The function f_w is as follows,

$$f_w = g\left[\frac{1 + c_{w3}^6}{g^6 + c_{w3}^6)}\right]^{\frac{1}{6}}, \quad g = r + c_{w2}\left(r^6 - r\right), \quad r \equiv \frac{\tilde{\nu}}{\tilde{S}\kappa^2 d^2} \tag{3.25}$$

The function f_{t2} serves to enable laminar-turbulent transitional effects of which will be discussed in Section 3.4.2.2. During simulations of a turbulent interaction, f_{t2} is suppressed by OVERFLOW. The calibration constants are c_{b1} = 0.1355, σ = 2/3, c_{b2} = 0.622, κ = 0.41, c_{w2} = 0.3, c_{w3} = 2, c_{v1} = 7.1, and

$$c_{w1} = \frac{c_{b1}}{\kappa^2} + \frac{1 + c_{b2}}{\sigma} \tag{3.26}$$

QCR redefines the turbulent stress tensor that the SA turbulence model uses. The QCR2000 [45] turbulent stress tensor is defined as

$$\tau_{ij,QCR} = \tau_{ij} - C_{nl1}\left[O_{ik}\tau_{jk} + O_{jk}\tau_{ik}\right] \tag{3.27}$$

The turbulent stresses are defined by the linear Boussinesq relation,

$$\tau_{ij} = 2\mu_t\left(S_{ij} - \frac{1}{3}\frac{\partial u_k}{\partial x_k}\delta_{ij}\right) - \frac{2}{3}\rho k\delta_{ij} \tag{3.28}$$

where the last term is neglected by OVERFLOW for one-equation turbulent models. O_{ik} is a normalized rotation tensor defined as

$$O_{ik} = \frac{\left(\frac{\partial u_i}{\partial x_k} - \frac{\partial u_k}{\partial x_i}\right)}{\sqrt{\frac{\partial u_m}{\partial x_n}\frac{\partial u_m}{\partial x_n}}} \tag{3.29}$$

The calibration constant C_{nl1} is specified to be 0.3. QCR2013 [46] is similar to QCR2000 with the only difference occurring in the turbulent stresses defined as

$$\tau_{ij,QCR} = \tau_{ij} - C_{nl1}\left[O_{ik}\tau_{jk} + O_{jk}\tau_{ik}\right] - C_{nl2}\mu_t\sqrt{2S^*_{mn}S^*_{mn}}\delta_{ij} \tag{3.30}$$

$$S^*_{ij} = S_{ij} - \frac{1}{3}\frac{\partial u_k}{\partial x_k}\delta_{ij} \tag{3.31}$$

and calibration constant C_{nl2} is specified as 2.5.

DDES [48, 49] is used to provide a higher fidelity simulation in the separated flow region. DDES is a hybrid RANS/LES methodology that provides RANS-based modeling in near-wall regions and LES-like behavior elsewhere, does so by altering the length scale used in the SA equation

$$d \to \tilde{d} \equiv d - f_d\max\left(0, d - C_{DES}\Delta\right) \tag{3.32}$$

where d is the distance to the closest surface, f_d is a function set to equal 0 in the near-wall region, C_{DES} is a calibration coefficient specified as 0.65, and Δ is the maximum spacing of the grid cell.

3.3.3.2 Amplification Factor Transport Transition Model (AFT2017b)

The AFT2017b transition model [47] is an enhancement to the transition model of Coder and Maughmer [50] and Coder [51]. AFT2017b solves two transport equations for the amplification factor

$$\frac{\partial\left(\rho\tilde{n}\right)}{\partial t}+\frac{\partial\left(\rho u_j\tilde{n}\right)}{\partial x_j}=\rho\Omega F_{crit}F_{growth}\frac{\mathrm{d}\tilde{n}}{\mathrm{d}Re_\theta}+\frac{\partial}{\partial x_j}\left[\left(\mu+\sigma_n\mu_t\right)\frac{\partial\tilde{n}}{\partial x_j}\right] \tag{3.33}$$

and modified intermittency

$$\frac{\partial\left(\rho\tilde{\gamma}\right)}{\partial t}+\frac{\partial\left(\rho u_j\tilde{\gamma}\right)}{\partial x_j}=c_1\rho SF_{onset}\left[1-exp\left(\tilde{\gamma}\right)\right]-c_2\rho\Omega F_{turb}\left[c_3exp\left(\tilde{\gamma}\right)-1\right]+\frac{\partial}{\partial x_j}\left[\left(\mu+\frac{\mu_t}{\sigma_\gamma}\right)\frac{\partial\tilde{\gamma}}{\partial x_j}\right] \tag{3.34}$$

where Ω is the vorticity magnitude, μ is the molecular viscosity, and σ_n = 1. Transition is considered to occur once the amplification factor ($\tilde{n}$) reaches a critical amplification factor (N_{crit}). N_{crit} is calculated through Mack's relation [52],

$$N_{crit}=-8.43-2.4\ln\left(\frac{\tau}{100}\right) \tag{3.35}$$

$$\tau=2.5\tanh\left(\frac{Tu_\infty\left(\%\right)}{2.5}\right) \tag{3.36}$$

The amplification factor transport equation (Equation 3.33) describes the growth and development of the approximate amplitude of the maximum Tollmien-Schlichting instability in the boundary layer (amplification factor) based on linear stability theory [53]. An integral shape factor, H_{12}, as

$$H_{12} = 0.376960 + \sqrt{\frac{H_L + 2.453432}{0.653181}} \tag{3.37}$$

where a local shape factor, H_L, is based on the work of Mentor [54]

$$H_L = \frac{d^2}{\mu} \left[\nabla \left(\rho \vec{u} \cdot \nabla d \right) \cdot \nabla d \right] \tag{3.38}$$

The function F_{crit} is defined as

$$F_{crit} = \begin{cases} 0, & Re_V < Re_{V,0} \\ 1, & Re_V \geq Re_{V,0} \end{cases} \tag{3.39}$$

$$Re_V = \frac{\rho S d^2}{\mu + \mu_t} \tag{3.40}$$

$$\frac{Re_{\nu,0}}{Re_{\theta,0}} = 0.246175 {H_{12}}^2 - 0.141831 H_{12} + 0.008886 \tag{3.41}$$

$$\log_{10} \left(Re_{\theta,0} \right) = 0.7 \tanh \left(\frac{14}{H_{12} - 1} - 9.24 \right) + \frac{2.492}{\left(H_{12} - 1 \right)^{0.43}} + 0.62 \tag{3.42}$$

The function F_{growth} is defined as

$$F_{growth} = \frac{H_{12}}{0.5482H_{12} - 0.5185}\left[1 + m\left(H_{12}\right)\right]\frac{l\left(H_{12}\right)}{2} \tag{3.43}$$

where Drela and Giles [53] developed the functions $l(H)$ and $m(H)$ defined as

$$l\left(H_{12}\right) = \frac{6.54H_{12} - 14.07}{H_{12}^2}, \quad m\left(H_{12}\right) = \left(0.058\frac{\left(H_{12} - 4\right)^2}{H_{12} - 1} - 0.068\right)\frac{1}{l\left(H_{12}\right)} \tag{3.44}$$

and

$$\frac{\mathrm{d}\tilde{n}}{\mathrm{d}Re_\theta} = 0.028\left(H_{12} - 1\right) - 0.0345exp\left[-\left(\frac{3.87}{H_{12} - 1} - 2.52\right)^2\right] \tag{3.45}$$

The modified intermittency transport equation (Equation 3.34) is based on the Menter intermittency model [54]. The function definitions are

$$F_{onset,1} = \min\left(\frac{\tilde{n}}{N_{crit}}, 2\right) \tag{3.46}$$

$$F_{onset,2} = \max\left[1 - \left(\frac{\mu_t}{3.5\mu}\right)^3, 0\right] \tag{3.47}$$

$$F_{onset} = \max\left[F_{onset,1} - F_{onset,2}\ , 0\right] \tag{3.48}$$

$$F_{turb} = exp\left[-\left(\frac{\mu_t}{2\mu}\right)^4\right] \tag{3.49}$$

Calibration constants [54] for the modified intermittency transport equation are c_1 = 100, c_2 = 0.06, c_3 = 50, and σ_γ = 1.0.

The AFT transition model interacts with the SA turbulence model through the redefined function f_{t2} as

$$f_{t2} = c_{t3}\left[1 - exp\left(\tilde{\gamma}\right)\right] \tag{3.50}$$

where c_{t3} = 1.2. For DDES simulations, the modified f_d function

$$f_{d,DDES} = \gamma f_d \tag{3.51}$$

ensures that the LES-branch does not become active in an attached, laminar boundary layer.

CHAPTER 4
RESULTS AND DISCUSSION

This chapter highlights the RANS and DDES simulations. The determination of N_{crit} will be discussed as well as a qualitative and quantitative comparison of the simulated XSBLI phenomena to the experimental data. The flow parameters analyzed are surface pressures, velocity profiles, and surface skin frictions. As previously mentioned, the simulations were obtained through the NASA-developed OVERFLOW solver with the cylinder leading-edge positioned 7 diameters downstream of the plate leading-edge. OVERFLOW 2.2 is a three-dimensional time-marching implicit RANS compressible gas dynamics solver that uses structured overset grid systems [21]. RANS simulations are defined as fully turbulent (SA-QCR) and transitional (SA-QCR-AFT) while DDES simulations are as DDES-SA-QCR and DDES-SA-QCR-AFT for fully turbulent and transitional simulations

4.1 Determination of N_{crit}

SA-QCR-AFT simulations have the option of influencing the location of laminar-turbulent transition within the boundary layer. By specifying the value of N_{crit} in the simulations, transition is predicted at a respective location along the streamwise direction of the flat plate. Lower N_{crit} values allow for boundary layer transition to occur further upstream. Combs et al. [17] and Lash et al. [18-20] positioned the cylinder such that the separation shock would introduce a SBLI within a transitioning boundary layer. As such, the objective of the computational study was to replicate the experimental condition. The objective was completed by studying the surface skin friction (normalized vorticity magnitude) along the flat plate geometry for varying values of N_{crit}. The N_{crit} value was chosen such that transition occurred naturally along the surface without the presence of additional flow features. Therefore, the model geometry did not include the standing cylinder.

Figure 4.1 displays the boundary layer transition location along the flat plate for each respective N_{crit} value. The occurrence of laminar-turbulent transition within the boundary layer can be regarded as the deviation of the surface skin friction from the general trend observed by all N_{crit} values. A N_{crit} value of 5 introduces a transitional boundary layer at approximately 6 diameters downstream of the plate leading-edge. This allows for a boundary layer transition to occur approximately 1 diameter upstream of the standing cylinder leading-edge.

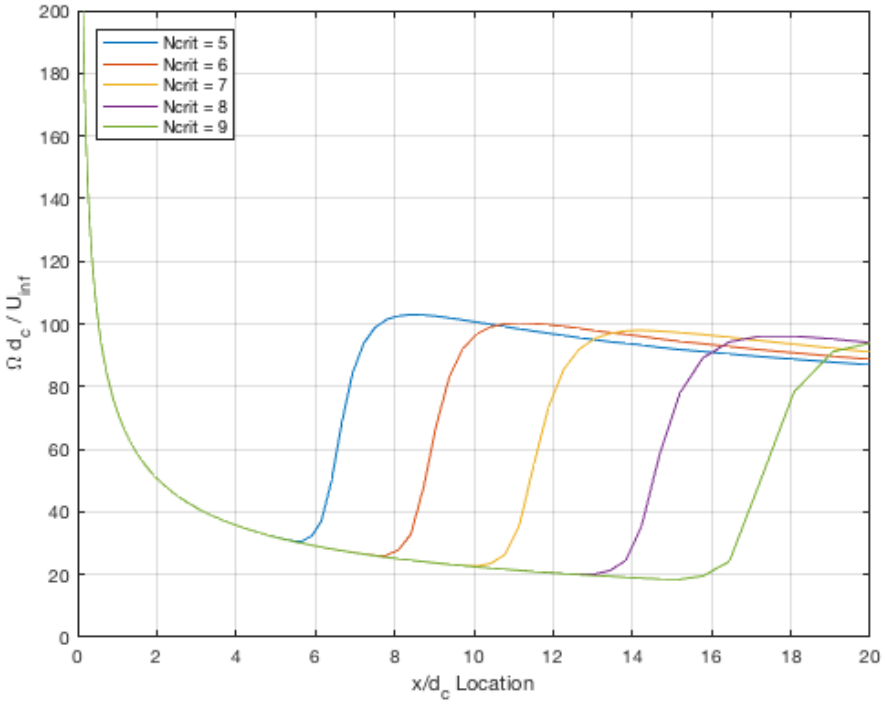

Figure 4.1 Laminar-turbulent transition locations along a flat plate geometry for N_{crit} values 5-9.

4.2 RANS Results

RANS simulations did exhibit the XSBLI phenomena present in the experiment but did not fully converge, obtaining a normalized residual on the order of 10^{-3} for both SA-QCR and SA-QCR-AFT simulations in the region of interest. Note that SA-QCR simulations did show better convergence approaching a normalized residual on the order of 10^{-4}. Due to the less than optimal convergence, the XSBLI phenomena were compared with the experimental date in a primarily

qualitative manner. Additional analysis of the flow parameters was conducted to provide predictive capabilities of steady RANS in capturing XSBLI phenomena. Solutions on the initial grid system provide only a visual comparison of the flow features while the modified grid system provides both a qualitative and quantitative comparison to experimental data.

4.2.1 SA-QCR Results

As expected, SA-QCR simulations on either grid system do not predict an UI shock. Because laminar-turbulent transition is not modeled, the predicted XSBLI phenomena replicate the experimental work of Lash et al. [18-20] with the cylinder positioned 25 diameters downstream of the plate leading-edge. The computed density-gradient magnitude contours (i.e. numerical Schlieren) for both grid systems are visually represented in Figure 4.2. The distorted section of the oblique shock upstream of the cylinder is due to the mesh being too coarse to properly capture the flow feature. The distortion does not directly affect the flow physics downstream in the SA-QCR simulations; however, it was found to influence the DDES-SA-QCR simulations. This phenomenon will be further discussed in Section 4.3.

Nevertheless, SA-QCR simulations did capture the separation and reattachment shocks. Additionally, the SA-QCR simulations captured the separation region located between the separation and reattachment shocks. Table 4.1 compares the triple point height, separation shock distance, and reattachment shock distance to the experimental reference time-averaged values. Note the accuracy of the measurements are $\pm 0.36\%$ for h_{tp}, $\pm 0.22\%$ for $\lambda_{s,1}$, and $\pm 1.35\%$ for $\lambda_{s,2}$ due to the refinement mesh spacing. The SA-QCR simulations of both grid systems produce similar measurements to one another. Additionally, the SA-QCR simulations show good agreement with the measurements of h_{tp}, $\lambda_{s,1}$, and $\lambda_{s,2}$ in the experimental reference

Computed Mach contours for the SA-QCR simulations are shown in Figure 4.3. The same flow features prominent in the numerical Schlieren images are observed by the Mach contour plots. The blue and green contours emphasize the subsonic separation region, displaying one large vortex. Additionally, an indentation of the Mach contours appears just downstream of the separation-reattachment shock intersection. A secondary indentation develops downstream of the subsonic separation region, located at the cylinder-plate junction.

Table 4.1 Measurements of XSBLI phenomena for SA-QCR simulations

	Initial Grid System	**Modified Grid System**	**Experimental Reference [18]**
h_{tp}/d_c	1.45	1.44	1.39
$\lambda_{s,1}/d_c$	2.19	2.16	2.24
$\lambda_{s,2}/d_c$	0.38	0.40	0.37

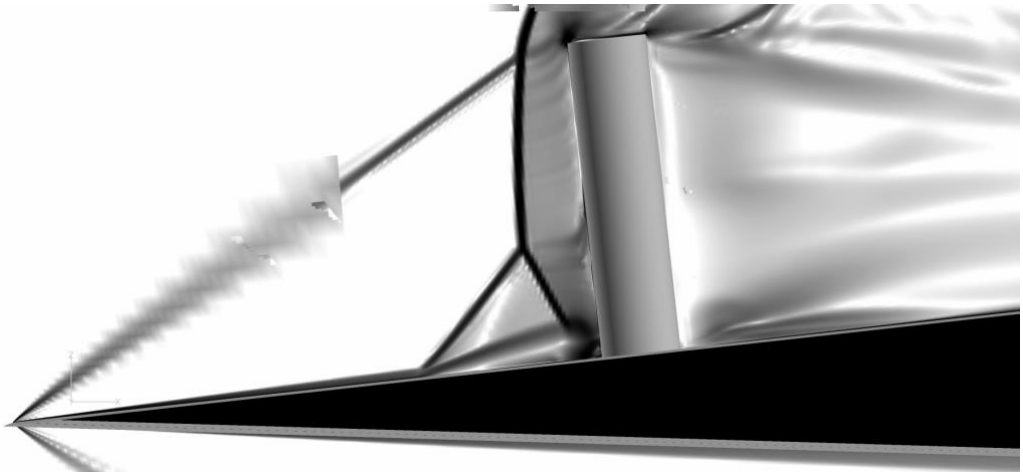

(a)

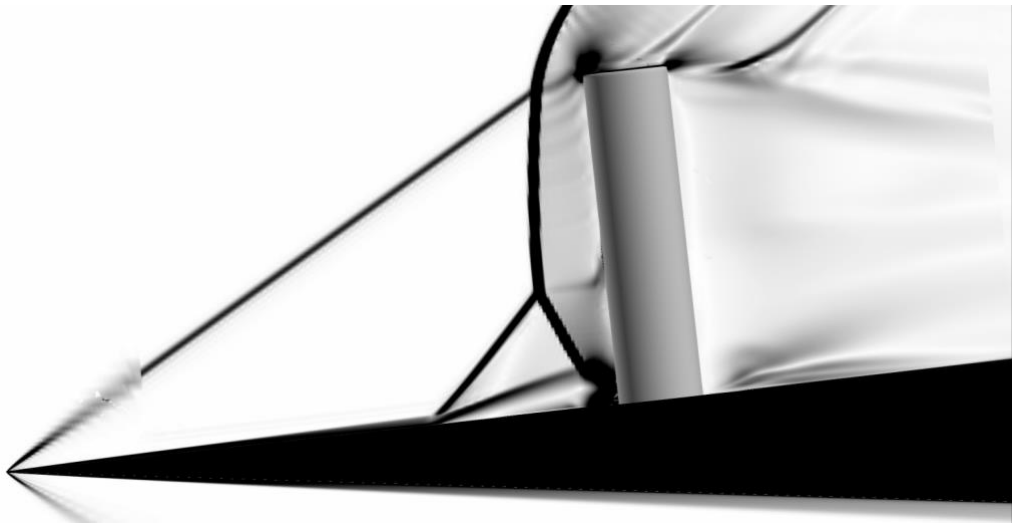

(b)

Figure 4.2 Numerical Schlieren of SA-QCR simulations for the (a) initial grid system (b) modified grid system. Flow is from left to right.

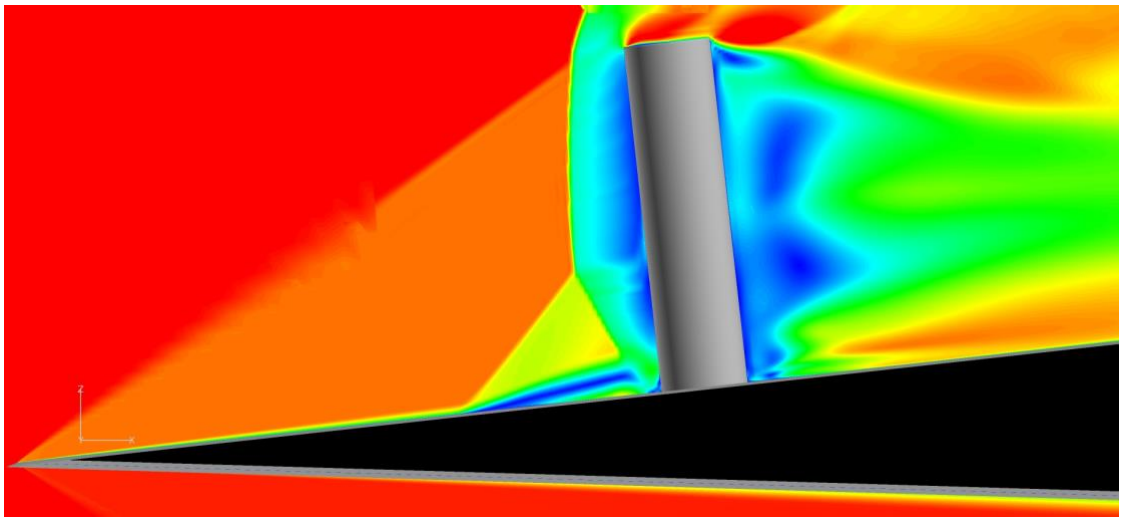

(a)

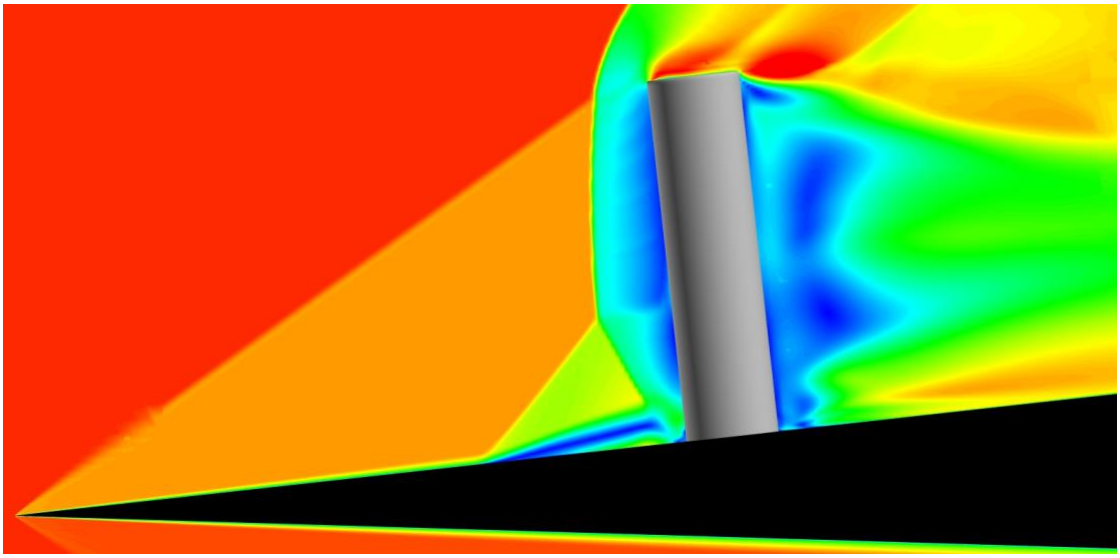

(b)

Figure 4.3 Mach contours of SA-QCR simulations for the (a) initial grid system (b) modified grid system. Flow is from left to right. Note the slight variation in contour values; the purpose of these images is to visually compare the differences in flow features.

4.2.1.1 Surface Pressures

The non-dimensional surface pressure contours provide further insight on the separation shock and reattachment shock locations denoted as the region of separation. As previously mentioned, the UI shock is not present in the SA-QCR simulations. Experimental efforts to display and measure the surface pressure for a standing cylinder configuration have been conducted by Lash et al. [19] through the use of fast-response PSP imaging.

The calculated surface pressure contours are presented in Figure 4.4. The separation shock is evident through the sharp pressure gradient denoted by the color change from blue to green. The reattachment shock is present through the thin region of a gradient just upstream of the cylinder, producing similar pressures to the freestream surface pressure. Note the higher resolution on both the separation shock and reattachment shock in the spanwise direction of the modified grid system. Surface pressures in the spanwise direction seems to be visually symmetric about the centerline.

Further detail of the calculated surface pressures is given through the off-center surfaces pressures plotted in Figure 4.5. The off-center surface pressures were computed on the surface $\pm 0.5d_c$ and $\pm 1.0d_c$ in the spanwise direction. Each pair of off-center surface pressures show no discernable difference in magnitude and peak locations in the region of interest. Local strong gradients in the surface pressure reveal the locations of the separation and reattachment shocks. The peaks in surface pressure occur further downstream as the distance in the spanwise direction is increased displaying the curvature of the shock system about the cylinder. Note that all centerline and off-center surface pressures were computed from the modified grid system simulations.

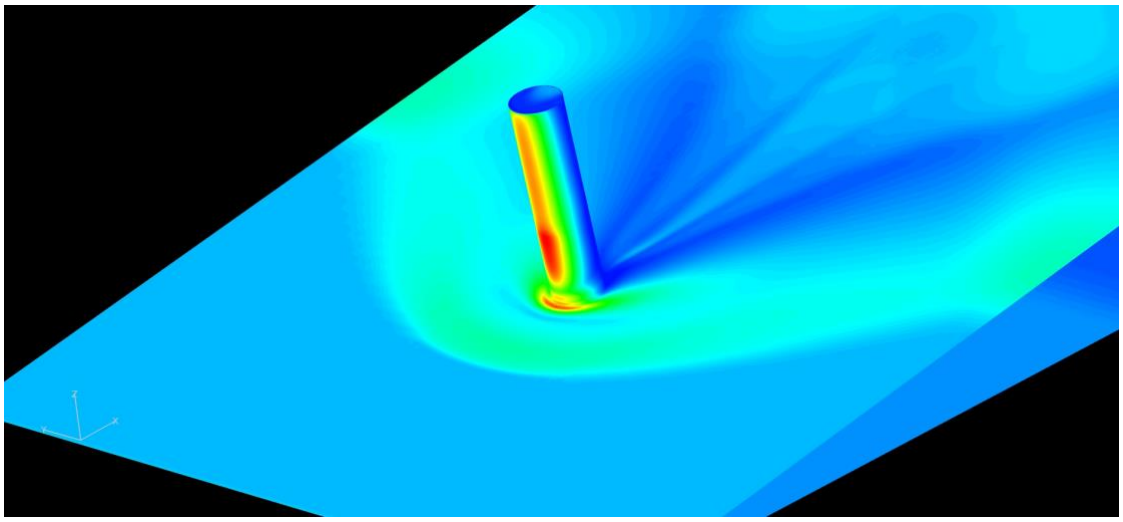

(a)

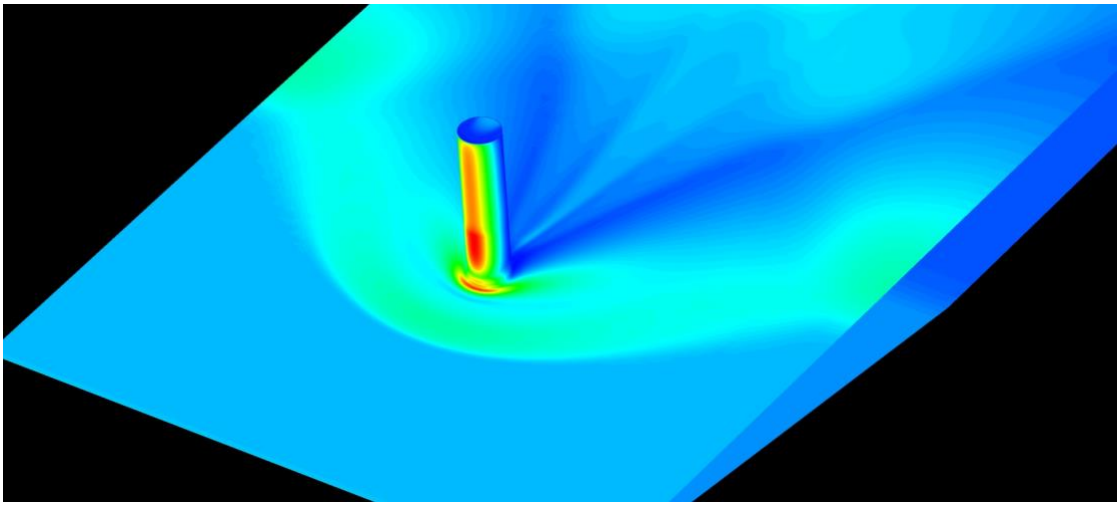

(b)

Figure 4.4 Surface pressure contours of SA-QCR simulations for the (a) initial grid system (b) modified grid system. Flow is from the bottom-left to top-right.

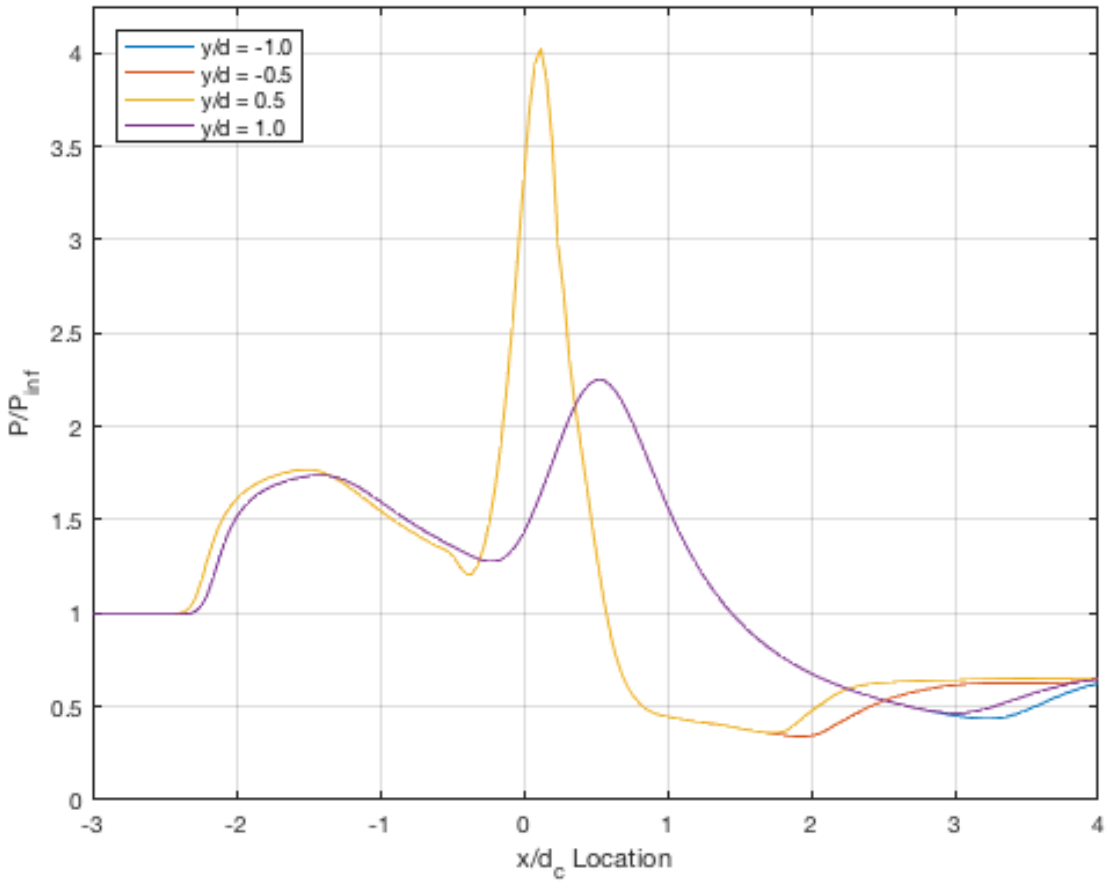

Figure 4.5 SA-QCR-computed off-center surface pressures normalized by freestream surface pressure. Zero denotes the location of the cylinder leading edge.

4.2.1.2 Velocity Profiles

The streamwise velocity profiles located upstream of the UI shock, downstream of the UI shock, and within the separation region are given by Figure 4.6. Note that the UI shock is not present in the SA-QCR simulations but is used for reference from the SA-QCR-AFT simulations to define the location of the velocity profiles. The location of the velocity profiles will be further discussed in Section 4.2.2.2. The velocity profile downstream of the UI shock and upstream of the UI shock both have initial values of zero before abruptly increasing to approximately 1.04. The velocity profile just downstream of the UI shock shows that a phenomenon slightly delays the growth of the streamwise velocity. The separation region velocity profile begins as upstream flow near the surface denoting a vortex is circulating in the region. The region of the initial plateau in the separation velocity profile indicates the height of the separation bubble. The secondary plateau represents the separation shock location. The final velocity gradient present in all the velocity profiles is representative of the inviscid oblique shock.

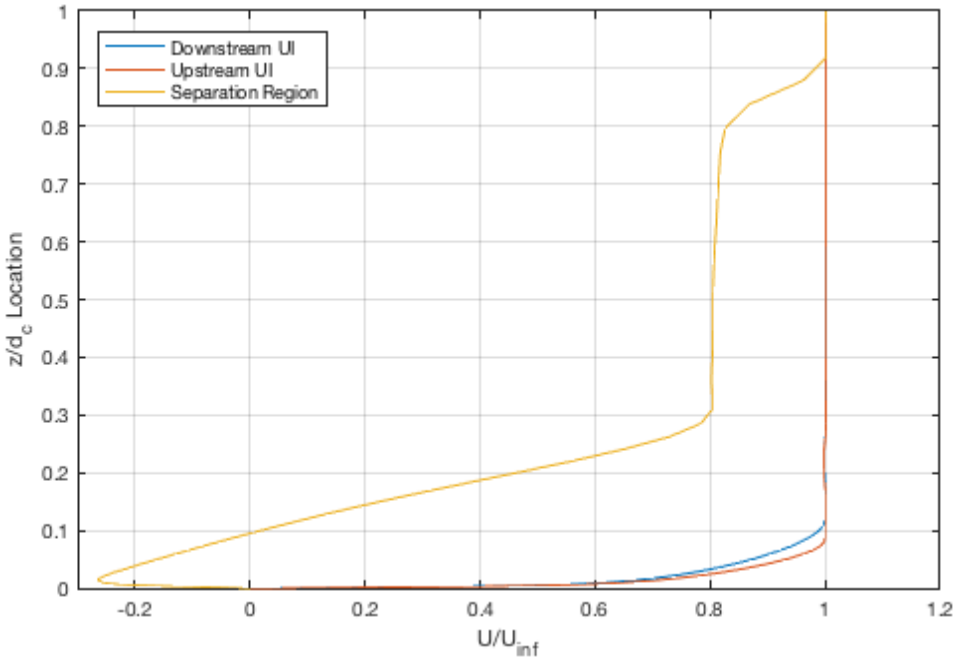

Figure 4.6 SA-QCR-computed velocity profiles normalized by freestream velocity downstream of the inviscid oblique shock.

4.2.2 SA-QCR-AFT Results

Unlike the SA-QCR simulations, the SA-QCR-AFT simulations captured the UI feature, but it resembled a compression wave more than a true shock. The numerical Schlieren images are illustrated in Figure 4.7. The UI shock appears less prominent than the separation and reattachment shocks, but with the addition of the UI shock, the separation shock appears to be weakened. Note that the UI shock intersects the overset grid boundary of the coarse mesh in the initial grid system which partially motivated the modified grid system.

The measurements of the XSBLI phenomena are presented in Table 4.2. Note the previously mentioned uncertainties still apply as well as an uncertainty of the UI shock location (UI/d_c) as $\pm 0.12\%$. The SA-QCR-AFT simulations tended to over-predict the relevant features the experimental data while the turbulent simulations under-predicted the separation shock location.

Table 4.2 Measurements of XSBLI phenomena for SA-QCR-AFT simulations

	Initial Grid System	**Modified Grid System**	**Experimental Reference [18]**
h_{tp}/d_c	1.50	1.48	1.39
$\lambda_{s,1}/d_c$	2.42	2.28	2.24
$\lambda_{s,2}/d_c$	0.38	0.40	0.37
UI/d_c	3.35	3.24	3.90 - 4.20

The visualization of the UI shock existing as a compression wave is further emphasized by the Mach contours in Figure 4.8. Rather than representing a single feature as shown in the numerical Schlieren images, the UI feature appears to emerge from the separation shock. All other XSBLI phenomena show good agreement with the SA-QCR RANS simulations. Due to the aforementioned overset boundary condition of the initial grid system, a subtle variation in Mach contours is located in the upper region upstream of the cylinder.

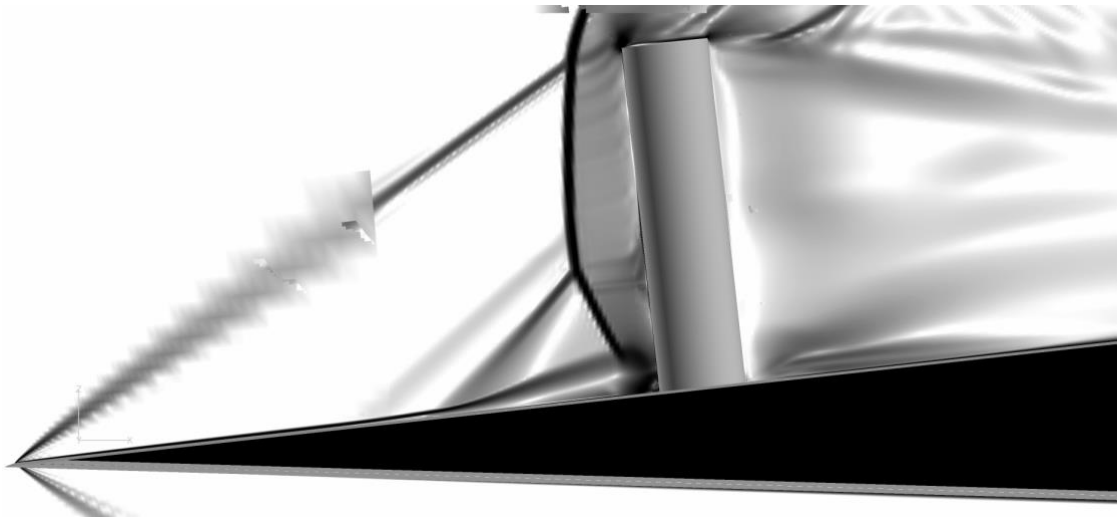

(a)

(b)

Figure 4.7 Numerical Schlieren images of SA-QCR-AFT simulations for the (a) initial grid system (b) modified grid system. Flow is from left to right.

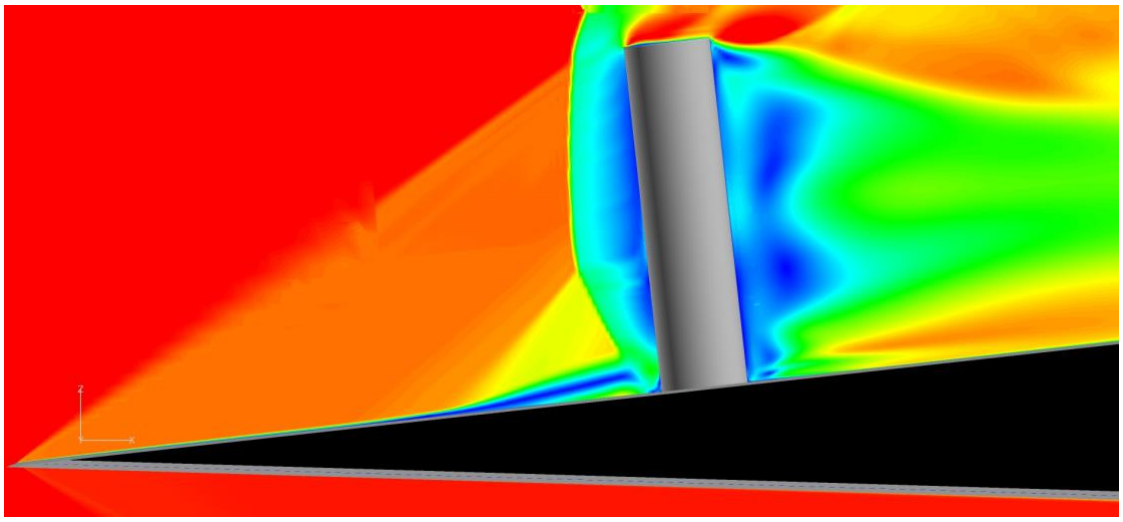

(a)

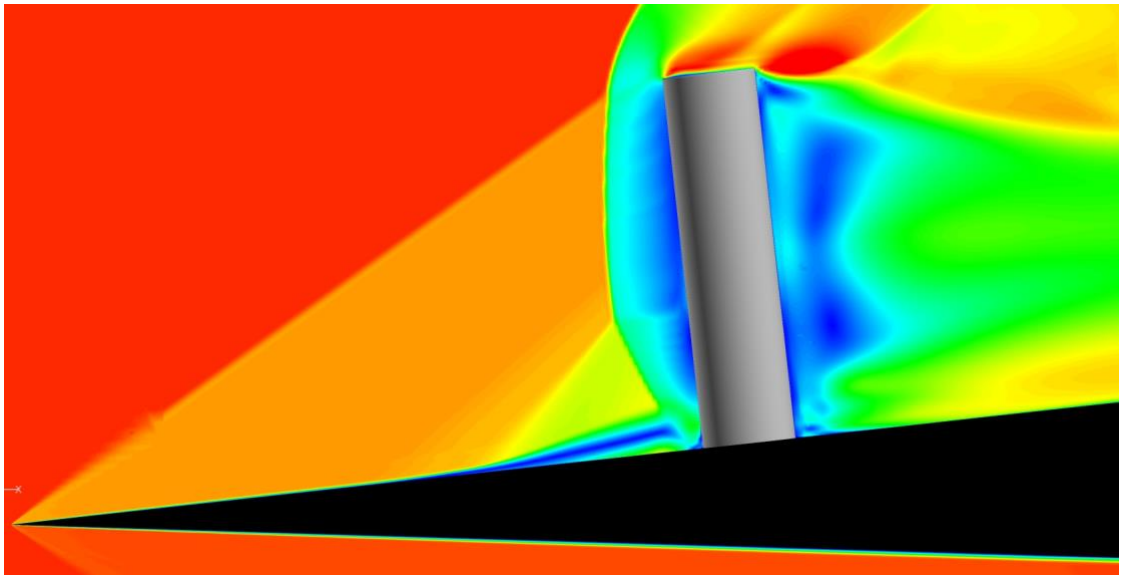

(b)

Figure 4.8 Mach contours of SA-QCR-AFT simulations for the (a) initial grid system (b) modified grid system. Flow is from left to right. Note the slight variation in contour values; the purpose of these images is to visually compare the differences in flow phenomena.

Another flow parameter used in studying the behavior of XSBLI phenomena is the centerline surface skin friction plotted in Figure 4.9. A decrease in skin friction is associated with an increase in boundary layer thickness for zero pressure gradient. The SA-QCR simulation has a prominent shock denoted by the sharp increase in skin friction after the initial decrease. The SA-QCR-AFT simulation, however, has two gradual increases in the skin friction indicating the UI feature and separation shock locations. The gradual increase indicates the shocks are weaker representing a behavior more similar to a compression wave. The initial increase in boundary layer thickness behaves like a compression ramp reinforcing the presence of a UI feature. Additionally, the UI feature causes the boundary layer to thicken, conversely, obscuring the origin of the phenomenon.

Additional skin friction analysis is plotted in Figure 4.10 and Figure 4.11, displaying the regions of separation along the plate and cylinder surface. A region of separation is denoted by a negative value in the spanwise vorticity. On the plate surface, RANS simulations produce one large vortex, showing good agreement with the results of Lindorfer et al. [33] However, the SA-QCR-AFT simulation predicts separation further upstream, corresponding with the UI shock location. On the leading-edge of the cylinder surface, three regions of separation are apparent. Note that these regions are significantly smaller in size than the separation regions along the plate surface. These three regions correspond roughly with the location of the triple-point height, the interaction of the reattachment shock and separation bubble, and the cylinder-plate junction. The vortex at the shock-separation interaction is significantly weaker than the other vortices predicted.

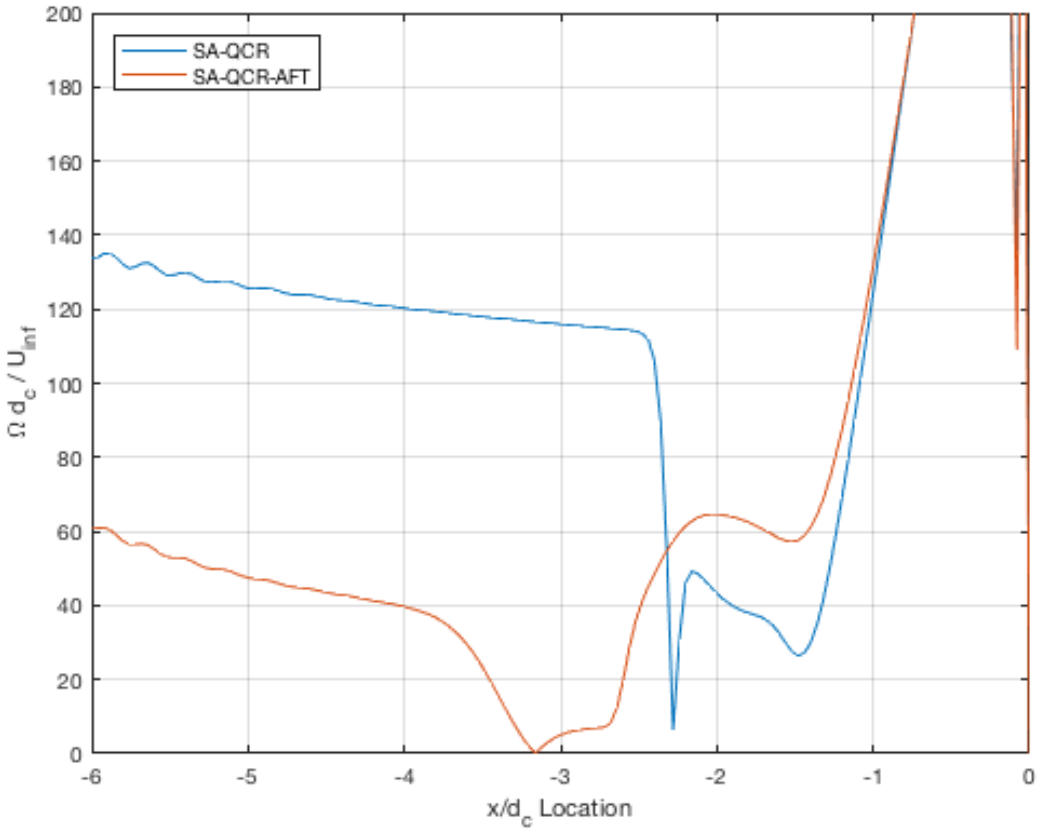

Figure 4.9 Steady normalized surface skin friction along the centerline.

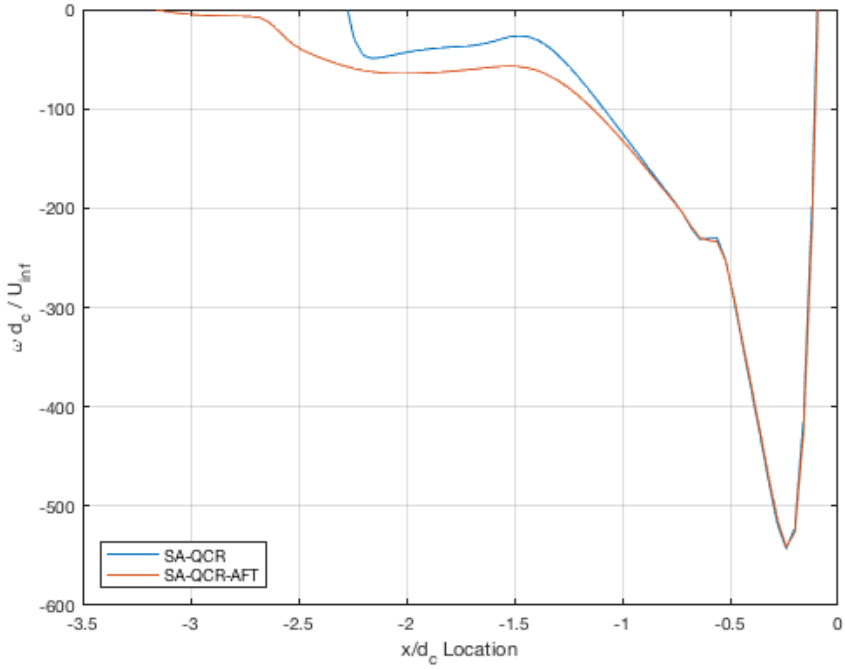

Figure 4.10 Steady normalized vorticity in the spanwise direction along the plate centerline.

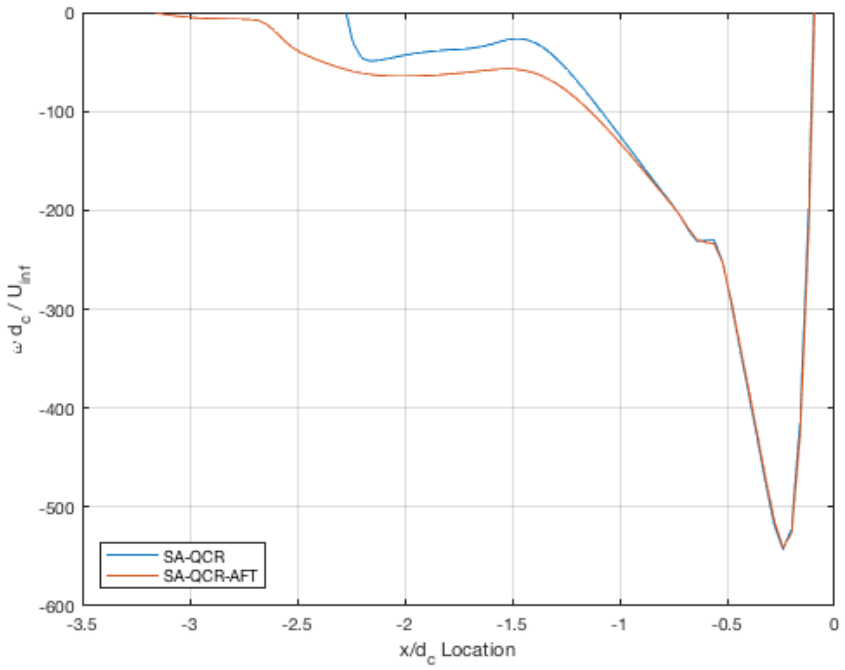

Figure 4.11 Steady normalized vorticity in the spanwise direction along the cylinder centerline. Note the log

4.2.2.1 Surface Pressures

The computed surface pressures are pictured in Figure 4.12. The presence of the UI feature is evident upstream of the separation shock. As previously mentioned, the UI feature appears to emerge from the separation shock. Additionally, the reattachment shock is more prominent in the SA-QCR-AFT simulations than the SA-QCR simulations. All other XSBLI phenomena show good agreement with the SA-QCR simulations and the experimental data. The UI feature is contained within the refinement mesh of the initial grid system which is the motivation behind expanding the refinement mesh in the spanwise direction. The UI feature in the modified grid solution shows better agreement with the experimental reference in the spanwise direction extending outward to the tunnel walls.

Further detail of the computed surface pressures is plotted in Figure 4.13 and Figure 4.14. The SA-QCR simulation agrees with the experimental XSBLI data in terms of matching the peak pressure location. However, the SA-QCR simulation does not predict the initial pressure increase around x/d = -5 which represents the UI feature, and it over-predicts the magnitude of the surface pressures after separation. Similar to the turbulent simulations, the SA-QCR-AFT simulation over-predicts the value of the peak surface pressures, but the SA-QCR-AFT centerline surface pressures show better phenomenological agreement with the experimental data with the indication of a gradual increase before the separation region. This gradual increase indicates that a UI feature is influencing the separation region, promoting separation to occur further upstream. This region upstream of the separation shock is further enforced by the velocity profile downstream of the UI feature that will be discussed in Section 4.2.2.2. The off-center surface pressures in Figure 4.14 display similar results to the SA-QCR simulations. Similar to the centerline surface pressures, a UI feature is indicated by the gradual rise in the surface pressure upstream of the separation shock. The pair of off-center surface pressures show no discernable difference in the spanwise direction within the region of interest.

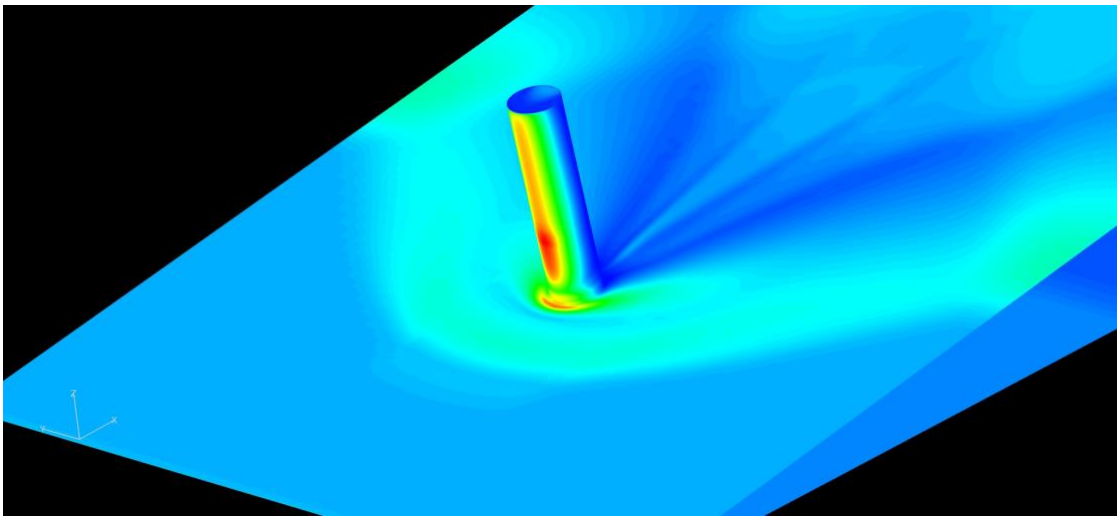

(a)

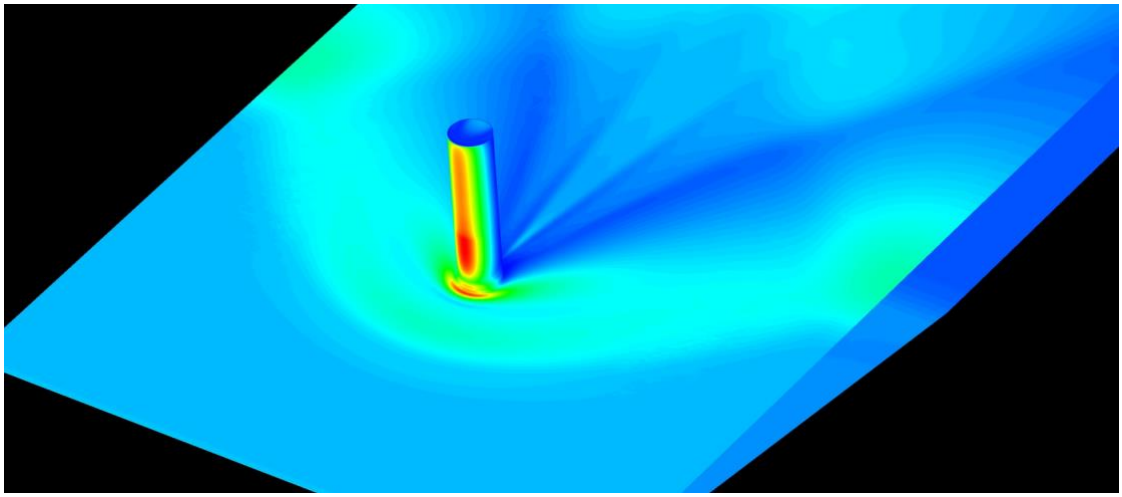

(b)

Figure 4.12 Surface pressure contours of SA-QCR-AFT simulations for the (a) initial grid system (b) modified grid system. Flow is from bottom-left to top-right.

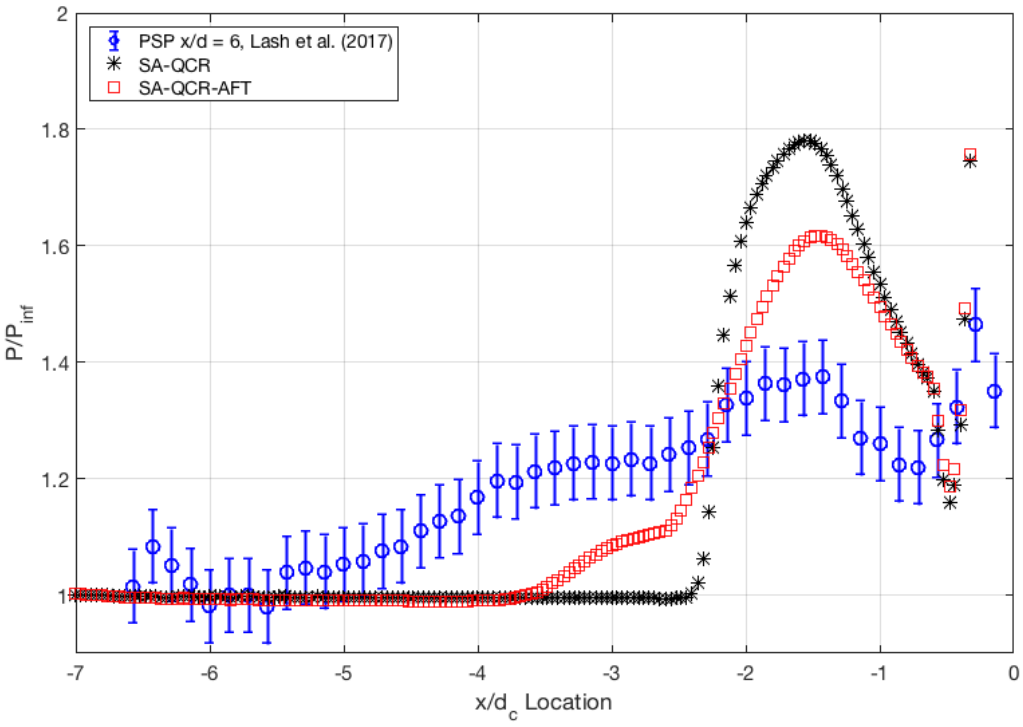

Figure 4.13 SA-QCR-AFT computed centerline surface pressures normalized by freestream surface pressure. Zero denotes the location of the cylinder leading edge.

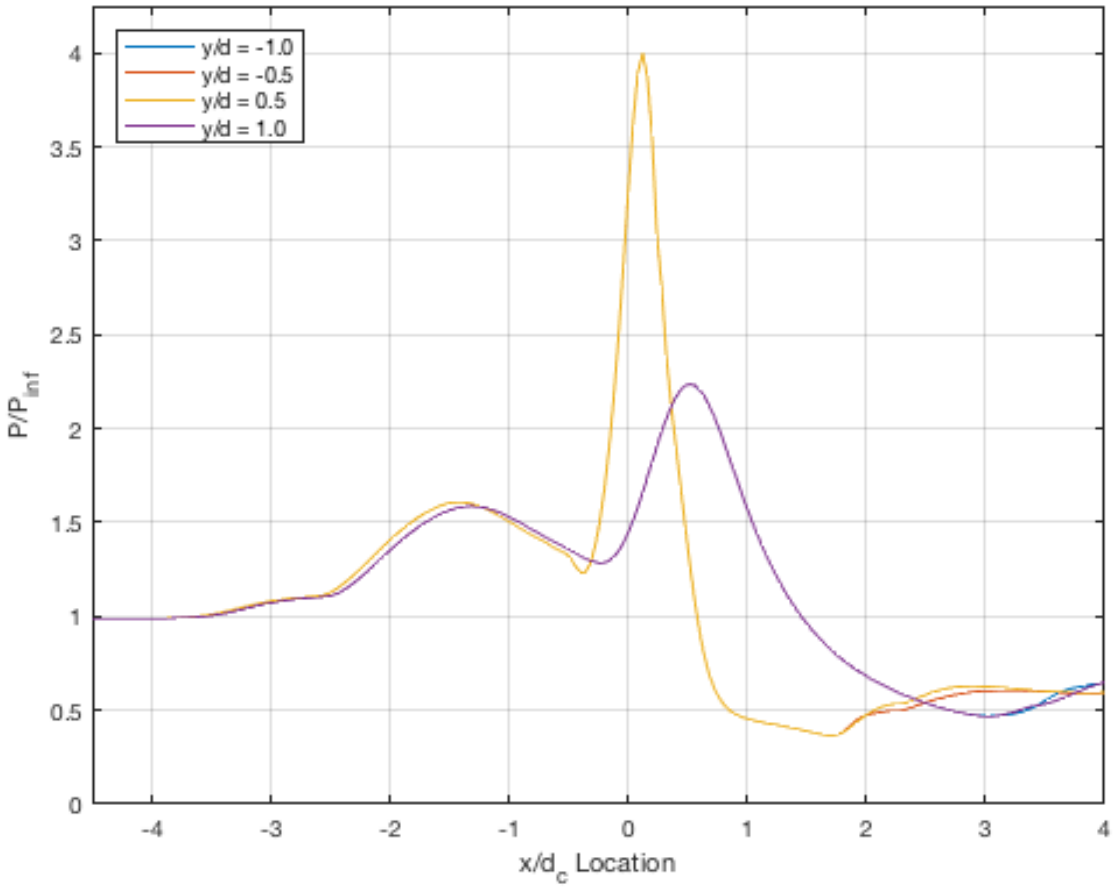

Figure 4.14 SA-QCR-AFT computed off-center surface pressures normalized by freestream surface pressure. Zero denotes the location of the cylinder leading edge.

4.2.2.2 Velocity Profiles

Three locations of interest were identified for extracting velocity profiles. These are illustrated in Figure 4.15. The velocity profile upstream of the UI feature depicts the flow with no influence from the XSBLI phenomenon. The velocity profile downstream of the UI feature was selected to study the effects the UI feature had on the boundary layer characteristics. Lastly, velocity profile in the separation region was specified to obtain further detail of the separation region developed by the XSBLI phenomena.

Figures 4.16-19 plot the SA-QCR-AFT and SA-QCR computed velocity profiles in each location including a near-wall profile of the separation region where only the shear layer is present. Figure 4.16 depicts the region upstream of the UI feature. Both RANS simulations behave similarly with a slight deviation occurring in the near-wall region. Downstream of the UI feature, shown in Figure 4.17, the SA-QCR-AFT simulation has a prolonged region of lower streamwise velocity due to the presence of the UI feature. Additionally, the SA-QCR-AFT simulation predicts flow propagating upstream within the subsonic boundary layer while the SA-QCR simulation does not. The upstream flow further highlighted that separation is present further upstream in the SA-QCR-AFT simulation. Within the separation region, plotted by Figure 4.18, the SA-QCR-AFT simulation has a near-linear increase consisting of two peaks in velocity whereas the SA-QCR simulation has a singular sharp gradient representing the separation shock. The first local peak in the SA-QCR-AFT simulation is depicted as the separation shock showing a larger gradient than the second local peak, portraying the UI feature. The comparison between the two gradients further emphasizes that the UI feature behaves as a compression wave in the SA-QCR-AFT simulations. Lastly in Figure 4.19, the near-wall velocity profile of the separation region exhibits a vortex present in the region indicated by the advancement of flow upstream. Both simulations behave similarly, seeming to capture only one large vortex, but the SA-QCR-AFT simulation predicts a stronger vortex due to the larger magnitude in upstream velocity.

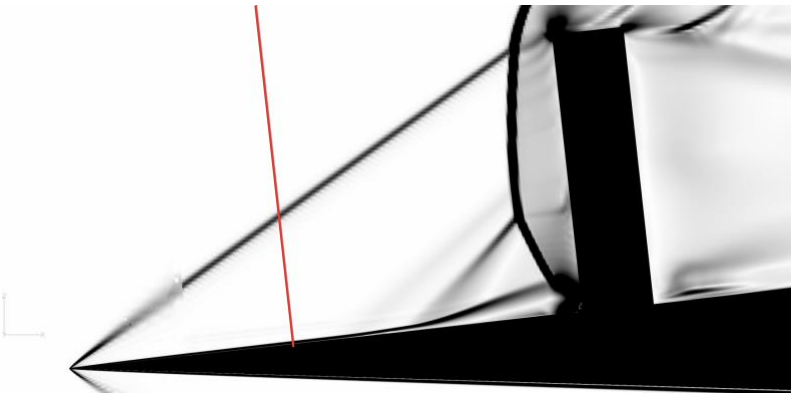

(a)

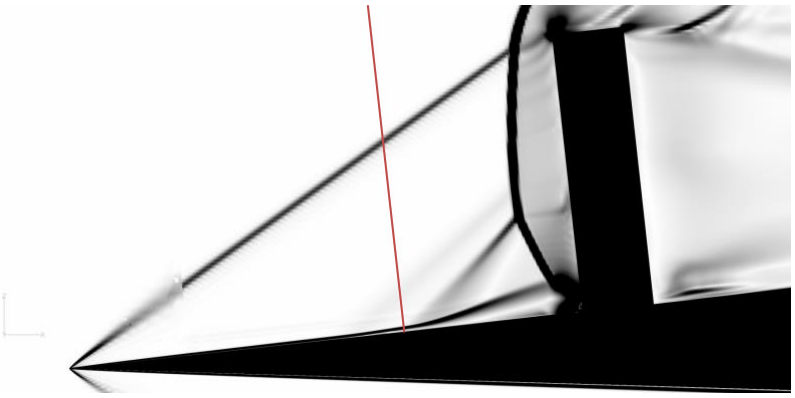

(b)

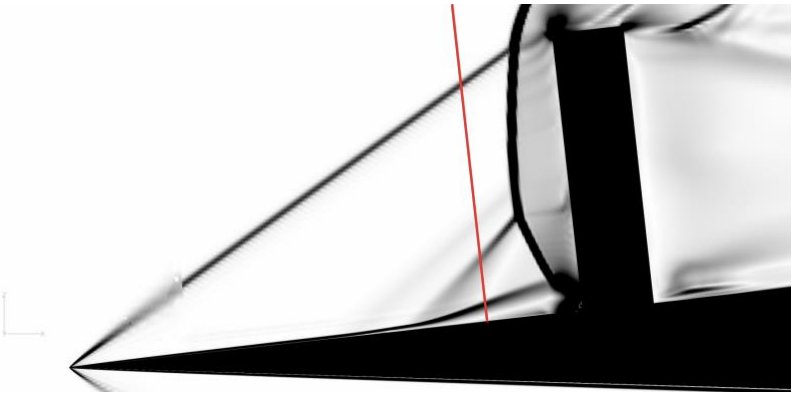

(c)

Figure 4.15 Location of velocity profiles (a) upstream of UI shock (b) downstream of UI shock (c) separation region.

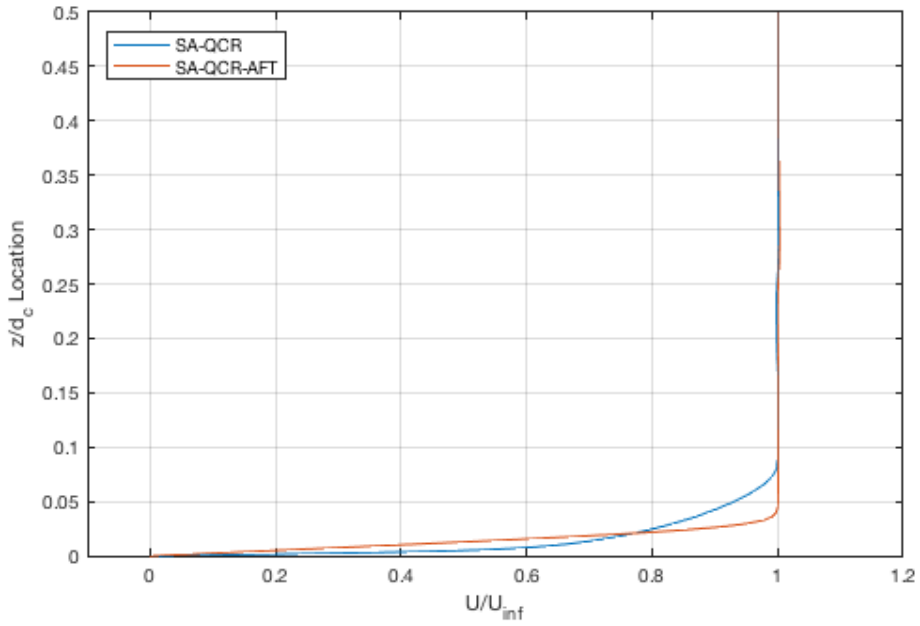

Figure 4.16 Steady velocity profiles upstream of UI shock normalized by freestream velocity downstream of the inviscid oblique shock.

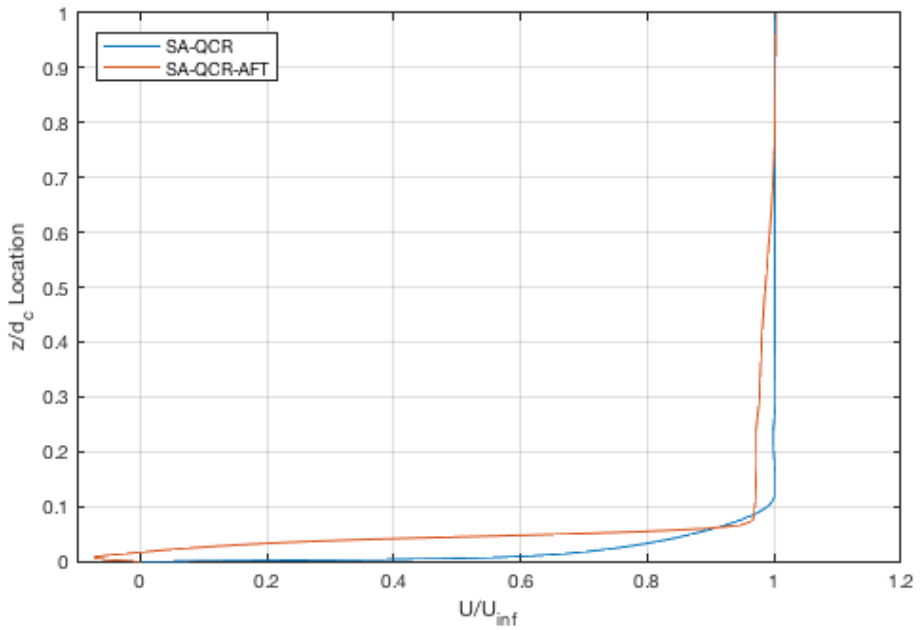

Figure 4.17 Steady velocity profiles downstream of UI shock normalized by freestream velocity downstream of the inviscid oblique shock.

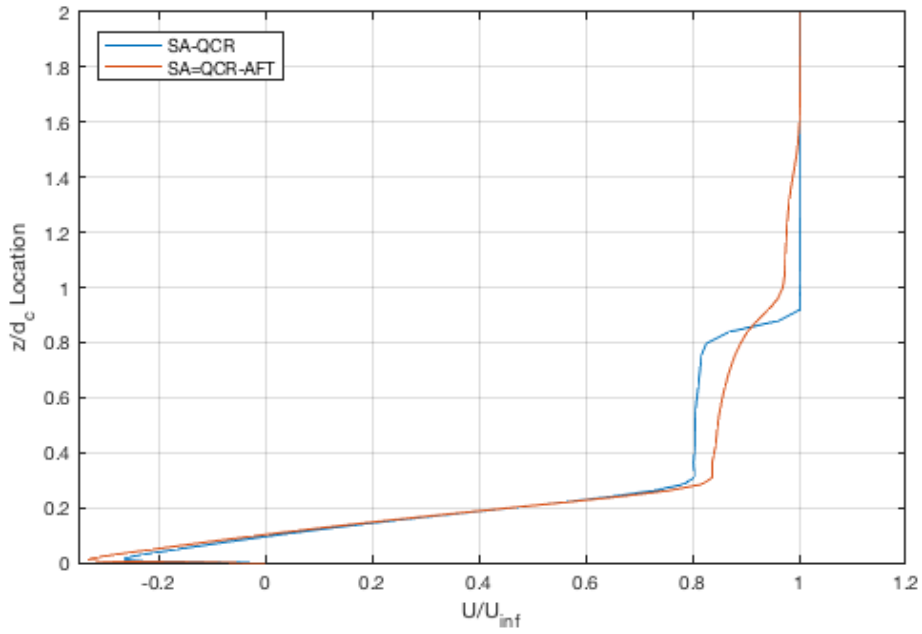

Figure 4.18 Steady velocity profiles in separation region normalized by freestream velocity downstream of the inviscid oblique shock.

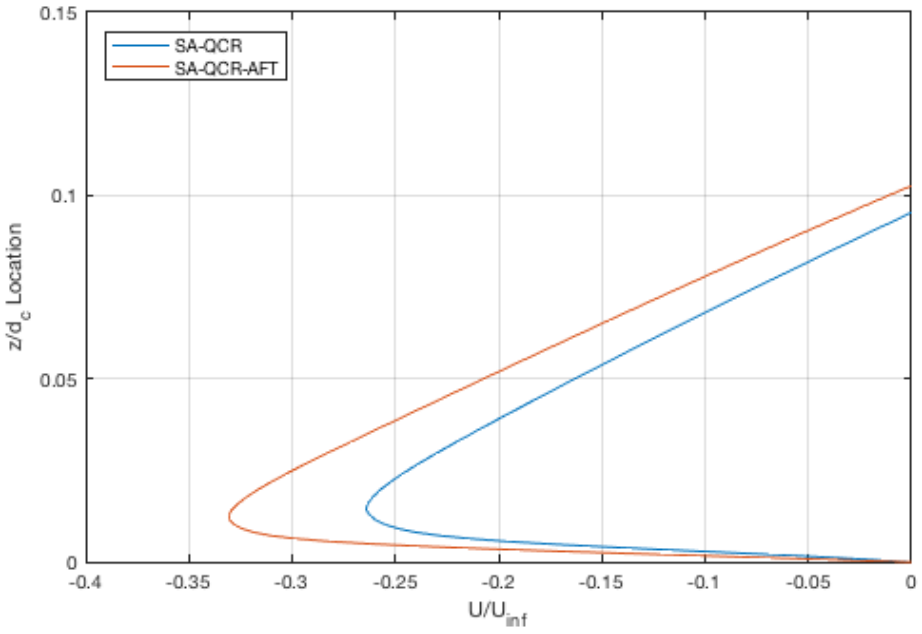

Figure 4.19 Near-wall steady velocity profiles in separation region normalized by freestream velocity downstream of the inviscid oblique shock.

4.3 Hybrid RANS/LES (DDES) Results

DDES methods were employed to capture the dynamic behavior in the XSBLI phenomena as seen in the experimental data. The DDES simulations were run with SA-QCR and SA-QCR-AFT methods providing further detail in the separation region. The initial grid system simulations showed promising results with predicted dynamic behavior, but these results were called into question due to the grid system. As such, the initial grid system will not be used for any DDES comparisons to the experimental data. The modified grid system simulations reached a visually converged state after transitioning from a RANS solution to a hybrid RANS/LES solution from which visual and quantitative results are obtained

4.3.1 DDES-SA-QCR Results

Consistent with the RANS results, the DDES-SA-QCR simulations did not capture an UI shock. As the simulation progresses from a RANS-based modeling solution to a hybrid RANS/LES solution, the bifurcated shock system expands both upstream and in the wall-normal direction. Curvature of the reattachment shock towards the separation region then occurs after the shock system expansion. Additionally, an expansion wave forms just downstream of the separation shock, redirecting the flow back towards the plate further upstream than the reattachment shock location. As such, the separation region is significantly reduced in relation to the RANS simulations. However, once these features have formed, the simulations reach a visually converged state illustrated in Figure 4.20.

The converged Mach contours displayed in Figure 4.21 provide further detail on the expansion wave present within the separation region. The expansion wave immediately increases the downstream streamwise velocity. The sharp increase in the velocity and accompanying expansion wave is not present in the RANS simulations. In the near-wall region below the expansion wave, the subsonic region contains a curved profile at the end of the increase in separation thickness. Additionally, small separation pockets appear to form at the surface just upstream of the reattachment shock.

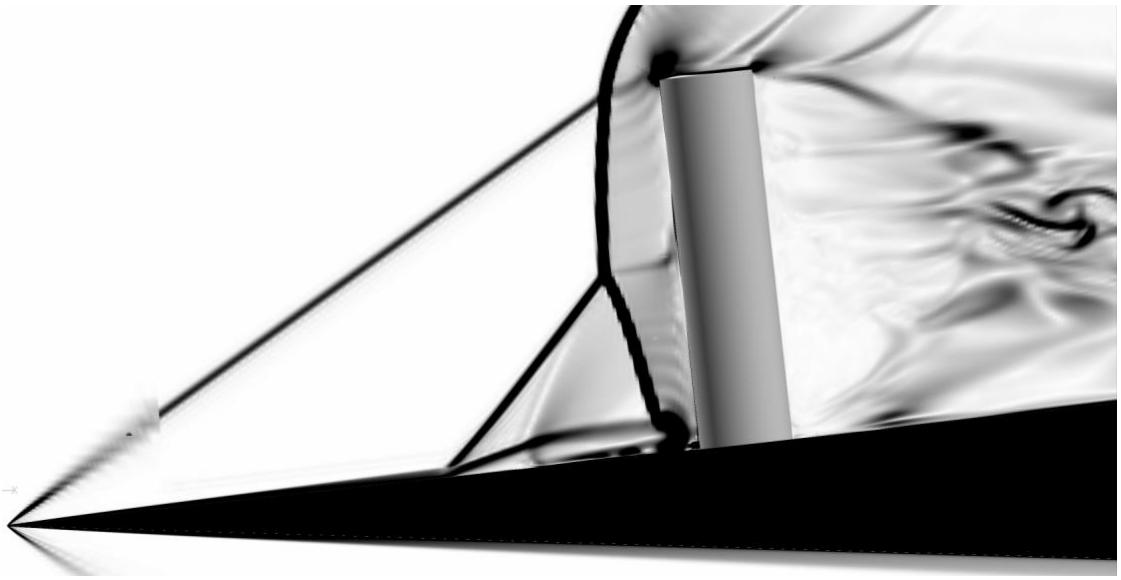

Figure 4.20 DDES-SA-QCR numerical Schlieren image after convergence. Flow is from left to right.

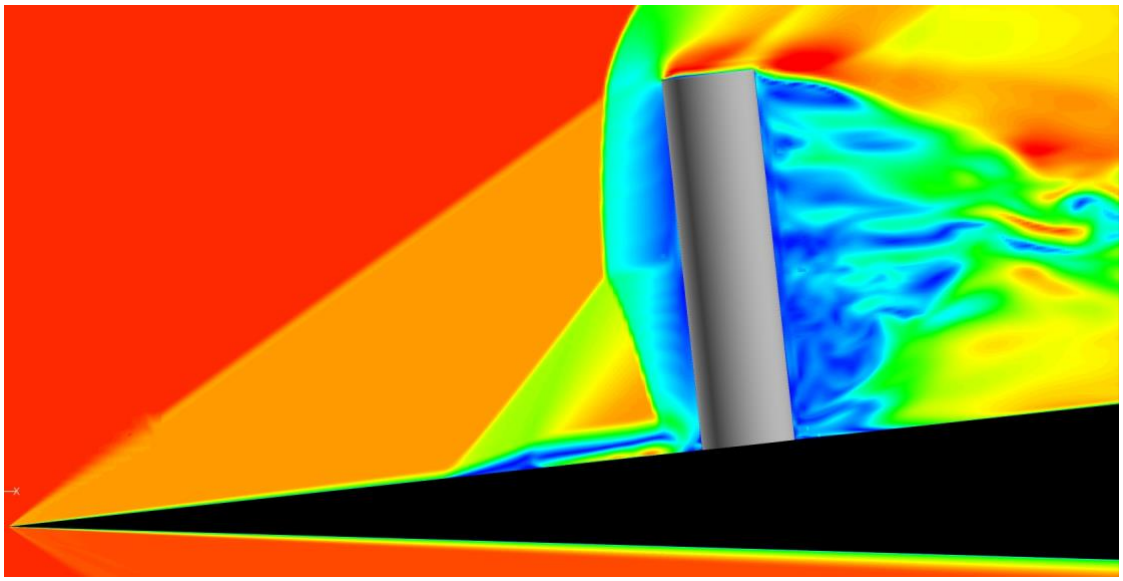

Figure 4.21 DDES-SA-QCR Mach contours after convergence. Flow is from left to right.

4.3.1.1 Surface Pressures

The computed DDES-SA-QCR surface pressures are displayed in Figure 4.22. As previously discussed, an expansion wave appears to reattach the flow to the surface in addition to developing small pockets in the separation region. The computed surface pressures exhibit a similar behavior in the reattachment region. A smaller region of separation occurs than the RANS simulations and a larger region of reattachment forms. Within the reattachment region, several pressure fluctuations can be seen indicating a potential for small separation pockets. The surface pressures appear to be visually symmetric in the spanwise direction.

Further insight on the computed surface pressures is revealed by the off-center surface pressures plotted in Figure 4.23. The off-center surface pressures confirm that simulation is symmetric in the spanwise direction with each pair of surface pressures showing no discernable difference in magnitude and local peak location in the region of interest. Approximately 0.75 diameters upstream of the cylinder leading edge, an oscillatory behavior occurs indicating a potential for small regions of separation. Two regions of separation are implied by the two local peaks. Additionally, the surface pressure in these regions of local separation drops below the freestream surface pressure. After the initial rise in pressure, an indication of the separation shock, the pressure sharply declines where the RANS simulations display a gradual decline. The sharp favorable gradient around x/d = -1.5 further emphasizes the existence of an expansion wave in the separation region.

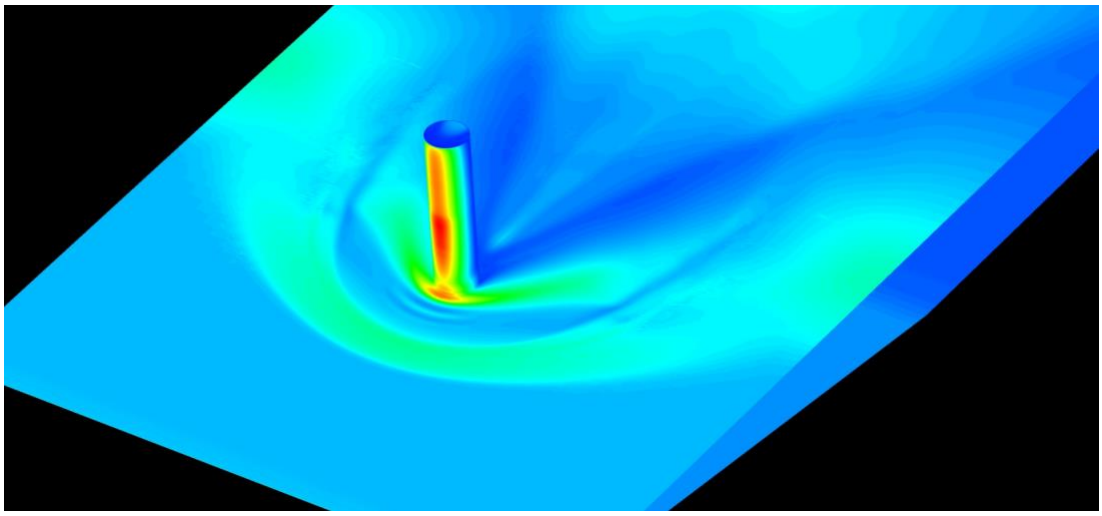

Figure 4.22 Instantaneous DDES-SA-QCR surface pressure contours after convergence. Flow is from bottom-left to top-right.

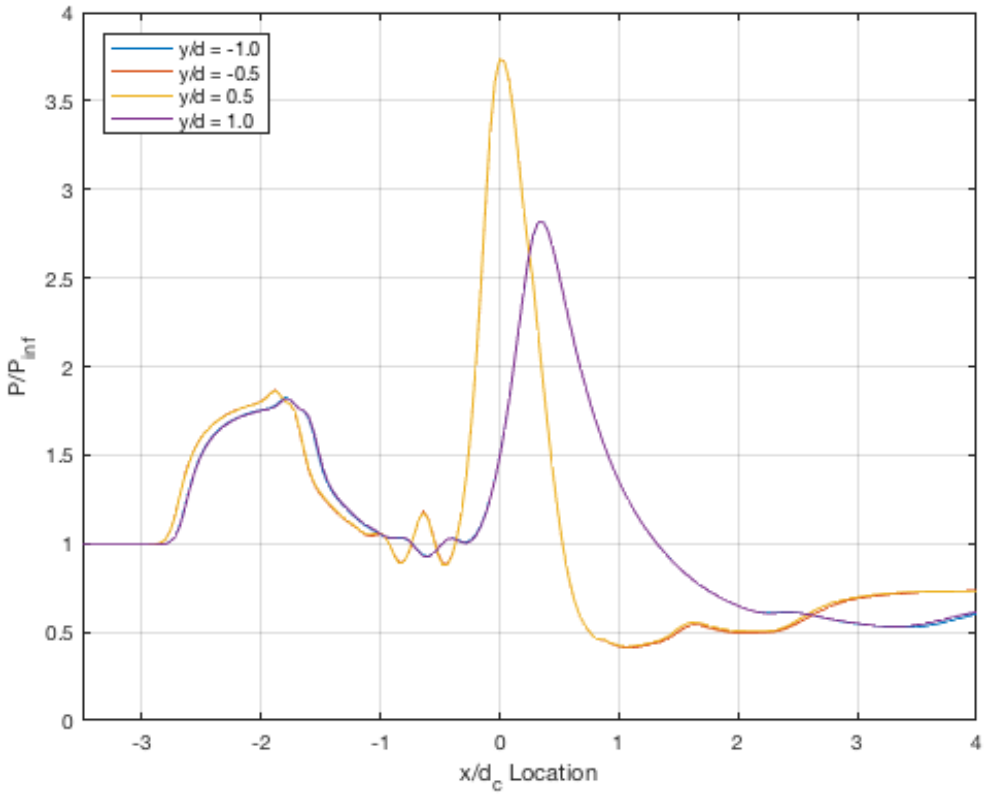

Figure 4.23 Instantaneous DDES-SA-QCR off-center surface pressures after reaching convergence normalized by freestream surface pressure. Zero denotes the location of the cylinder leading edge.

4.3.1.2 Velocity Profiles

The DDES-SA-QCR velocity profiles exhibit similar behaviors to the SA-QCR simulation; however, the velocity profile that passes through the separation region differs from the RANS to DDES simulation. Not only is the separation region larger, attributable to DDES because grid-induced separation can occur, but the separation bubble slows down the flow while the RANS simulation held the flow at a constant velocity across the wall-normal direction. This relation can be seen through the Mach contours of Figure 4.21 by the thin region of subsonic flow, denoted as the blue contour. While the magnitude of the streamwise velocity is approximately equal in this region for both simulations, the DDES simulation reaches a higher velocity closer to the plate surface. Again, this can be visualized in the Mach contours by the thin region of higher velocity flow just below the separation bubble.

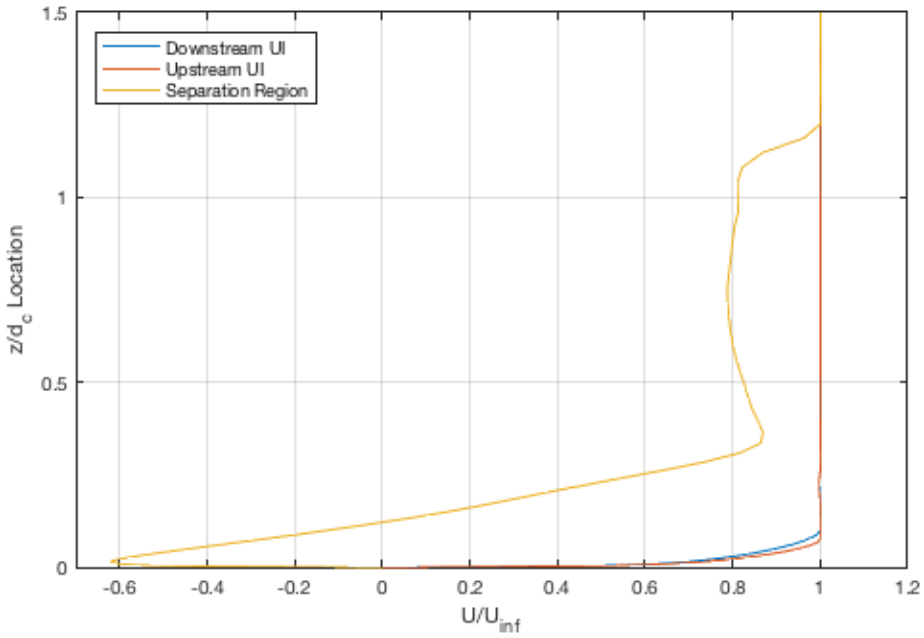

Figure 4.24 Instantaneous DDES-SA-QCR velocity profiles normalized by freestream velocity downstream of the inviscid oblique shock.

4.3.2 DDES-SA-QCR-AFT Results

As previously mentioned, the initial grid system displayed a dynamic behavior of the XSBLI phenomena. The time progression of the DDES-SA-QCR-AFT numerical Schlieren images for the initial grid system is portrayed in Figure 4.25. Note that this simulation is affected by the disturbances propagating from the overset boundary. Once a larger refinement region was implemented into the modified grid system, the dynamic behavior was not reproduced, implying that the overset boundary contributed to the unsteadiness. Similar to the DDES-SA-QCR simulation, as the DDES-SA-QCR-AFT simulation applied a hybrid RANS/LES turbulence closure, the bifurcated shock system expanded outward. During the expansion, the UI feature radiated from the separation shock similarly to the experimental reference; however, the simulation converged to the numerical Schlieren image displayed in Figure 4.26 after the initial expansion. All XSBLI phenomena in the DDES-SA-QCR simulation are present in the DDES-SA-QCR-AFT simulation with the addition of the UI feature. The UI feature appears to behave as a compression wave and weakens the strength of the separation shock downstream, showing similar behaviors to the RANS simulation.

Measurements of the DDES XSBLI phenomena are presented in Table 4.3. The DDES simulations over-predict the separation shock standoff distance and triple point height. Unlike the SA-QCR simulation, the DDES-SA-QCR-AFT simulation shows good agreement with the experimental measurement in regard to the UI shock location. Note that the simulation positions the UI feature approximately 1 diameter upstream of the separation shock, whereas the experimental reference has the time-averaged UI shock location approximate 1.7 diameters upstream.

The converged DDES-SA-QCR-AFT Mach contours are displayed in Figure 4.27. All DDES simulations predict a supersonic region near the surface of the separation region. A primary difference in the separation region of the two DDES simulations is the region just below the expansion fan. The DDES-SA-QCR simulation predicts a strong initial separation, denoted by the sharp curvature of the Mach contour whereas the DDES-SA-QCR-AFT simulation predicts a gradual rise the Mach contour. Additionally, the UI feature and separation shock of the

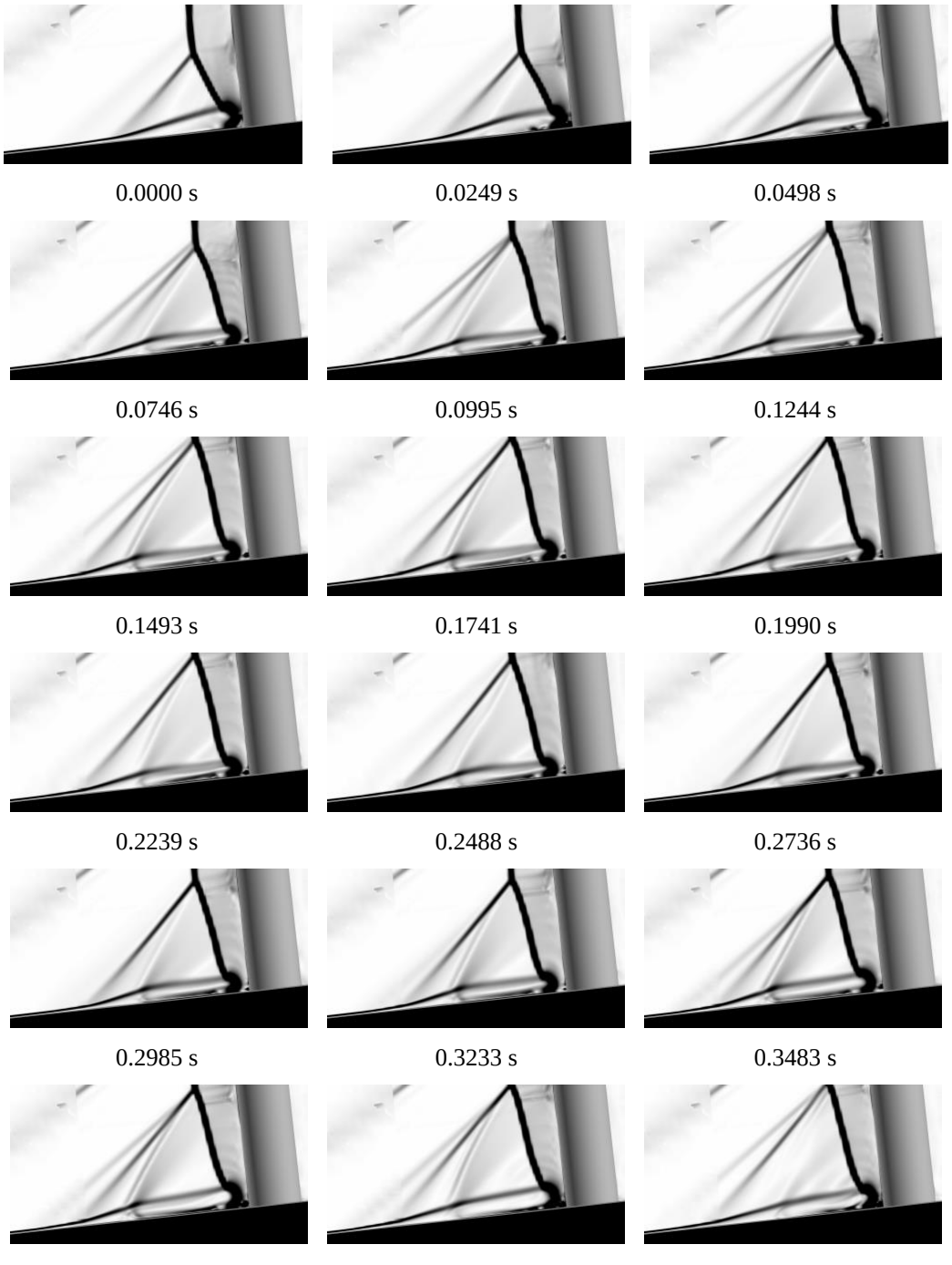

Figure 4.25 Time progression of initial grid DDES-SA-QCR-AFT numerical Schlieren images. Flow is from left to right. Note that what initially is seen as dynamic behavior due to transitional effects, is seen as disturbances propagating from the overset boundary.

Figure 4.26 DDES-SA-QCR-AFT numerical Schlieren after reaching convergence. Flow is from left to right.

Table 4.3 DDES XSBLI measurements.

	SA-QCR	**SA-QCR-AFT**	**Experimental Reference [18]**
h_{tp}/d_c	1.96	2.28	1.39
$\lambda_{s,1}/d_c$	2.64	2.96	2.24
$\lambda_{s,2}/d_c$	0.40	0.40	0.37
UI/d_c	n/a	3.92	3.90 - 4.20

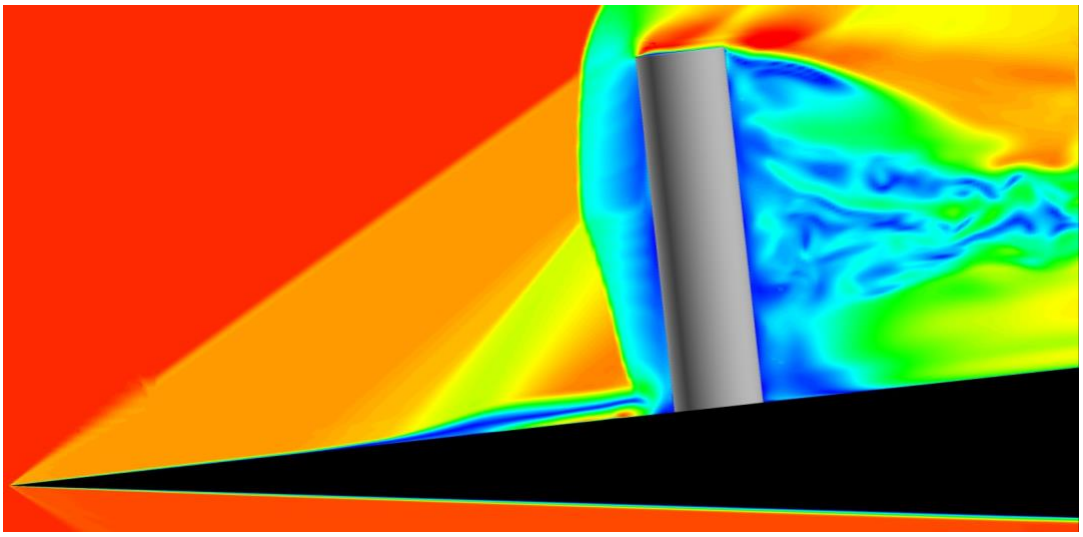

Figure 4.27 DDES-SA-QCR-AFT Mach contours after reaching convergence. Flow is from left to right.

DDES-SA-QCR-AFT simulation does not decelerate the flow as much as the single separation shock of the DDES-SA-QCR simulation. The phenomenon further indicates that the UI feature weakens the separation shock.

Displayed in Figure 4.28 are the computed surface skin friction distributions along the centerline for the DDES-SA-QCR and DDES-SA-QCR-AFT simulations. The DDES predicted surface skin frictions show a similar behavior to the RANS simulations with additional detail in the separation region. As expected, the transition simulation captures the same phenomenon of a steady decline before the UI feature. All prominent features are brought further upstream due to the implementation of DDES methods.

Further detail of the surface skin friction is provided in Figure 4.29 and Figure 4.30. The DDES-SA-QCR-AFT simulation captures separation further upstream than the DDES-SA-QCR simulation. Additionally, both simulations capture two regions of separation on the plate surface. The DDES-SA-QCR-AFT simulation captures a large separation region from the UI feature to the reattachment shock in addition to the separation region between the reattachment shock and the cylinder leading-edge. The DDES-SA-QCR simulation, however, captures a smaller separation region from the separation shock to the approximate location of the expansion wave within the separation bubble. The larger separation region occurs at the approximate location of

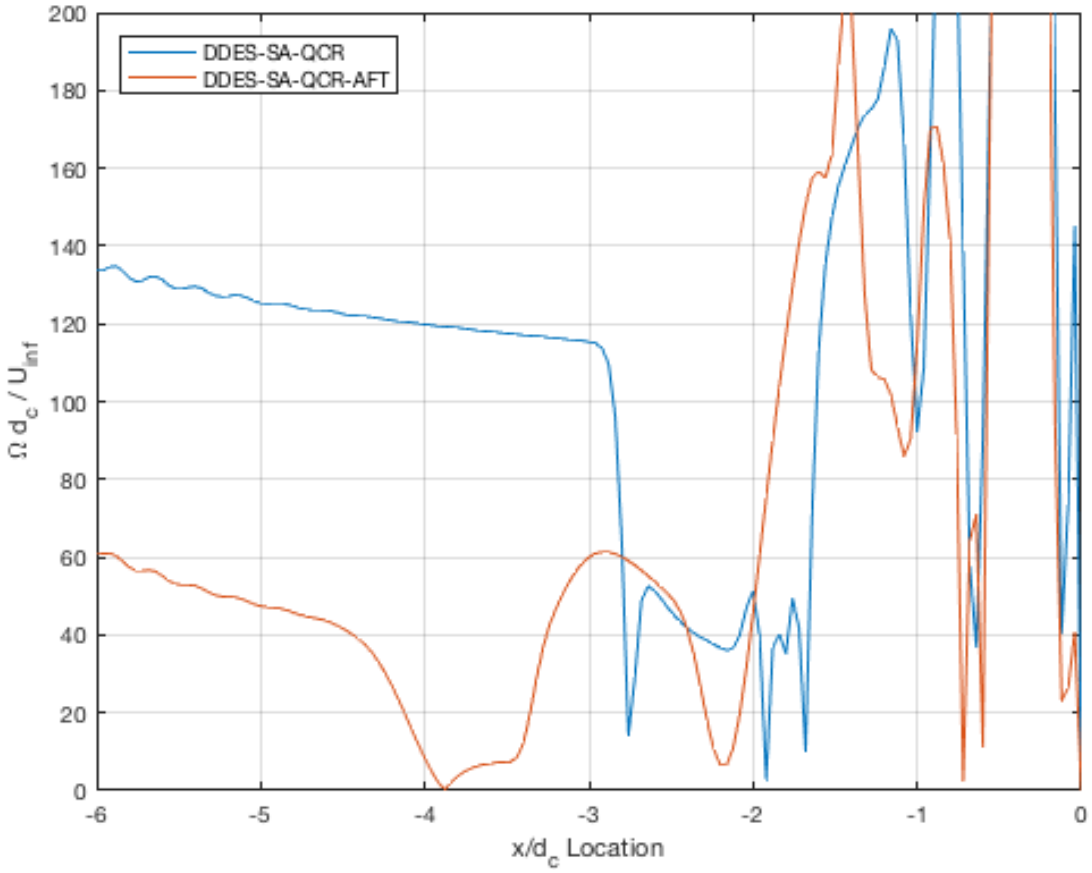

Figure 4.28 Unsteady normalized surface skin friction.

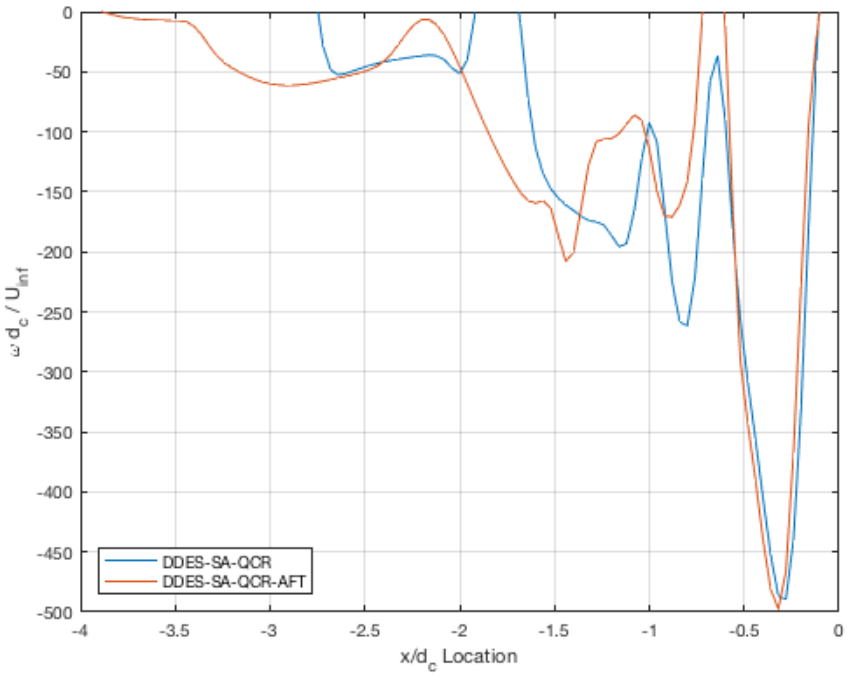

Figure 4.29 Unsteady normalized vorticity in the spanwise direction along the plate.

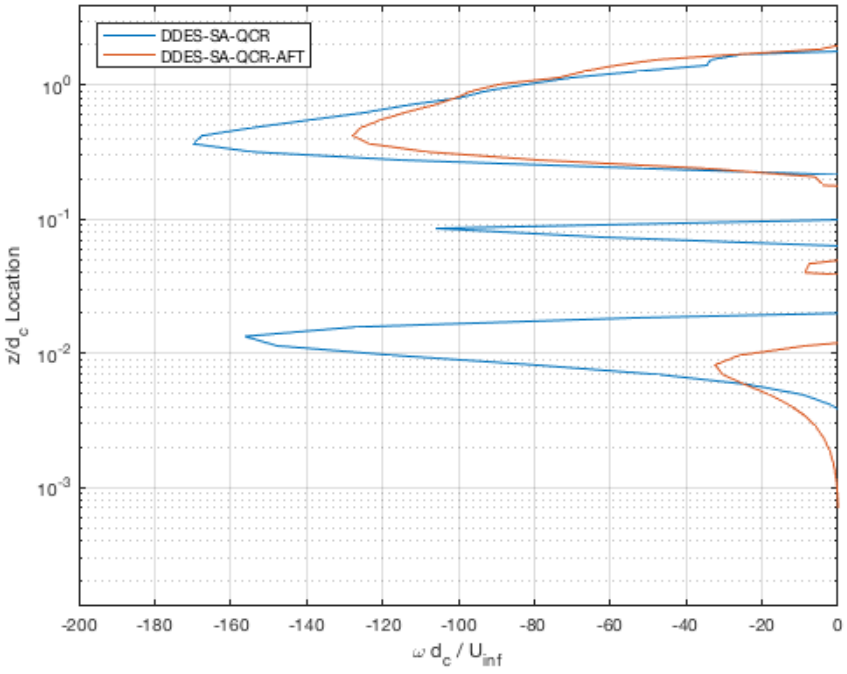

Figure 4.30 Unsteady normalized vorticity in the spanwise direction along the cylinder. Note the log scale on the y-axis.

the aforementioned Mach curvature to the cylinder leading-edge. Along the cylinder leading-edge, three regions of separation are predicted in approximately the same locations as the RANS simulations. The first predicted separation ($y/d_c \approx 0.1\text{-}1.0$) decreases in strength by a factor of two with the DDES-SA-QCR-AFT simulation being weaker than the DDES-SA-QCR. The second separation ($y/d_c \approx 1.0$) increased in strength by a factor or two for the fully-turbulent simulation and decreased by a factor of two for the DDES-SA-QCR-AFT simulation. Additionally, the DDES-SA-QCR-AFT simulation computed the location to be closer to the plate surface. The final separation ($y/d_c \approx 0.01$) in the DDES-SA-QCR simulation remained consistent with the RANS simulations. However, the DDES-SA-QCR-AFT simulation saw a significant decrease in strength while translating closer to the plate surface.

4.3.2.1 Surface Pressures

DDES-SA-QCR-AFT computed surface pressures are illustrated in Figure 4.31. The region of reattachment expands further outward in the spanwise direction than the DDES-SA-QCR simulation. Additionally, the reattachment region maintains its width in the spanwise direction whereas the DDES-SA-QCR tapers off. Again, the simulation is visually symmetric in the spanwise direction.

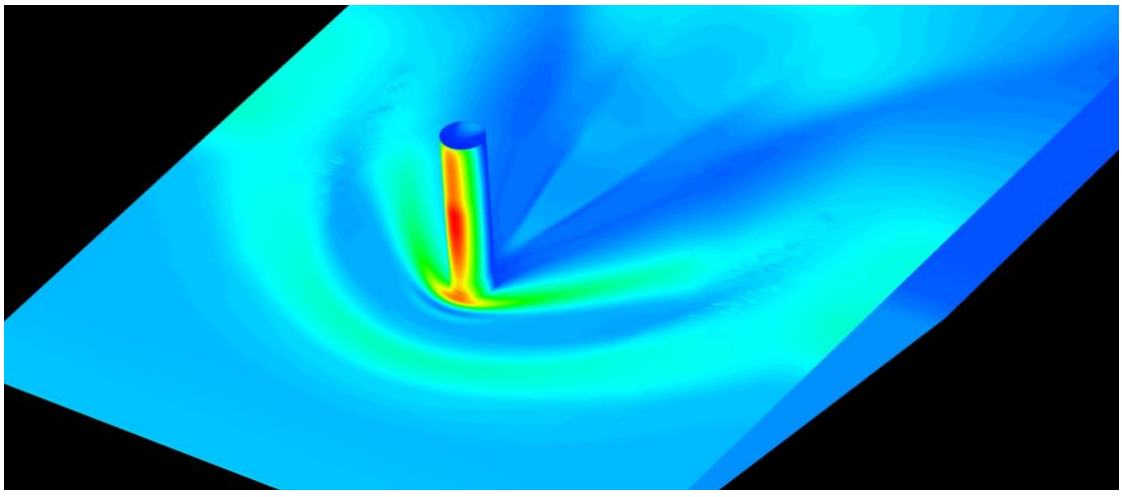

Figure 4.31 DDES-SA-QCR-AFT surface pressure contours after reaching convergence. Flow is from bottom-left to top-right.

Further detail provided for the computed centerline surface pressures is plotted in Figure 4.32 with a final analysis of both SA-QCR-AFT and DDES-SA-QCR-AFT surface pressures plotted in Figure 4.33. The unsteady centerline pressures behave similarly to their representative RANS pressures but have the local peak magnitudes further upstream. Additionally, the minimum pressures, located in the separation region, have values below the freestream surface pressure. This behavior was also in the laminar interaction of Lindorfer et al. [33]. Initially, the the SA-QCR-AFT and DDES-SA-QCR-AFT simulations exhibit behavior of a laminar interaction displayed by the initial rise in pressure before the sharper gradient. Within the separation region, the surface pressures show good agreement with the turbulent interaction in magnitude and shape. Note that the locations of the phenomena vary due to the simulations being conducted with the cylinder location at a $x/d_c = 7$ while the simulations of Lindorfer et al. were conducted at a cylinder location of $x/d_c = 25$ which would be fully in the turbulent region. The SA-QCR-AFT surface pressures display similar behavior to the turbulent interaction from the reattachment shock location to the cylinder leading-edge. However, the DDES-SA-QCR-AFT surface pressures show good agreement with the laminar interaction from the reattachment shock location to the cylinder leading-edge and predicts values of surface pressure below the freestream value. All simulations presented in this work, as well as the work by Lindorfer et al. [33], show good agreement in predicting the maximum surface pressures just upstream of the cylinder leading-edge. Unfortunately, the CFD simulations did not capture the peak surface pressure exhibited by the experimental reference.

Figure 4.34 displays the off-center surface pressures of the DDES-SA-QCR-AFT simulation. The DDES-SA-QCR-AFT surface pressures show good agreement with DDES-SA-QCR surface pressures with the exception of the gradual rise exhibited just upstream of the separation shock location produced by the UI shock. The DDES-SA-QCR-AFT simulation did not capture the spike present within the first local peak predicted by the DDES-SA-QCR simulation.

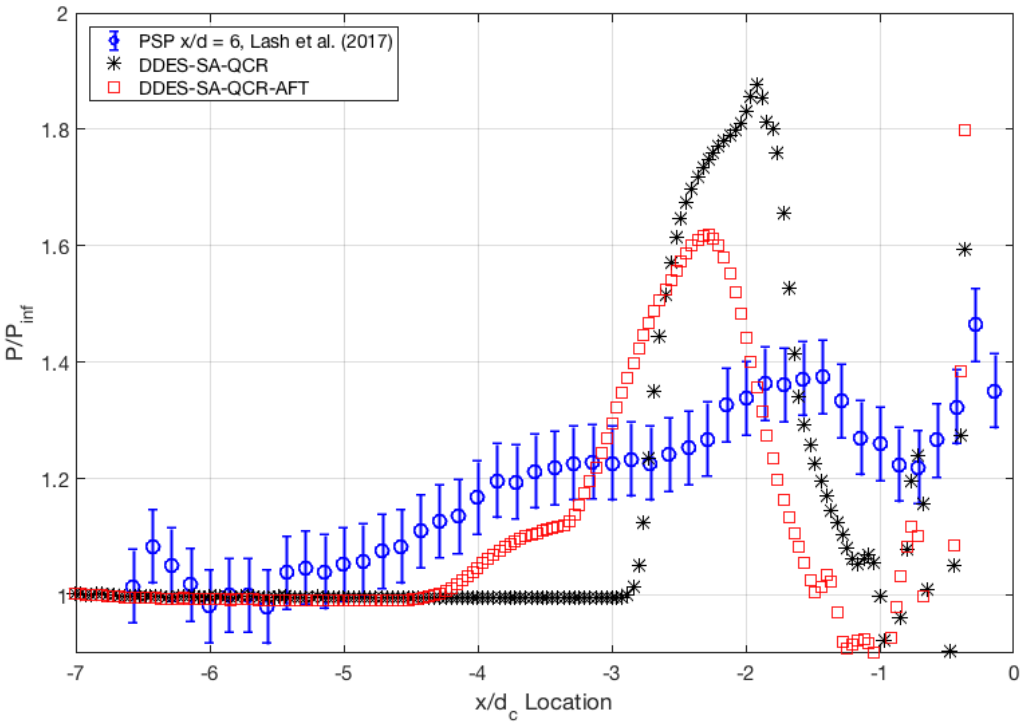

Figure 4.32 SA-QCR-AFT DDES centerline surface pressure after reaching convergence normalized by freestream surface pressure. Zero denotes the location of the cylinder leading-edge.

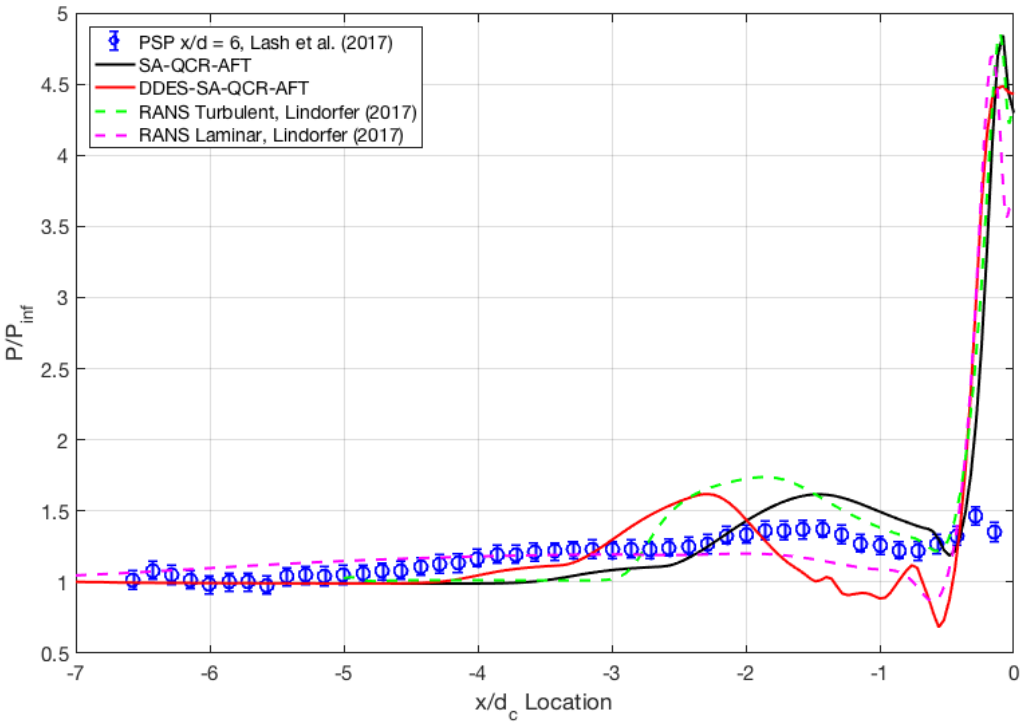

Figure 4.33 Comparison of both RANS and DDES-SA-QCR-AFT simulations. Zero denotes the location of the cylinder leading-edge.

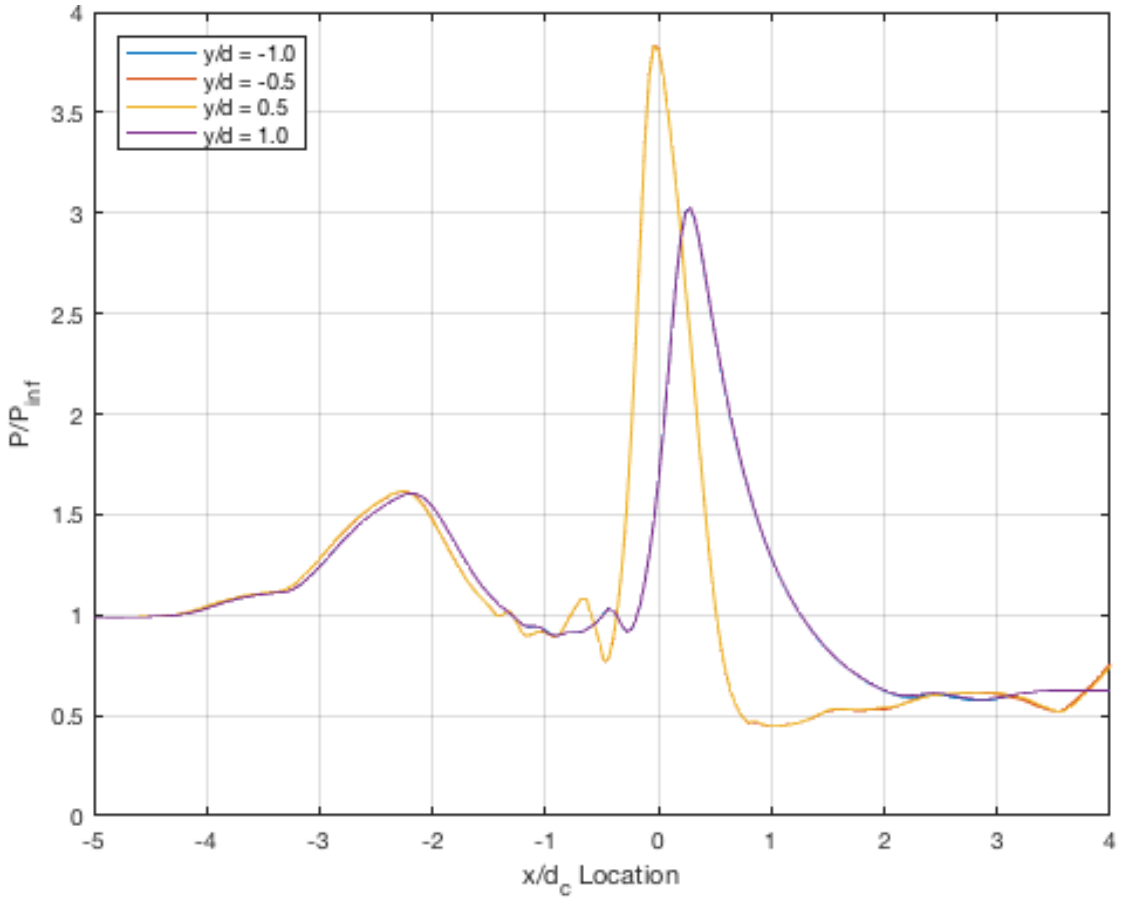

Figure 4.34 DDES-SA-QCR-AFT off-center surface pressure after reaching convergence normalized by freestream surface pressure. Zero denotes the location of the cylinder leading-edge.

4.3.2.2 Velocity Profiles

The velocity profiles at each respective location are provided through Figures 4.35-38. All velocity profiles show good agreement with the RANS simulations. Within the separation region, however, both DDES simulations predict a much larger separation height given by the taller triple-point height plotted in Figure 4.38. Additionally, a subsonic shear layer is exhibited just above the supersonic pockets indicated by the initial decrease in the velocity, whereas the RANS simulations predicted only an increase in velocity. Near the wall, the velocity is decreased approximately by a factor of two, which indicates a stronger vortex structure. After the separation shock location, denoted by the second spike in velocity, the DDES-SA-QCR-AFT simulation predicts the influence of the UI feature is approximately 0.75 y/d_c whereas the SA-QCR-AFT simulation predicts an influence of approximately 1 y/d_c indicating that the UI feature is closer to the separation shock.

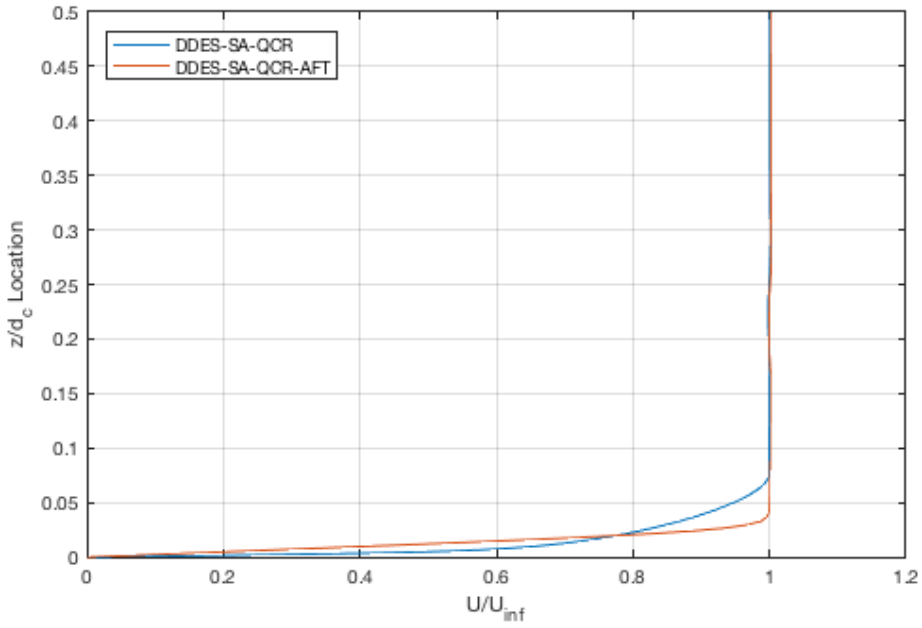

Figure 4.35 Unsteady velocity profiles upstream of UI shock normalized by freestream velocity downstream of the inviscid oblique shock.

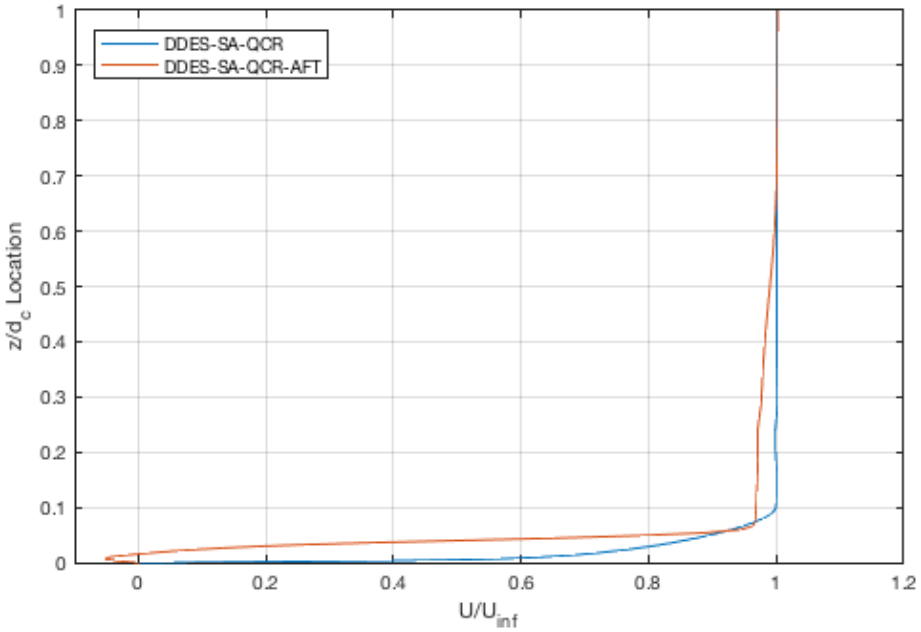

Figure 4.36 Unsteady velocity profiles downstream of UI shock normalized by freestream velocity downstream of the inviscid oblique shock.

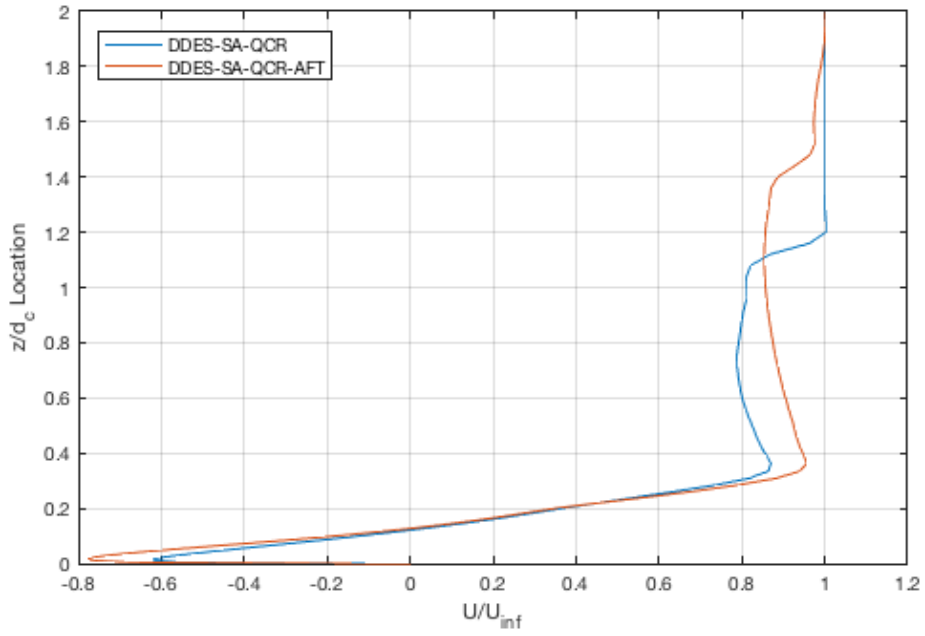

Figure 4.37 Unsteady velocity profiles in separation region normalized by freestream velocity downstream of the inviscid oblique shock.

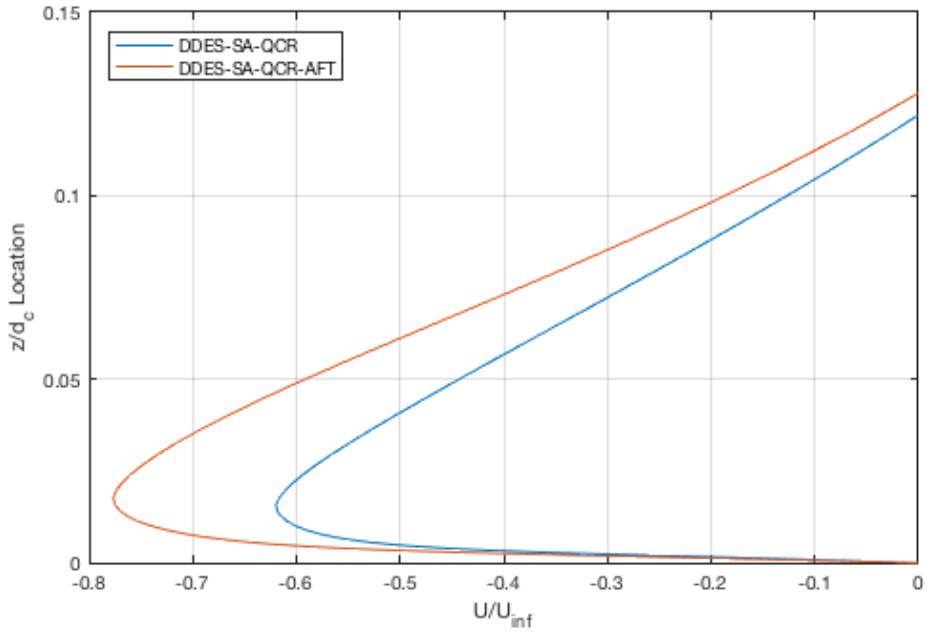

Figure 4.38 Near-wall unsteady velocity profiles in separation region normalized by freestream velocity downstream of the inviscid oblique shock.

CHAPTER 5
CONCLUSIONS

To study the capabilities of RANS-based modeling in simulating XSBLI phenomena, a series of RANS and DDES simulations were performed at M_∞ = 2.01. Each set of simulations consisted of a SA-QCR and SA-QCR-AFT case. Key parameters of interest were the separation shock standoff distance ($\lambda_{s,1}$), reattachment shock standoff distance ($\lambda_{s,2}$), triple point height (h_{tp}), and upstream-influence (UI) shock location.

RANS simulations showed good agreement with the empirical measurements of h_{tp}, $\lambda_{s,1}$, and $\lambda_{s,2}$. As anticipated, SA-QCR simulations did not capture the UI shock. SA-QCR-AFT simulations under-predicted the UI shock location, and the simulated UI shock appeared to resemble a compression wave and weakened the downstream separation shock.

The DDES-SA-QCR and DDES-SA-QCR-AFT simulations of the initial grid system captured the dynamic behavior of the shock system observed in the empirical data, but it was later determined that the overset boundary generated disturbances due to an interaction with the separation shock. Thus, a modified grid system was implemented for the simulations, in which the refinement region about the cylinder was extended upstream. Once DDES simulations were performed using the modified grid system, the simulations reached a visually converged state where all upstream flow features became spatially fixed. At the visually converged state, DDES simulations over-predicted h_{tp} and $\lambda_{s,1}$, but showed good agreement with the empirical $\lambda_{s,2}$ and UI shock location.

Analysis of the surface pressures indicated that they are symmetric along the spanwise plane in the region of interest. Off-center surface pressures exhibited similar behaviors to the respective centerline surface pressures in the upstream region. SA-QCR-AFT and DDES-SA-QCR-AFT simulations captured a gradual increase before the sharp gradient observed in both cases. The gradual increase showed similar behavior to the computational laminar interaction

[33] before displaying behaviors of a turbulent interaction in the separation region. At the reattachment shock location, the DDES-SA-QCR-AFT simulation saw a decrease in pressure below the freestream value, representative of a laminar interaction, while the SA-QCR-AFT simulation maintained a pressure above the freestream value, representative of a turbulent interaction.

The surface skin friction provided further insight on potential mechanisms forming the UI shock. The SA-QCR-AFT and DDES-SA-QCR-AFT simulations saw a gradual decrease upstream of the UI shock location. A decrease in surface skin friction can be related to an increase in the boundary layer thickness, thus implying that a boundary layer thickening generates a compression ramp, producing an UI shock. Without the UI shock, the boundary layer does not produce behavior similar to a compression ramp in the SA-QCR and DDES-SA-QCR simulations. Consequently, the UI shock reinforces the upstream boundary layer thickening, but, no conclusive origin of the phenomenon has been identified at present.

Lastly, the spanwise vorticity displays the regions of separation along the plate and cylinder surface. The RANS simulations captured one large vortex in the separation region of the plate while DDES simulations produced two smaller vortices. Along the cylinder leading-edge, three regions of separation appear for all simulations approximately located at the cylinder-plate junction, the interaction of the reattachment shock and separation bubble, and h_{tp}.

LIST OF REFERENCES

1. Babinsky, H., and Harvey, J. K. *Shock wave-boundary-layer interactions*: Cambridge University Press, 2011.
2. Délery, J., Marvin, J. G., and Reshotko, E. "Shock-wave boundary layer interactions." ADVISORY GROUP FOR AEROSPACE RESEARCH AND DEVELOPMENT NEUILLY-SUR-SEINE (FRANCE), 1986.
3. Dolling, D. S. "Fifty years of shock-wave/boundary-layer interaction research: what next?," *AIAA journal* Vol. 39, No. 8, 2001, pp. 1517-1531.
4. Gaitonde, D. V. "Progress in shock wave/boundary layer interactions," *Progress in Aerospace Sciences* Vol. 72, 2015, pp. 80-99.
5. Green, J. "Interactions between shock waves and turbulent boundary layers," *Progress in Aerospace Sciences* Vol. 11, 1970, pp. 235-340.
6. Knight, D. D., and Degrez, G. "Shock wave boundary layer interactions in high Mach number flows a critical survey of current numerical prediction capabilities," *AGARD ADVISORY REPORT AGARD AR* Vol. 2, 1998, pp. 1-1.
7. Knight, D. D., and Mortazavi, M. "Hypersonic Shock Wave Transitional Boundary Layer Interactions-A Review," *47th AIAA Fluid Dynamics Conference*. 2017, p. 3124.
8. Morkovin, M. V. "On the many faces of transition," *Viscous drag reduction*. Springer, 1969, pp. 1-31.
9. Morkovin, M. V. "Critical evaluation of transition from laminar to turbulent shear layers with emphasis on hypersonically traveling bodies." MARTIN MARIETTA CORP BALTIMORE MD RESEARCH INST FOR ADVANCED STUDIES, 1969.
10. Reed, H. L., and Saric, W. S. "Stability of three-dimensional boundary layers," *Annual Review of Fluid Mechanics* Vol. 21, No. 1, 1989, pp. 235-284.
11. Saric, W. S., Reed, H. L., and Kerschen, E. J. "Boundary-layer receptivity to freestream disturbances," *Annual review of fluid mechanics* Vol. 34, No. 1, 2002, pp. 291-319.
12. Leidy, A., Neel, I., Bowersox, R. D., and Schmisseur, J. D. "Influence of perturbations on 3-D hypersonic shock laminar boundary interactions," *55th AIAA Aerospace Sciences Meeting*. 2017, p. 1685.

13. Coder, J. G. "Standard Test Cases for CFD-Based Laminar-Transition Model Verification and Validation," *2018 AIAA Aerospace Sciences Meeting*. American Institute of Aeronautics and Astronautics, 2018.
14. Hall, Z. "Assessment of Transition Modeling Capabilities in NASA?s OVERFLOW CFD Code version 2.2m," *2018 AIAA Aerospace Sciences Meeting*. American Institute of Aeronautics and Astronautics, 2018.
15. Hall, Z. "CFD Modeling of US Army Shadow UAV Wind Tunnel Testing for OVERFLOW CFD Transition Model Validation," *2018 AIAA Aerospace Sciences Meeting*. American Institute of Aeronautics and Astronautics, 2018.
16. Rumsey, C. L., Slotnick, J. P., and Sclafani, A. J. "Overview and Summary of the Third AIAA High Lift Prediction Workshop," *2018 AIAA Aerospace Sciences Meeting*. American Institute of Aeronautics and Astronautics, 2018.
17. Combs, C. S., Lash, E. L., and Schmisseur, J. D. "Investigation of a Cylinder-Induced Transitional Shock Wave-Boundary Layer Interaction using Laser Diagnostics," *32nd AIAA Aerodynamic Measurement Technology and Ground Testing Conference*. American Institute of Aeronautics and Astronautics, 2016.
18. Lash, E. L., Combs, C. S., Kreth, P. A., Beckman, E. A., and Schmisseur, J. D. "Developing an Image-Based Analysis of the Dynamics of Transitional Shock Wave-Boundary Layer Interactions," *32nd AIAA Aerodynamic Measurement Technology and Ground Testing Conference*. American Institute of Aeronautics and Astronautics, 2016.
19. Lash, E. L., Combs, C. S., Kreth, P. A., and Schmisseur, J. D. "Study of the Dynamics of Transitional Shock Wave-Boundary Layer Interactions using Optical Diagnostics," *47th AIAA Fluid Dynamics Conference*. American Institute of Aeronautics and Astronautics, 2017.
20. Lash, E. L., Combs, C. S., Kreth, P. A., and Schmisseur, J. D. "Experimental Investigation of a Cylinder-Induced Transitional Shock Wave-Boundary Layer Interaction," *55th AIAA Aerospace Sciences Meeting*. American Institute of Aeronautics and Astronautics, 2017.

21. Nichols, R., and Buning, P. "OVERFOW User's Manual, Version 2.2," *NASA Langley Research Center, Hampton, VA*, 2010.
22. Schülein, E. "Effects of Laminar-Turbulent Transition on the Shock-Wave/Boundary-Layer Interaction," *44th AIAA Fluid Dynamics Conference*. 2014, p. 3332.
23. Sandham, N., Schülein, E., Wagner, A., Willems, S., and Steelant, J. "Transitional shock-wave/boundary-layer interactions in hypersonic flow," *Journal of Fluid Mechanics* Vol. 752, 2014, pp. 349-382.
24. Willems, S., and Gülhan, A. "Experiments on Shock Induced Laminar-Turbulent Transition on a Flat Plate at Mach 6," 2013.
25. Willems, S., Gülhan, A., and Steelant, J. "Experiments on the effect of laminar–turbulent transition on the SWBLI in H2K at Mach 6," *Experiments in Fluids* Vol. 56, No. 3, 2015, p. 49.
26. Teramoto, S. "Large-eddy simulation of transitional boundary layer with impinging shock wave," *AIAA journal* Vol. 43, No. 11, 2005, pp. 2354-2363.
27. Benay, R., Chanetz, B., Mangin, B., Vandomme, L., and Perraud, J. "Shock wave/transitional boundary-layer interactions in hypersonic flow," *AIAA journal* Vol. 44, No. 6, 2006, pp. 1243-1254.
28. Estruch-Samper, D., Ganapathisubramani, B., Vanstone, L., and Hillier, R. "Axisymmetric flare-induced separation of high-speed transitional boundary layers," *50th AIAA Aerospace Sciences Meeting including the New Horizons Forum and Aerospace Exposition*. 2012, p. 67.
29. Benay, V. "Shock Wave Transitional Boundary Layer Interaction in Hypersonic Flow," *12th AIAA International Space Planes and Hypersonic Systems and Technologies*. American Institute of Aeronautics and Astronautics, 2003.
30. Bur, R., and Chanetz, B. "Experimental study on the PRE-X vehicle focusing on the transitional shock-wave/boundary-layer interactions," *Aerospace Science and Technology* Vol. 13, No. 7, 2009, pp. 393-401.
31. Estruch-Samper, D., Vanstone, L., Ganapathisubramani, B., and Hillier, R. "Effect of roughness-induced disturbances on axisymmetric hypersonic laminar boundary layer,"

51st AIAA Aerospace Sciences Meeting including the New Horizons Forum and Aerospace Exposition. 2013, p. 83.

32. Murphree, Z., Yuceil, K., Clemens, N., and Dolling, D. "Experimental studies of transitional boundary layer shock wave interactions," *45th AIAA Aerospace Sciences Meeting and Exhibit*. 2006, p. 1139.
33. Lindörfer, S., S. Combs, C., A. Kreth, P., Bond, R., and D. Schmisseur, J. *Limiting Cases for Cylinder-Induced Shock Wave/Boundary Layer Interactions*, 2017.
34. Dolling, D., and Bogdonoff, S. "Blunt fin-induced shock wave/turbulent boundary-layer interaction," *AIAA Journal* Vol. 20, No. 12, 1982, pp. 1674-1680.
35. Pulliam, T. H., and Steger, J. L. "Implicit finite-difference simulations of three-dimensional compressible flow," *AIAA Journal* Vol. 18, No. 2, 1980, pp. 159-167.
36. William M. Chan, S. E. R., Shishir A. Pandya, David L. Kao, Pieter G. Buning, Robert L. Meakin, David A. Boger, Steven M. Nash. "Chimera Grid Tools User's Manual, Version 2.1," *NASA Langley Research Center, Hampton, VA*, 2010.
37. Meakin, R. "Object X-rays for cutting holes in composite overset structured grids," *15th AIAA computational fluid dynamics conference*. 2001, p. 2537.
38. Nichols, R. H., Tramel, R. W., and Buning, P. G. "Evaluation of two high-order weighted essentially nonoscillatory schemes," *AIAA journal* Vol. 46, No. 12, 2008, pp. 3090-3102.
39. Tramel, R., Nichols, R., and Buning, P. "Addition of improved shock-capturing schemes to OVERFLOW 2.1," *19th AIAA Computational Fluid Dynamics*. 2009, p. 3988.
40. Nichols, R., Tramel, R., and Buning, P. "Solver and turbulence model upgrades to OVERFLOW 2 for unsteady and high-speed applications," *24th AIAA Applied Aerodynamics Conference*. 2006, p. 2824.
41. Henrick, A. K., Aslam, T. D., and Powers, J. M. "Mapped weighted essentially non-oscillatory schemes: achieving optimal order near critical points," *Journal of Computational Physics* Vol. 207, No. 2, 2005, pp. 542-567.
42. Merriman, B. "Understanding the Shu–Osher conservative finite difference form," *Journal of Scientific Computing* Vol. 19, No. 1-3, 2003, pp. 309-322.

43. Liu, X.-D., Osher, S., and Chan, T. "Weighted essentially non-oscillatory schemes," *Journal of computational physics* Vol. 115, No. 1, 1994, pp. 200-212.
44. Spalart, P., and Allmaras, S. "A one-equation turbulence model for aerodynamic flows," *30th aerospace sciences meeting and exhibit*. 1992, p. 439.
45. Spalart, P. R. "Strategies for turbulence modelling and simulations," *International Journal of Heat and Fluid Flow* Vol. 21, No. 3, 2000, pp. 252-263.
46. Mani, M., Babcock, D., Winkler, C., and Spalart, P. "Predictions of a supersonic turbulent flow in a square duct," *51st AIAA Aerospace Sciences Meeting including the New Horizons Forum and Aerospace Exposition*. 2013, p. 860.
47. Coder, J. G., Pulliam, T. H., and Jensen, J. C. "Contributions to HiLiftPW-3 Using Structured, Overset Grid Methods," *2018 AIAA Aerospace Sciences Meeting*. 2018, p. 1039.
48. Spalart, P., Jou, W., Strelets, M., and Allmaras, S. "Comments on the feasibilty of LES for wings and on the hybrid RANS/LES approach, Advances in DNS/LES, 1st AFOSR Int. Conf. on DNS/LES." Greden Press, 1997.
49. Spalart, P. R., Deck, S., Shur, M. L., Squires, K. D., Strelets, M. K., and Travin, A. "A new version of detached-eddy simulation, resistant to ambiguous grid densities," *Theoretical and computational fluid dynamics* Vol. 20, No. 3, 2006, p. 181.
50. Coder, J. G., and Maughmer, M. D. "Computational fluid dynamics compatible transition modeling using an amplification factor transport equation," *AIAA Journal* Vol. 52, No. 11, 2014, pp. 2506-2512.
51. Coder, J. G. "Enhancement of the Amplification Factor Transport Transition Modeling Framework," *55th AIAA Aerospace Sciences Meeting*. American Institute of Aeronautics and Astronautics, 2017.
52. Mack, L. M. "Transition and laminar instability," 1977.
53. Drela, M., and Giles, M. B. "Viscous-inviscid analysis of transonic and low Reynolds number airfoils," *AIAA journal* Vol. 25, No. 10, 1987, pp. 1347-1355.

54. Menter, F. R., Smirnov, P. E., Liu, T., and Avancha, R. "A one-equation local correlation-based transition model," *Flow, Turbulence and Combustion* Vol. 95, No. 4, 2015, pp. 583-619.

VITA

Bradley Wayne Tester was born in Nashville, TN to the parents of Sharon and Wayne Tester. He was raised in Franklin and Thompson's Station, TN, where he graduated from Independence High School. The next four years, he studied Aerospace Engineering at the University of Tennessee where he received a Bachelor of Science degree in May 2016. He accepted a research position under Dr. James Coder at the University of Tennessee. After two years, he received a Master of Science degree in May 2018.